Ripples from the Early Universe to the Present

Thesis by
Adriano Testa

In Partial Fulfillment of the Requirements for the
Degree of
Doctor of Philosophy

Caltech

CALIFORNIA INSTITUTE OF TECHNOLOGY
Pasadena, California

2025
Defended May 30, 2025

Adriano Testa
ORCID: 0000-0003-4423-9243

"You have to be lost to find a place that can't be found."
— Captain Barbossa

ACKNOWLEDGEMENTS

First and foremost, I would like to thank my advisor, Mark Wise, for his guidance and support throughout my time at Caltech, for always believing in me, and for his infectious dedication and passion for physics. From the very beginning, he gave me the chance to learn by his side and encouraged me to pursue my own ideas while always providing thoughtful advice when I needed it.

I am deeply grateful to Olivier Doré for many illuminating discussions, for introducing me to his group, and for serving on both my candidacy and defense committees. I also thank Frank Porter and Michele Papucci, who likewise served on those committees.

I am indebted to my collaborators and colleagues at Caltech and elsewhere, and to Paolo Pani for his mentorship during my master's studies. I also thank Carol Silberstein for her reliable administrative support.

I would like to thank my friend and colleague Samuel Patrone for his unwavering commitment to understanding physics in depth, his patient explanations, and the many hours we spent at the blackboard and beyond, as we learned, laughed, and grew together.

I want to thank my friend Léo Borrel for all the late-night discussions about life, physics, and everything in between, for always being an example of integrity, for his help through difficult times, and for being such a terrific flatmate.

I am also grateful for the friendship of those with whom I shared different parts of my time at Caltech, including Osmond Wen, Magel Su, Michele Tarquini, Federico Cima, and Francesco Calisto.

Finally, I thank my family and all my other friends for their encouragement and patience throughout this journey.

This material is based upon work supported by the U.S. Department of Energy, Office of Science, Office of High Energy Physics, under Award Number DE-SC0011632.

ABSTRACT

In this thesis we study a range of topics in cosmology and gravitational wave physics, emphasizing their roles as probes of fundamental physics across vastly different scales. On the cosmology side, we focus on the analysis of the bispectrum, which provides unique insights into the physics of the early universe. Our work includes a calculation of the bispectrum in the squeezed-limit in quasi-single field inflation using Conformal Fermi Coordinates, a demonstration of the equivalence of different regularization prescriptions for the galaxy bias expansion, and the first numerical evaluation of the bispectrum in the Spherical Fourier-Bessel basis. On the gravitational wave side, we present an analytical template for the ring-down signal from rotating exotic compact objects, with applications to searches in interferometer data.

PUBLISHED CONTENT AND CONTRIBUTIONS

During my PhD I contributed to the following published papers. All authors contributed equally.

[1] E. Maggio, A. Testa, S. Bhagwat, and P. Pani, "Analytical model for gravitational-wave echoes from spinning remnants," *Phys. Rev. D* **100**, 064056 (2019). doi:10.1103/PhysRevD.100.064056, arXiv:1907.03091 [gr-qc].

[2] A. Testa, and M. B. Wise, "Impact of transforming to conformal Fermi coordinates on quasi-single field non-Gaussianity," *Phys. Rev. D* **102**, 023533 (2020). doi:10.1103/PhysRevD.102.023533, arXiv:2004.06126 [astro-ph.CO].

[3] S. Patrone, A. Testa, and M. B. Wise, "Regularization Scheme Dependence of the Counterterms in the Galaxy Bias Expansion," *JCAP* **11**, 087 (2023). doi:10.1088/1475-7516/2023/11/087, arXiv:2306.08025 [astro-ph.CO].

[4] J. N. Benabou, A. Testa, C. Heinrich, H. S. Grasshorn Gebhardt, and O. Doré, "Galaxy bispectrum in the spherical Fourier-Bessel basis," *Phys. Rev. D* **109**, 103507 (2024). doi:10.1103/PhysRevD.109.103507, arXiv:2312.15992 [astro-ph.CO].

[5] P. Fileviez Pérez, C. Murgui, S. Patrone, A. Testa, and M. B. Wise, "Finite naturalness and quark-lepton unification," *Phys. Rev. D* **109**, 015011 (2024). doi:10.1103/PhysRevD.109.015011, arXiv:2308.07367 [hep-ph].

The last publication listed above, [5], is in the field of particle physics and is not discussed in this thesis as it lies beyond its primary scope. Chapters 2 through 5 of this dissertation are adapted from publications [1–4].

TABLE OF CONTENTS

LIST OF ILLUSTRATIONS

LIST OF TABLES

Number *Page*

Chapter 1

INTRODUCTION

Gravity influences the universe at every scale, from the smallest distances near compact objects probed by gravitational wave interferometers to the largest structures revealed by galaxy surveys.

While general relativity and inflationary cosmology have achieved significant successes in describing a wide range of phenomena, important questions remain. These include the true nature of compact objects and the mechanisms that shaped the early universe.

On the experimental side, the past decade has seen substantial progress. The first detection of gravitational waves by the Laser Interferometer Gravitational-Wave Observatory (LIGO) and Virgo in 2015 opened a new observational window, making it possible to search for signatures of quantum gravity in ways that were previously inaccessible.

Meanwhile, galaxy surveys such as the Dark Energy Spectroscopic Instrument (DESI) and Euclid have begun delivering detailed maps of the large-scale distribution of galaxies. Synergies between these and the recently launched SPHEREx mission, as well as future observatories like the Nancy Grace Roman Space Telescope, will enable increasingly stringent searches for subtle imprints of new physics in the primordial universe.

Bridging the gap between this rapidly expanding body of precise observational data and our theoretical understanding of the underlying physical processes presents a number of challenges. As the volume and complexity of data increase, progress increasingly relies on overcoming computational challenges and on formulating theoretical predictions in a way that enables direct comparison with observational data.

This thesis addresses some aspects of these challenges.

In Chapter 2, we present an analytical template for the gravitational wave signal from rotating exotic compact objects, building on previous work by the author for non-spinning objects. This physically motivated approach allows fast searches for signals using matched filtering.

The remaining chapters focus on cosmological applications.

In Chapter 3, we consider the minimal extension of single field inflation known as Quasi Single Field Inflation (QSFI). We calculate the curvature bispectrum in the squeezed limit in Conformal Fermi Coordinate and find deviations from the perfect cancellation present in single field inflation.

In Chapter 4, we explore the effect of different regularization schemes on the counterterms in the renormalization of the galaxy bias expansion in the context of primordial local non-Gaussianity. This analysis clarifies the internal consistency of the theory and demonstrates the equivalence of different conventions, enabling the choice of the most convenient prescription for further calculations and simulations.

Finally, in Chapter 5, we study the galaxy bispectrum in the Spherical Fourier-Bessel (SFB) basis. The SFB approach is particularly well suited for wide-angle surveys, and we present the first numerical calculation of the three-point function in this basis.

Chapter 2

ANALYTICAL MODEL FOR GRAVITATIONAL-WAVE ECHOES FROM SPINNING REMNANTS

Gravitational-wave echoes in the post-merger signal of a binary coalescence are predicted in various scenarios, including near-horizon quantum structures, exotic states of matter in ultracompact stars, and certain deviations from general relativity. The amplitude and frequency of each echo is modulated by the photon-sphere barrier of the remnant, which acts as a spin- and frequency-dependent high-pass filter, decreasing the frequency content of each subsequent echo. Furthermore, a major fraction of the energy of the echo signal is contained in low-frequency resonances corresponding to the quasi-normal modes of the remnant. Motivated by these features, in this chapter we provide an analytical gravitational-wave template in the low-frequency approximation describing the post-merger ringdown and the echo signal of a spinning ultracompact object. Besides the standard ringdown parameters, the template is parametrized in terms of only two physical quantities: the reflectivity coefficient and the compactness of the remnant. We discuss novel effects related to the spin and to the complex reflectivity, such as a more involved modulation of subsequent echoes, the mixing of two polarizations, and the ergoregion instability in case of perfectly-reflecting spinning remnants. Finally, we compute the errors in the estimation of the template parameters with current and future gravitational-wave detectors using a Fisher matrix framework. Our analysis suggests that models with almost perfect reflectivity can be excluded/detected with current instruments, whereas probing values of the reflectivity smaller than 80% at 3σ confidence level requires future detectors (Einstein Telescope, Cosmic Explorer, LISA). The template developed in this chapter can be easily implemented to perform a matched-filter based search for echoes and to constrain models of exotic compact objects.

2.1 Introduction

Gravitational-wave (GW) echoes in the post-merger signal of a compact binary coalescence might be a smoking gun of near-horizon quantum structures [6–9], exotic compact objects (ECOs), exotic states of matter in ultracompact stars [10–12], and of modified theories of gravity [13, 14] (see [15–17] for some reviews). Detecting echoes in the GW data of LIGO/Virgo and of future GW observatories would allow us to probe the near-horizon structure of compact objects. The absence of echoes in GW data could instead place increasingly stronger constraints on alternatives to the black-hole (BH) paradigm.

Tentative evidence for echoes in the combined LIGO/Virgo binary BH events [18, 19] and in the neutron-star binary coalescence GW170817 [20] have been reported, followed by controversial claims about the statistical significance of such results [18, 19, 21–24], and by recent negative searches using a more accurate template [25] and a morphology-independent algorithm [26]. Performing a reliable search for echoes requires developing data analysis techniques as well as constructing accurate waveform models. Here we focus on the latter challenge.

While several features of the signal have been understood theoretically [17], an important open problem is to develop templates for echoes that are both accurate and practical for searches in current and future detectors, which might complement model-independent [19, 20, 27] and burst [26, 28, 29] searches, the latter being independent of the morphology of the echo waveform. Furthermore, using an accurate template is crucial for model selection and to discriminate the origin of the echoes in case of a detection. There has been a considerable progress in modeling the echo waveform [25, 30–36], but the approaches adopted so far are not optimal, since they are either based on analytical templates not necessarily related to the physical properties of the remnant, or rely on model-dependent numerical waveforms which are inconvenient for matched filtered searches and can be computationally expensive. In this chapter, we provide an analytical, physically motivated template that is parametrized by the standard ringdown parameters plus two physical quantities related to the properties of the exotic remnant. Our template can be easily implemented in a matched filter based data analysis.

We extend the recent analytical template of Ref. [2] to include spin effects. This is particularly important for various reasons. First, merger remnants are typically rapidly spinning (dimensionless spin $\chi \approx 0.7$ in case of nonspinning binaries, due to angular-momentum conservation); second, the spin might introduce nontrivial effects in the shape and modulation of echoes; finally, spinning ECOs have a rich phenomenology [17], for example they might undergo various types of instabilities [3, 4, 37–43]. In particular, if an ergoregion instability [39, 43, 44] occurs, the signal would grow exponentially in time over a time scale which is generically parametrically longer than the time delay between echoes, and it is always much longer than the object's dynamical time scale [45].

In this chapter we use $G = c = 1$ units.

2.2 Analytical echo template

Reference [31] presents a framework for modeling the echoes from nonspinning ECOs by reprocessing the standard BH ringdown (at the horizon) using a transfer function $\mathcal{K}$, which encodes the information about the physical properties of the remnant, such as its reflectivity. Our approach is based on this framework, but we extended its scope to gravitational perturbations of *spinning* ECOs. Our goal is to model the echo signal *analytically*, following a prescription similar to that of the nonspinning case studied in Ref. [2]. The key difference between the present chapter and Ref. [2] is that in the latter the effective potential for the perturbations of the Schwarzschild geometry was approximated using a Pöschl-Teller potential [46, 47] in order to obtain an analytical solution for BH perturbations. In this chapter, we use a low-frequency approximation to solve Teukolsky's equation analytically. We get an analytical transfer function (see Eq. (2.18) below) by approximating the BH reflection ($\mathcal{R}_{\rm BH}$) and transmission ($\mathcal{T}_{\rm BH}$) coefficients. Our final template is provided in a ready-to-be-used form in a supplemental Mathematica® notebook [1].

Background

We consider a spinning compact object with radius r_0, whose exterior geometry ($r > r_0$) is described by the Kerr metric [3, 18, 36, 45]. Unlike the case of spherically symmetric spacetimes, the absence of Birkhoff's theorem in axisymmetry does not ensure that the vacuum region outside a spinning object is described by the Kerr geometry. This implies that the multipolar structure of a spinning ECO might be different from that of a Kerr BH [48, 49]. Nevertheless, for perturbative solutions to the vacuum Einstein's equation that admit a smooth BH limit, all multipole moments of the external spacetime approach those of a Kerr BH in the high-compactness regime [48] (for specific examples, see [50–55]).

Therefore, in Boyer-Lindquist coordinates, the line element at $r > r_0$ reads

$$\begin{aligned} ds^2 &= -\left(1-\frac{2Mr}{\Sigma}\right)dt^2 + \frac{\Sigma}{\Delta}dr^2 - \frac{4Mr}{\Sigma}a\sin^2\theta d\phi dt \\ &+ \Sigma d\theta^2 + \left[(r^2+a^2)\sin^2\theta + \frac{2Mr}{\Sigma}a^2\sin^4\theta\right]d\phi^2\,. \end{aligned} \tag{2.1}$$

In the above equation $\Sigma = r^2 + a^2\cos^2\theta$ and $\Delta = r^2 + a^2 - 2Mr = (r - r_+)(r - r_-)$, where $r_\pm = M \pm \sqrt{M^2 - a^2}$; M and $J \equiv aM \equiv \chi M^2$ are the total mass and angular momentum of the object respectively.

The properties of the object's interior and surface can be parametrized in terms of boundary conditions at $r = r_0$, in particular by a complex and (possibly) frequency-and-spin-dependent reflection coefficient, $\mathcal{R}$ [3, 31]. Motivated by models of microscopic corrections at the horizon scale, in the following we focus on the case

$$r_0 = r_+(1+\epsilon) \qquad 0 < \epsilon \ll 1\,, \tag{2.2}$$

where r_+ is the location of the would-be horizon. We fix r_0 (or, equivalently, ϵ), by requiring the location of the surface to be at a proper length $\delta \ll M$ from r_+, where

$$\delta = \int_{r_+}^{r_0} dr\, \sqrt{g_{rr}}|_{\theta=0}\,. \tag{2.3}$$

This implies

$$\epsilon \simeq \sqrt{1-\chi^2}\frac{\delta^2}{4r_+^2}\,, \tag{2.4}$$

in the $\delta/M \ll 1$ limit.

We shall use M, χ, and δ/M to parametrize the background geometry, and $\mathcal{R}$ to model the boundary conditions for perturbations.

Linear perturbations

Scalar, electromagnetic and gravitational perturbations in the exterior Kerr geometry are described by Teukolsky's master equations [56–58], the radial solution of which shall be denoted by ${}_sR_{lm}(r,\omega)$ (see Appendix 2.A).

It is convenient to make a change of variables by introducing the Detweiler's function [4, 59]

$$\tilde{\Psi} = \Delta^{s/2}\sqrt{r^2+a^2}\left[\alpha\,{}_sR_{lm} + \beta\Delta^{s+1}\frac{d_sR_{lm}}{dr}\right]\,, \tag{2.5}$$

where α and β are certain radial functions [4, 59] that satisfy the following relation:

$$\alpha^2 - \alpha'\beta\Delta^{s+1} + \alpha\beta'\Delta^{s+1} - \beta^2\Delta^{2s+1}V_S = \text{constant}\,. \tag{2.6}$$

The radial potential V_S is defined below in Eq. (2.12), and $s = 0, \pm1, \pm2$ for scalar, electromagnetic and gravitational perturbations, respectively. By introducing the tortoise coordinate x, defined as

$$\frac{dx}{dr} = \frac{r^2+a^2}{\Delta}\,, \tag{2.7}$$

Teukolsky's master equation becomes

$$\frac{d^2\tilde{\Psi}}{dx^2} - V(r,\omega)\tilde{\Psi} = \tilde{S}\,. \tag{2.8}$$

Here $\tilde{S}$ is a source term and the effective potential reads as

$$V(r,\omega) = \frac{U\Delta}{(r^2+a^2)^2} + G^2 + \frac{dG}{dx}\,, \tag{2.9}$$

with

$$G = \frac{s(r-M)}{r^2+a^2} + \frac{r\Delta}{(r^2+a^2)^2}\,, \tag{2.10}$$

$$U = V_S + \frac{2\alpha' + (\beta'\Delta^{s+1})'}{\beta\Delta^s}\,, \tag{2.11}$$

$$V_S = -\frac{1}{\Delta}\left[K^2 - is\Delta' K + \Delta(2isK' - \lambda_s)\right]\,, \tag{2.12}$$

and $K = (r^2+a^2)\omega - am$. The prime denotes a derivative with respect to r. Remarkably, the functions α and β can be chosen such that the resulting potential (2.9) is purely real [4, 59]. Although the choice of α and β is not unique, $\tilde{\Psi}$ evaluated at the asymptotic infinities ($x \to \pm\infty$) remains unchanged up to a phase. Therefore, the energy and angular momentum fluxes are not affected [60].

The asymptotic behavior of the potential is

$$V \to \begin{cases} -\omega^2 & \text{as } x \to +\infty \\ -k^2 & \text{as } x \to -\infty \end{cases}\,, \tag{2.13}$$

where $k = \omega - m\Omega$ and $\Omega = a/(2Mr_+)$ is the angular velocity at the event horizon of a Kerr BH.

Transfer function

Equation (2.8) is formally equivalent to the static scalar case [31] and can be solved using Green's function techniques. At asymptotic infinity, we require the solution of Eq. (2.8) to be an outgoing wave, $\tilde{\Psi}(\omega, x \to \infty) \sim \tilde{Z}^+(\omega)e^{i\omega x}$. Similarly to what is shown in Ref. [31] we have

$$\tilde{Z}^+(\omega) = \tilde{Z}^+_{\rm BH}(\omega) + \mathcal{K}(\omega)\tilde{Z}^-_{\rm BH}(\omega)\,. \tag{2.14}$$

In the above equation, $\tilde{Z}^\pm_{\rm BH}$ are the responses of a Kerr BH (at infinity and near the horizon, for the plus and minus signs, respectively) to the source $\tilde{S}$, i.e.

$$\tilde{Z}^\pm_{\rm BH}(\omega) = \frac{1}{W_{\rm BH}}\int_{-\infty}^{+\infty} dx \tilde{S}\tilde{\Psi}_\mp\,, \tag{2.15}$$

where $\tilde{\Psi}_\pm$ are two independent solutions of the homogeneous equation associated to Eq. (2.8) such that

$$\tilde{\Psi}_+(\omega,x) \sim \begin{cases} e^{+i\omega x} & \text{as } x \to +\infty \\ B_{\rm out}(\omega)e^{+ikx} + B_{\rm in}(\omega)e^{-ikx} & \text{as } x \to -\infty \end{cases}\,, \tag{2.16}$$

$$\tilde{\Psi}_{-}(\omega,x) \sim \begin{cases} A_{\rm out}(\omega)e^{+i\omega x} + A_{\rm in}(\omega)e^{-i\omega x} & \text{as } x \to +\infty \\ e^{-ikx} & \text{as } x \to -\infty \end{cases} , \tag{2.17}$$

and $W_{\rm BH} = \frac{d\tilde{\Psi}_+}{dx}\tilde{\Psi}_- - \tilde{\Psi}_+\frac{d\tilde{\Psi}_-}{dx} = 2ikB_{\rm out}$ is the Wronskian of the solutions $\tilde{\Psi}_\pm$. The details of the ECO model are all contained in the transfer function, which is formally the same as in Ref. [31], namely[1,2]

$$\mathcal{K}(\omega) = \frac{\mathcal{T}_{\rm BH}\mathcal{R}(\omega)e^{-2ikx_0}}{1-\mathcal{R}_{\rm BH}\mathcal{R}(\omega)e^{-2ikx_0}} , \tag{2.18}$$

where $\mathcal{T}_{\rm BH} = 1/B_{\rm out}$ and $\mathcal{R}_{\rm BH} = B_{\rm in}/B_{\rm out}$ are the transmission and reflection coefficients for waves coming from the *left* of the photon-sphere potential barrier [60–62]. The Wronskian relations imply that $|\mathcal{R}_{\rm BH}|^2 + \frac{\omega}{k}|\mathcal{T}_{\rm BH}|^2 = 1$ for any frequency and spin [63].

Finally, the reflection coefficient at the surface of the object, $\mathcal{R}(\omega)$, is defined such that

$$\tilde{\Psi} \sim e^{-ik(x-x_0)} + \mathcal{R}(\omega)e^{ik(x-x_0)} \qquad \text{as } x \sim x_0 , \tag{2.19}$$

where $|x_0| \gg M$.

The BH reflection coefficient in the low-frequency approximation

In Appendix 2.A we solve Teukolsky's equation analytically in the low-frequency limit for gravitational perturbations. We obtain an analytical expression for $\mathcal{R}_{\rm BH}$ which is accurate when $\omega M \ll 1$ (we call this the low-frequency approximation hereon). This is the most interesting regime for echoes, since they are obtained by reprocessing the post-merger ringdown signal [31], whose frequency content is initially dominated by the BH fundamental QNM ($\omega \lesssim \omega_{\rm QNM} \sim 0.5/M$) and subsequently decreases in time. The photon-sphere barrier acts as a high-pass filter and consequently the frequency content decreases for each subsequent echo. Hence, a low-frequency approximation becomes increasingly more accurate at late times. We quantify this in Sec. 2.3.

From the analysis in Appendix 2.A, we find that

$$\mathcal{R}_{\rm BH}^{\rm LF} = \sqrt{1+Z}e^{i\Phi} , \tag{2.20}$$

[1] A heuristic derivation of Eq. (2.18) guided by an analogy with the geometrical optics is provided in Refs. [2, 17] for the static case.

[2] The phase e^{-2ikx_0} in Eq. (2.18) accounts for waves that travel from the potential barrier to $x = x_0$ and return to the potential barrier after being reflected at the surface. Notice that the definition of the transfer function and, in turn, various subsequent formulas could be simplified by defining $\bar{\mathcal{R}} \equiv \mathcal{R}e^{-2ikx_0}$. We choose to keep the notation of Ref. [31] instead.

where "LF" stands for "low frequency", and

$$Z = 4Q\beta_{sl} \prod_{n=1}^{l} \left(1 + \frac{4Q^2}{n^2}\right) [\omega(r_+ - r_-)]^{2l+1} \tag{2.21}$$

coincides with Starobinski's result for the reflectivity of a Kerr BH [64] (for the sake of generality we wrote it for spin-s perturbations), $\sqrt{\beta_{sl}} = \frac{(l-s)!(l+s)!}{(2l)!(2l+1)!!}$, and $Q = -k\frac{r_+^2+a^2}{r_+-r_-}$. The matched asymptotic expansion presented in Appendix 2.A allows us to extract also the phase $\Phi = \Phi(\omega, \chi)$. Note that Φ depends on the choice of an arbitrary constant in the definition of the tortoise coordinate (see Eq. (2.7)). However, as one would expect, this freedom in the choice of x does not affect $\mathcal{K}(\omega)$, since it cancels out in the product $\mathcal{R}\mathcal{R}_{\text{BH}}$.

Furthermore, the phase of $\mathcal{R}(\omega)$ and $\mathcal{R}_{\text{BH}}$ depends also on the choice of the radial perturbation function, but the combination $\mathcal{R}\mathcal{R}_{\text{BH}}$ which enters the transfer function (2.18) does not depend on this choice, as expected; see Sec. 2.3 for more details.

At low frequencies $\mathcal{R}_{\text{BH}}$ takes the form described in Eq. (2.20), while in the high-frequency regime $\mathcal{R}_{\text{BH}} \sim e^{-2\pi\omega/\kappa_H}$, where $\kappa_H = \frac{1}{2}(r_+ - r_-)/(r_+^2 + a^2)$ is the surface gravity of a Kerr BH [65, 66]. We, then, use a Fermi-Dirac interpolating function to smoothly connect the two regimes:

$$\mathcal{R}_{\text{BH}}(\omega, \chi) = \mathcal{R}_{\text{BH}}^{\text{LF}}(\omega, \chi) \frac{\exp\left(\frac{-2\pi\omega_R}{\kappa_H}\right) + 1}{\exp\left(\frac{2\pi(|\omega| - \omega_R)}{\kappa_H}\right) + 1}, \tag{2.22}$$

where ω_R is the real part of the fundamental QNM of a Kerr BH with spin χ. For $|\omega| \ll \omega_R$ the reflection coefficient reduces to $\mathcal{R}_{\text{BH}}^{\text{LF}}$, whereas it is exponentially suppressed when $|\omega| \gg \omega_R$.

The transition between low and high frequencies is phenomenological and not unique, but the choice of the interpolating function is not crucial since high-frequency ($\omega \gtrsim \omega_R$) signals are not trapped within the photon-sphere and hence are not reprocessed.

Modeling the BH response at infinity

We model the BH response at infinity using the fundamental $l = m = 2$ QNM; extensions to multipole modes are straightforward. We consider a generic linear combination of two independent polarizations, namely [67, 68]

$$
\begin{aligned}
Z^{+}_{\rm BH}(t) \quad &\sim \quad \theta(t-t_0)\left(\mathcal{A}_{+}\cos(\omega_R t+\phi_{+})\right. \\
&\qquad \left. + i\mathcal{A}_{\times}\sin(\omega_R t+\phi_{\times})\right) e^{-t/\tau}\,, \qquad (2.23)
\end{aligned}
$$

so that $\Re[Z^{+}_{\rm BH}]$ and $\Im[Z^{+}_{\rm BH}]$ are the two ringdown polarizations, $h_{+}(t)$ and $h_{\times}(t)$, respectively. In the above relation, $\tau=-1/\omega_I$ is the damping time, $\mathcal{A}_{+,\times}\in\Re$ and $\phi_{+,\times}\in\Re$ are respectively the amplitudes and the phases of the two polarizations, and t_0 parametrizes the starting time of the ringdown. Note that Eq. (2.23) is the most generic expression for the fundamental $l=m=2$ ringdown and requires that $\mathcal{A}_{+,\times}$ and $\phi_{+,\times}$ are four independent parameters. The most relevant case of a binary BH ringdown is that of circularly polarized waves [68], which can be obtained from Eq. (2.23) by setting $\mathcal{A}_{+}=\mathcal{A}_{\times}$ and $\phi_{+}=\phi_{\times}$. In the following we provide a template for the generic expression (2.23), but for simplicity in the analysis we shall restrict to $\mathcal{A}_{\times}=0$, i.e. to linearly polarized waves.

Given that the BH response is in the time domain, the frequency-domain waveform can be obtained through a Fourier transform,

$$
\tilde{Z}^{\pm}_{\rm BH}(\omega)=\int_{-\infty}^{+\infty}\frac{dt}{\sqrt{2\pi}}Z^{\pm}_{\rm BH}(t)e^{i\omega t}, \qquad (2.24)
$$

which at infinity simplifies to

$$
\begin{aligned}
\tilde{Z}^{+}_{\rm BH}(\omega)\sim\frac{e^{i\omega t_0}}{2\sqrt{2\pi}} \quad &\left(\frac{\alpha_{1+}\mathcal{A}_{+}-\alpha_{1\times}\mathcal{A}_{\times}}{\omega-\omega_{\rm QNM}}\right. \\
&\left. +\frac{\alpha_{2+}\mathcal{A}_{+}+\alpha_{2\times}\mathcal{A}_{\times}}{\omega+\omega^{*}_{\rm QNM}}\right)\,, \qquad (2.25)
\end{aligned}
$$

where $\omega_{\rm QNM}=\omega_R+i\omega_I$, $\alpha_{1+,\times}=ie^{-i(\phi_{+,\times}+t_0\omega_{\rm QNM})}$, and $\alpha_{2+,\times}=-\alpha^{*}_{1+,\times}$.

Modeling the BH response at the horizon

Moving to the near-horizon BH response, we focus on $Z^{-}_{\rm BH}$, which is the quantity reprocessed by the transfer function (see Eq. (2.14)). Here we generalize the approach of Ref. [2], which considered a source localized near the surface of the ECO. Inspection of Eq. (2.15) reveals that $Z^{-}_{\rm BH}(\omega)$ in general contains the same poles in the complex frequency plane as $Z^{+}_{\rm BH}(\omega)$. Therefore, the near-horizon response at intermediate times can be written as in Eq. (2.25) with different amplitudes and phases. Nonetheless, for a given source, $Z^{+}_{\rm BH}(\omega)$ and $Z^{-}_{\rm BH}(\omega)$ are related to each other in a non-trivial fashion through Eq. (2.15). Let us assume that the source has support only in the interior of the object, i.e., on the left of the effective potential barrier, where $V \approx -k^2$. This is a reasonable assumption, since the source in the exterior can hardly perturb the spacetime within the cavity and therefore its contribution is expected to be subdominant (for example see Refs. [9, 69]). In this case, it is easy to show that

$$\tilde{Z}^{-}_{\rm BH} = \frac{\mathcal{R}_{\rm BH}}{\mathcal{T}_{\rm BH}}\tilde{Z}^{+}_{\rm BH} + \frac{1}{\mathcal{T}_{\rm BH}W_{\rm BH}}\int_{-\infty}^{+\infty} dx\, \tilde{S}e^{ikx}\,. \tag{2.26}$$

Using Eqs. (2.15) and (2.16) and the fact that $\tilde{S}$ has support only where $V \approx -k^2$, the above equation can be written as

$$\tilde{Z}^{-}_{\rm BH} = \frac{\mathcal{R}_{\rm BH}\tilde{Z}^{+}_{\rm BH} + \tilde{\mathcal{Z}}^{+}_{\rm BH}}{\mathcal{T}_{\rm BH}}\,, \tag{2.27}$$

where $\tilde{\mathcal{Z}}^{+}_{\rm BH}$ is the BH response at infinity to an *effective* source $\tilde{\mathcal{S}}(\omega, x) = \tilde{S}(\omega, x)e^{2ikx}$ within the cavity. As such, the ringdown part of $\tilde{\mathcal{Z}}^{+}_{\rm BH}$ can also be generically written as in Eq. (2.25) but with different amplitudes, phases, and starting time. Note that Eq. (2.27) is valid for any source (with support only in the cavity) and for any spin.

Two interesting features of Eq. (2.27) are noteworthy. First, in the final response (Eq. (2.14)) the term $\mathcal{T}_{\rm BH}$ in the denominator of Eq. (2.27) cancels out with that in the transfer function, Eq. (2.18). Second, Eq. (2.27) does not require an explicit modeling of the source. More precisely, although both $\tilde{Z}^{+}_{\rm BH}$ and $\tilde{\mathcal{Z}}^{+}_{\rm BH}$ are linear in the source, they can be written as in Eq. (2.25) which depends on amplitudes, phases, and starting time of the ringdown. Thus, Eq. (2.27) can be computed *analytically* using the expressions for $\mathcal{R}_{\rm BH}$ and $\mathcal{T}_{\rm BH}$.

δ	proper distance of the surface from the horizon radius r_+
$\mathcal{R}(\omega)$	reflection coefficient at the surface (located at $x = x_0(\delta)$ in tortoise coordinates)
M	total mass of the object
χ	angular momentum of the object
$\mathcal{A}_{+,\times}$	amplitudes of the two polarizations of the BH ringdown at infinity
$\phi_{+,\times}$	phases of the two polarizations of the BH ringdown at infinity
t_0	starting time of the BH ringdown at infinity

Table 2.1: Parameters of the ringdown+echo template presented in this chapter. The parameter δ and the (complex) function $\mathcal{R}(\omega)$ characterize the ECO. The remaining seven parameters characterize the most generic fundamental-mode BH ringdown. For circularly polarized waves ($\mathcal{A}_+ = \mathcal{A}_\times$ and $\phi_+ = \phi_\times$) or for linearly polarized waves (for example $A_\times = 0$), the number of ordinary BH ringdown parameters reduces to 5.

Ringdown+echo template for spinning ECOs

We can now put together all the ingredients previously derived. The ringdown+echo template in the frequency domain is given by Eq. (2.14). As already mentioned, by substituting Eq. (2.27) in the transfer function $\mathcal{K}$ [Eq. (2.18)], the dependence on $\mathcal{T}_{\rm BH}$ of the second term in Eq. (2.14) disappears and one needs to model only the reflection coefficient $\mathcal{R}_{\rm BH}$. Clearly, for $\mathcal{R} = 0$ one recovers a single-mode BH ringdown template in the frequency domain.

The extra term in Eq. (2.14) associated with the echoes reads

$$\mathcal{K}\tilde{Z}^{-}_{\rm BH} = \frac{\mathcal{R}e^{-2ikx_0}}{1-\mathcal{R}_{\rm BH}\mathcal{R}e^{-2ikx_0}}\left(\mathcal{R}_{\rm BH}\tilde{Z}^{+}_{\rm BH} + \tilde{\mathcal{Z}}^{+}_{\rm BH}\right) , \tag{2.28}$$

where $\mathcal{R}_{\rm BH}$ is given by Eq. (2.22) and $\tilde{Z}^{+}_{\rm BH}$ is given by Eq. (2.25). Note that, while $\mathcal{R}_{\rm BH}$ depends on the arbitrary constant associated to the tortoise coordinate [Eq. (2.7)], the final expression Eq. (2.28) does not, as expected.

Remarkably, Eq. (2.28) does not depend *explicitly* on the source, the latter being entirely parametrized in terms of $Z^{+}_{\rm BH}$ and $\mathcal{Z}^{+}_{\rm BH}$, i.e. in terms of the amplitudes of BH ringdown. Since the two terms in Eq. (2.28) are additive, in the following we shall focus only on the first one, in which the source is parametrized in terms of $Z^{+}_{\rm BH}$ only. Namely, we shall use

$$\mathcal{K}\tilde{Z}^{-}_{\rm BH} = \frac{\mathcal{R}_{\rm BH}\mathcal{R}e^{-2ikx_0}}{1-\mathcal{R}_{\rm BH}\mathcal{R}e^{-2ikx_0}}\tilde{Z}^{+}_{\rm BH} . \tag{2.29}$$

A discussion on the expressions for $\tilde{\mathcal{Z}}^{+}_{\rm BH}$ in terms of different sources is given in Appendix 2.B. Thus, the final template depends on seven "BH" parameters (M, χ, $\mathcal{A}_{+,\times}$, $\phi_{+,\times}$, t_0) plus two "ECO" quantities: δ (which sets the location of the surface or, equivalently, the compactness of the object) and the complex, frequency-dependent reflection coefficient $\mathcal{R}(\omega)$, see Table 2.1.

The template presented above is publicly available in a ready-to-be-used supplemental MATHEMATICA® notebook [1].

2.3 Properties of the template

Comparison with the numerical results

Our analytical template agrees very well with the exact numerical results at low frequency. A representative example is shown in Fig. 2.1, where we compare the (complex) BH reflection coefficient $\mathcal{R}_{\rm BH}$ (left panels) and the echo template (right panels) against the result of a numerical integration of Teukolsky's equation. In the

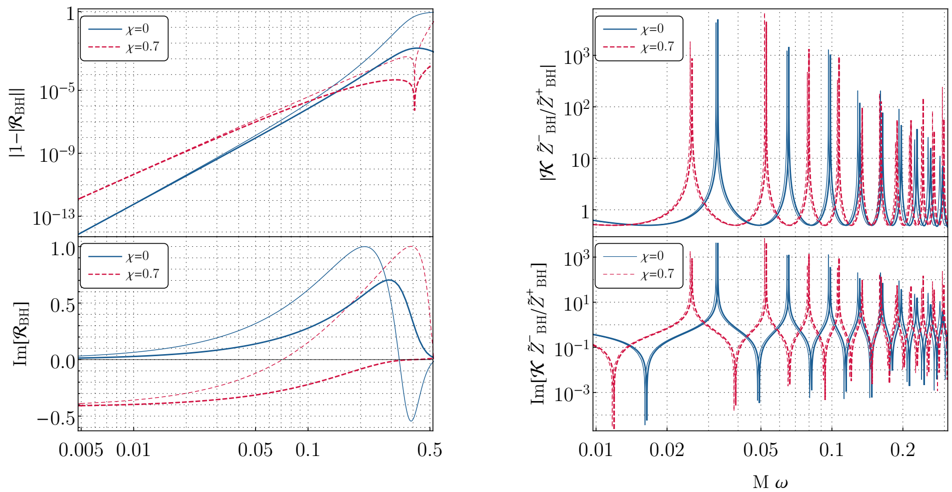

Figure 2.1: Comparison between our analytical template (thick curves) and the result of a numerical integration of Teukolsky's equation (thin curves) for $\chi = 0$ and $\chi = 0.7$. Left panels: the (complex) BH reflection coefficient. Note that the dip in the spinning case corresponds to the threshold of superradiance, i.e. $|\mathcal{R}_{\rm BH}|^2 > 1$ when $\omega < m\Omega$. Right panels: the absolute value (top) and the imaginary part (bottom) of the ECO response $\mathcal{K}\tilde{Z}^-_{\rm BH}/\tilde{Z}^+_{\rm BH}$ as functions of the frequency. For all panels we chose $l = m = 2$ and, for the right panels, $\delta/M = 10^{-10}$ and $\mathcal{R} = 1$.

right panels of Fig. 2.1 we show the quantity $\mathcal{K}Z^-_{\rm BH}$, normalized by the standard BH response $Z^+_{\rm BH}$; since $Z^-_{\rm BH}$ is proportional to $Z^+_{\rm BH}$, the final result is independent of the specific BH response. The agreement (both absolute value and imaginary part) is very good at low frequencies, whereas deviations are present in the transition region where $\omega M \sim 0.1$. Crucially, the low-frequency resonances — which dominate the response [19, 27] — are properly reproduced.

Notice that the agreement between analytics and numerics improves as $\delta \to 0$, since the ECO QNMs are at lower frequency (for moderate spin) in this regime and our framework is valid. For technical reasons we were able to produce numerical results up to $\delta = 10^{-10}M$, but we expect that the agreement would improve significantly for more realistic (and significantly smaller) values, when δ is of the order of the Planck length.

To quantify the agreement, we compute the overlap

$$\mathcal{O} = \frac{|\langle \tilde{h}_A|\tilde{h}_N\rangle|}{\sqrt{|\langle \tilde{h}_N|\tilde{h}_N\rangle||\langle \tilde{h}_A|\tilde{h}_A\rangle|}} \tag{2.30}$$

between the analytical signal, $\tilde{h}_A$, and the numerical one, $\tilde{h}_N$, where the inner product is defined as

$$\langle \tilde{X} | \tilde{Y} \rangle \equiv 4\Re \int_0^\infty \frac{\tilde{X}(f)\tilde{Y}^*(f)}{S_n(f)} df \,, \tag{2.31}$$

(or in a certain frequency range), S_n is the detector's noise spectral density, and $f = \omega/(2\pi)$ is the GW frequency.

When $|\mathcal{R}| \sim 1$ the presence of very high and narrow resonances makes a quantitative comparison challenging, since a slight displacement of the resonances (due for instance to finite-ω truncation errors) deteriorates the overlap. For instance, for a representative case shown in Fig. 2.1 ($\delta = 10^{-10}M$, $\chi = 0.7$, and $\mathcal{R} = 1$) the overlap is excellent ($\mathcal{O} \gtrsim 0.999$) when the integration is performed before the first resonance, but it quickly reduces to zero after that. To overcome this issue, we compute the overlap in the case in which the resonances are less pronounced, as it is the case when $|\mathcal{R}| < 1$. Let us consider $M = 30\, M_\odot$, $\chi = 0.7$, $\delta = 10^{-10}M$, and the aLIGO noise spectral density [70]. For $\mathcal{R} = 0.9$, the overlap in the range $f \in (20, 100)$ Hz (whose upper end roughly corresponds to the limit $\omega M \sim 0.1$ beyond which the low-frequency approximation is not accurate) is $\mathcal{O} = 0.48$. This small value is mostly due to a small displacement of the resonances. Indeed, by shifting the mass of the analytical waveform by only 1.6%, the overlap increases significantly, $\mathcal{O} = 0.995$. For $\mathcal{R} = 0.8$ and in the same conditions, we get $\mathcal{O} \approx 0.8$ without mass shift and $\mathcal{O} \gtrsim 0.999$ with the same mass shift as above with the mass shift indicated above. As $\delta \to 0$, the shift in the mass decreases since the exact resonant frequencies are better reproduced.

Time-domain echo signal: modulation and mixing of the polarizations

The time-domain signal can be computed through an inverse Fourier transform,

$$h(t) = \frac{1}{\sqrt{2\pi}} \int_{-\infty}^{+\infty} d\omega \tilde{Z}^+(\omega) e^{-i\omega t} \,, \tag{2.32}$$

where $\Re[h(t)]$ and $\Im[h(t)]$ are the two polarizations of the wave, respectively.

In Fig. 2.2 we present a representative slideshow of our template for different values of $\mathcal{R}$ and spins. For simplicity, we consider $\delta/M = 10^{-7}$ and $\mathcal{R}(\omega) = $ const (but generically complex). The time-domain waveform contains all the features previously reported for the echo signal, in particular amplitude and frequency modulation [2, 6, 7, 15, 16].

In addition, the spin of the object and the phase of the reflectivity coefficient introduce novel effects, such as a nontrivial amplitude modulation of subsequent echoes. This is mostly due to the spin-and-frequency dependence of the phase of $\mathcal{R}_{\rm BH}$ and $\mathcal{R}$. The effect of the spin can be seen by comparing the left column ($\chi = 0$) of Fig. 2.2 with the middle ($\chi = 0.7$) and the right columns ($\chi = 0.9$). Note that the phase of each subsequent echo depends on the combination $\mathcal{R}\mathcal{R}_{\rm BH}$, i.e., on the combined action of the reflection by the surface and by the BH barrier. Thus, phase inversion [2, 18, 36] of each echo relative to the previous one occurs whenever $\mathcal{R}\mathcal{R}_{\rm BH} \approx -1$ for low frequencies (cf. Sec. 2.3 for more details).

Furthermore, note that the first, the second, and the fourth row of Fig. 2.2 all correspond to perfect reflectivity, $|\mathcal{R}| = 1$, but their echo structure is different: in other words, a phase term in $\mathcal{R}$ introduces a nontrivial echo pattern. To the best of our knowledge this effect was neglected in the previous analyses.

As shown in Fig. 2.2 the time-domain signal can contain both plus and cross polarizations, even if the initial ringdown is purely plus polarized (i.e., $\mathcal{A}_\times = 0$). This interesting property can be explained as follows. In the nonspinning case, and provided

$$\mathcal{R}_{\chi=0}(\omega) = \mathcal{R}^*_{\chi=0}(-\omega^*)\,, \tag{2.33}$$

the transfer function satisfies the symmetry property

$$\mathcal{K}_{\chi=0}(\omega) = \mathcal{K}^*_{\chi=0}(-\omega^*)\,. \tag{2.34}$$

The time domain echo waveforms are real (resp., imaginary) if the ringdown waveform is real (resp., imaginary). In this case, the echo signal contains the same polarization of the BH ringdown and the two polarizations do not mix. In particular, Eq. (2.33) is satisfied when $\mathcal{R}$ is real.

Remarkably, this property is broken in the following cases:

1. when $\mathcal{R}$ is complex and does not satisfy Eq. (2.33), as in the second row of Fig. 2.2;

2. generically in the spinning case, even when $\mathcal{R}$ is real[3] or when it satisfies Eq. (2.33).

[3] In this case the transfer function satisfies an extended version of Eq. (2.34), namely

$$\mathcal{K}(\omega, m) = \mathcal{K}^*(-\omega^*, -m) \tag{2.35}$$

which, however, does not prevent the mixing of the polarizations, due to the $m \to -m$ transformation.

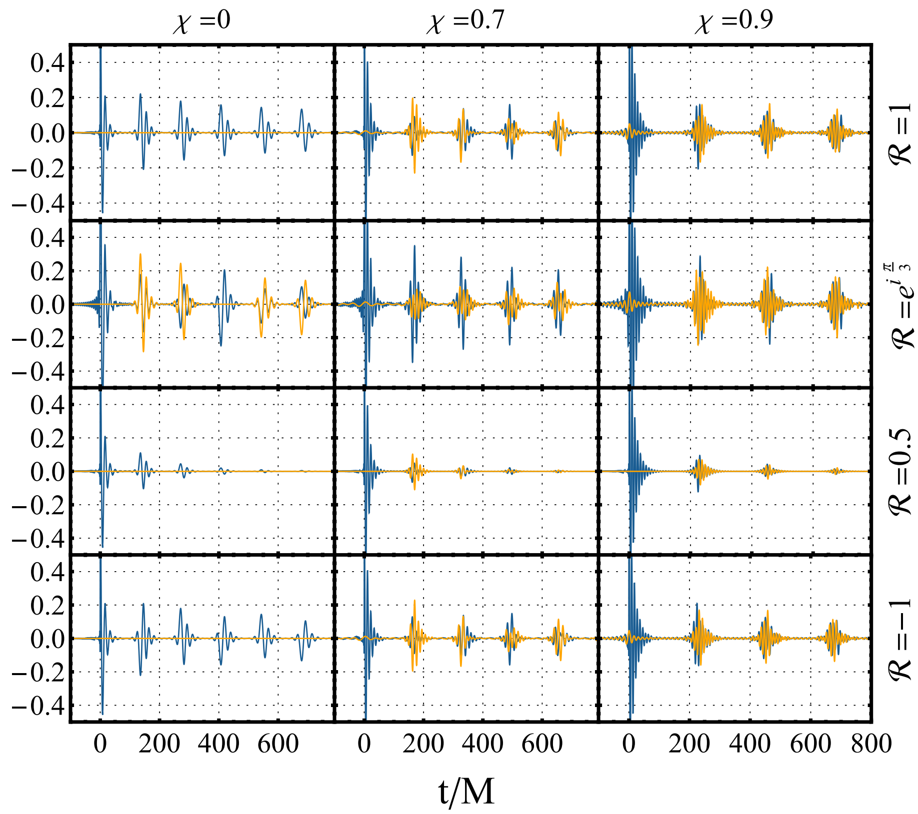

Figure 2.2: Examples of the gravitational ringdown+echo template in the time domain for different values of $\mathcal{R}(\omega)$ = const, and object's spin χ. We consider $\delta/M = 10^{-7}$. We plot the real (blue curve) and the imaginary (orange curve) parts of the waveform, corresponding to the plus and cross polarization, respectively (note that the ringdown signal is purely plus-polarized, i.e. $\mathcal{A}_\times = 0$). Each waveform is normalized to the peak of $|\Re[h(t)]|$ during the ringdown (the peak is not shown in the range of the y axis to better visualize the subsequent echoes). Additional waveforms are provided online [1].

In either case *mixing of the polarizations* occurs. For instance, if the BH ringdown is (say) a plus-polarized wave ($\mathcal{A}_\times = 0$), it might acquire a cross-polarization component upon reflection by the photon-sphere barrier (if $\chi \neq 0$) or by the surface (if $\mathcal{R}$ is complex and does not satisfy Eq. (2.33)). Therefore, even when the ringdown signal is linearly polarized (as when $\mathcal{A}_\times = 0$, the case considered in Fig. 2.2), generically the final echo signal is not.

The mixing of polarizations can be used to explain the involved echo patter shown in some panels of Fig. 2.2. For example, for $\chi = 0$ and $\mathcal{R} = e^{i\pi/3}$ each echo is multiplied by $e^{i\pi/3}$ relative to the previous one. Therefore, every three echoes the imaginary part of the signal (i.e., the cross polarization) is zero.

Another interesting consequence of the polarization mixing is the fact that the amplitude of subsequent echoes in each polarization does not decrease monotonically. This is evident, for example, in the panels of Fig. 2.2 corresponding to $\chi = 0.7$, $\mathcal{R} = 1$ and $\chi = 0$, $\mathcal{R} = e^{i\pi/3}$. However, it can be checked that the absolute value of the signal (related to the energy) decreases monotonically.

Decay at late times and superradiant instability

The involved behavior discussed above simplifies at very late times. In this case — when the dominant frequency is roughly $\omega \approx \omega_R^{\rm ECO} \ll 1/M$ (where $\omega_R^{\rm ECO}$ is the real part of the fundamental QNM of the ECO) — the amplitude of the echoes always decreases as [2]

$$|h_{\rm peaks}(t)| \propto |\mathcal{R}\mathcal{R}_{\rm BH}|^{\frac{t}{2|x_0|}}\,, \tag{2.36}$$

where both $\mathcal{R}$ and $\mathcal{R}_{\rm BH}$ are evaluated at $\omega_R^{\rm ECO} \ll 1/M$. The above scaling agrees almost perfectly with our time-domain waveforms, especially at late times.

More interestingly, Eq. (2.36) shows that the signal at late time should *grow* when $|\mathcal{R}\mathcal{R}_{\rm BH}| > 1$, i.e., when the combined action of reflection by the surface and by the BH barrier yields an amplification factor larger than unity [3, 4]. When $|\mathcal{R}| \approx 1$, this condition requires

$$|\mathcal{R}_{\rm BH}| > 1\,. \tag{2.37}$$

From Eq. (2.21), it is easy to see that this occurs when

$$\omega(\omega - m\Omega) < 0\,, \tag{2.38}$$

i.e., when the condition for superradiance [58, 71] is satisfied (see Ref. [39] for an overview). Thus, we expect the signal to grow in time over a time scale given by the ergoregion instability [3, 4, 38–41, 72] of spinning horizonless ultracompact objects. Indeed, the QNM spectrum of the object contains unstable modes when $\omega_R < m\Omega$ [3, 4, 40, 41]. The instability time scale is always much longer than the dynamical time scale of the object (e.g., $\tau_{\rm instab} \gtrsim 10^5 M$ for $\chi = 0.5$ [4]).

When the signal grows in time due to the ergoregion instability the waveform $h(t)$ is a nonintegrable function, so its Fourier transform cannot be defined. For this reason the frequency-domain waveforms are valid up to $t \lesssim \tau_{\rm instab}$. Since the instability time scale is much longer than the echo delay time, the time interval of validity of our waveform still includes a large number of echoes. In particular, the ergoregion instability does not affect the first $N \sim |\log \delta/M|$ echoes [17].

As discussed in Refs. [3, 4], this instability can be quenched if $|\mathcal{R}\mathcal{R}_{\rm BH}| < 1$, which requires a partially absorbing ECO, $|\mathcal{R}| < 1$ (see Refs. [9, 69] for a specific model where the instability is absent).

Energy of echo signal

The energy contained in the ringdown+echo signal is shown in Fig. 2.3, where we plot the quantity

$$E \propto \int_{-\infty}^{\infty} d\omega\, \omega^2 |\hat{Z}^+|^2 \,, \tag{2.39}$$

normalized by the one corresponding to the ringdown alone, $E_{\rm RD} \equiv E(\mathcal{R}=0)$, as a function of the reflectivity $\mathcal{R}$ and for several values of the spin χ. We use the prescription of Ref. [73] to compute the ringdown energy, i.e. $\tilde{Z}^+_{\rm BH}$ is the frequency-domain full response obtained by using the Fourier transform of

$$Z^+_{\rm BH}(t) \sim \mathcal{A}_+ \cos(\omega_R t + \phi_+) e^{-|t|/\tau} \,. \tag{2.40}$$

(Notice the absolute value of t at variance with Eq. (2.23).) This prescription circumvents the problem associated with the Heaviside function in Eq. (2.23) that produces a spurious high-frequency behavior in the energy flux, leading to infinite energy in the ringdown signal. With the above prescription, the energy defined in Eq. (2.39) is finite and reduces to the result of Ref. [73] for the BH ringdown when $\mathcal{R} = 0$.

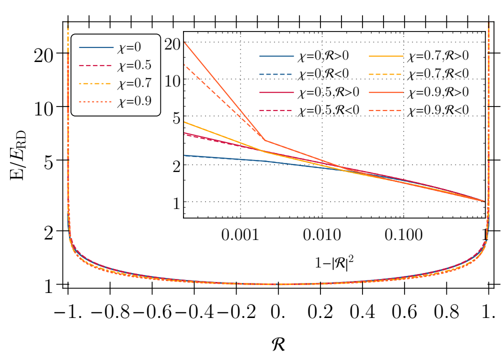

Figure 2.3: Total energy contained in the ringdown+echo signal normalized by that of the ringdown alone as a function of $\mathcal{R}$ and for various values of the spin χ. The total energy is much larger than the ringdown energy only when $\mathcal{R} \to 1$. We set $\delta/M = 10^{-5}$ and considered only one ringdown polarization with $\phi_+ = 0$; the result is independent of δ in the $\delta \ll M$ limit.

Because of reflection at the surface, the energy contained in the full signal for a fixed amplitude might be much larger than that of the ringdown itself. Overall, the normalized energy depends mildly on the spin, but much more strongly on $\mathcal{R}$: the energy contained in the echo part of the signal grows fast as $|\mathcal{R}| \to 1$ (reaching a maximum value that depends on the spin and might become larger than the energy of the ringdown alone). This is due to the resonances corresponding to the low-frequency QNMs of the ECO, which can be excited with large amplitude [19] (see bottom panel of Fig. 2.1), and suggests that GW echoes might be detectable even when the ringdown is not if $|\mathcal{R}| \approx 1$. However, it is worth noticing that these low-frequency resonances are excited only at late times and therefore the first few echoes contain a small fraction of the total energy of the signal. When $\mathcal{R}$ is significantly smaller than unity subsequent echoes are suppressed (see third row in Fig. 2.2) and their total energy is modest compared to that of the ringdown.

Note also that when $|\mathcal{R}| \approx 1$ the total energy is expected to diverge in the superradiant regime, due to the aforementioned ergoregion instability. This is not captured by the inverse Fourier transform $\hat{Z}^+(\omega)$, since the time-domain signal is non-integrable when $t \gtrsim \tau_{\rm instab}$.

Frequency content of the signal

As previously discussed, the photon-sphere barrier acts as a high-pass filter as a consequence of which each echo has a lower frequency content than the previous one. This is confirmed by Fig. 2.4, where we display the first four echoes for $\mathcal{R} = 1$, $\chi = 0$, and $\delta/M = 10^{-7}$, shifted in time and rescaled in amplitude so that their global maxima are aligned.

The frequency content of the total signal starts roughly at the BH QNM frequency, and slowly decreases in each subsequent echo until it is dominated by the low-frequency ECO QNMs at very late time. This also shows that a low-frequency approximation becomes increasingly more accurate at later times. In the example shown in Fig. 2.4, the frequencies of the first four echoes are approximately $M\omega \approx 0.34, 0.32, 0.3, 0.29$, whereas the real part of the fundamental BH QNM for $\chi = 0$ is $M\omega_R \approx 0.37367$. Therefore, the frequency between the first and the fourth echo decreases by $\approx 17\%$.

Note that the case shown in Fig. 2.4 is the one that provides the simplest echo patter ($\chi = 0$, $\mathcal{R} \in \Re$). The case $\chi \neq 0$ or a complex choice of $\mathcal{R}$ would provide a much more involved patter and polarization mixing.

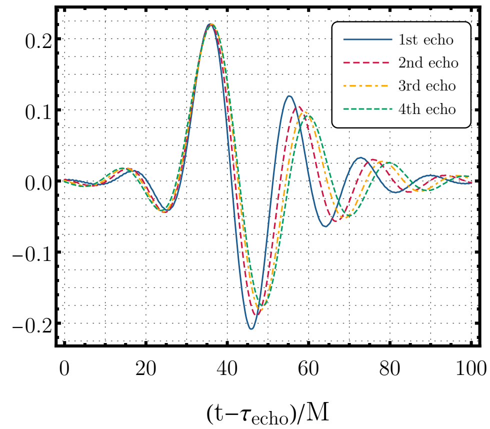

Figure 2.4: The first four echoes in the time-domain waveform for a model with $\mathcal{R} = 1$, $\chi = 0$, $\delta/M = 10^{-7}$. The waveform has been shifted in time and rescaled in amplitude so that the global maxima of each echo are aligned. Note that each subsequent echo has a lower frequency content than the previous one.

Our results show that two qualitatively different situations can occur:

A) the reflectivity $\mathcal{R}$ of the object is small enough so that the amplitude of subsequent echoes is suppressed. In this case most of the signal-to-noise ratio (SNR) is contained in the first few echoes at frequency only slightly smaller than the fundamental BH QNM.

B) the reflectivity $\mathcal{R}$ is close to unity, so subsequent echoes are relevant and contribute significantly to the total SNR. In this case the frequency content becomes much smaller than the fundamental BH QNM.

Clearly our low-frequency approximation is expected to be accurate in case B) and less accurate in case A), especially for high spin where $M\omega_{\rm QNM} \sim 0.5$ or larger.

On the phase of the reflectivity coefficients

It is worth remarking that there exist several definitions of the radial function describing the perturbations of a Kerr metric; these are all related to each other by a linear transformation similar to Eq. (2.5). The BH reflection coefficients that can be defined for each function differ by a phase, while the quantity $|\mathcal{R}_{\rm BH}|^2$ (related to the energy damping/amplification) is invariant [60].

The transfer function in Eq. (2.18) contains both the absolute value and the phase of $\mathcal{R}_{\rm BH}$. Therefore, one might wonder whether this ambiguity in the phase could affect the ECO response. For a given model, it should be noted that the reflectivity coefficient at the surface, $\mathcal{R}$, is also affected by the same phase ambiguity, in accordance with the perturbation variable chosen to describe the problem. Since the transfer function depends only on the combinations $\mathcal{R}\mathcal{R}_{\rm BH}$ and $\mathcal{R}\mathcal{T}_{\rm BH}$, the phase ambiguity in $\mathcal{R}$ cancels out with that in $\mathcal{R}_{\rm BH}$ and $\mathcal{T}_{\rm BH}$ in Eq. (2.18). This ensures that the transfer function is invariant under the choice of the radial perturbation function, as expected for any measurable quantity. For example, at small frequencies the BH reflection coefficient derived from the asymptotics of the Regge-Wheeler function at $x \to -\infty$ has a phase difference of π compared to the BH reflection coefficient computed from the Detweiler function for $\chi = 0$. Consistently, the reflectivity coefficient associated to the former differs by a phase π with respect to the reflectivity coefficient associated to the latter, i.e., if $\bar{\mathcal{R}} = 1$ for Regge-Wheeler then $\bar{\mathcal{R}} = -1$ for Detweiler in the same model, and viceversa.

Therefore, it is natural for $\mathcal{R}$ to have a nontrivial (and generically frequency- and spin- dependent) phase term, whose expression depends on the formulation of the problem. Obviously, all choices of the radial wavefunctions are equivalent but — for the same ECO model — the complex reflection coefficient $\mathcal{R}$ should generically be different for each of them. To the best of our knowledge, this point was neglected in actual matched-filtered searches for echoes, which so far considered $\mathcal{R}$ (and also $\mathcal{R}_{\rm BH}$) to be real.

This fact is particularly important in light of what previously discussed for the mixing of the polarizations. As shown in the second row of Fig. 2.2, a phase in $\mathcal{R}$ introduces a mixing of polarizations for any spin, which results in a more complex shape of the echoes in the individual polarizations of the signal.

Since the phase of $\mathcal{R}$ depends on the specific ECO model, in the analysis of Sec. 2.4 we will parametrize the reflectivity in a model-agnostic way as $\mathcal{R} = |\mathcal{R}|e^{i\phi}$. In principle, both the absolute value and the phase are generically frequency dependent but for simplicity we choose them to be constants or, equivalently, we take the leading-order and low-frequency limit of these quantities. Hence we parametrize our template by $|\mathcal{R}|$ and ϕ, different choices of which correspond to different models.

BH QNMs vs ECO QNMs

It is worth considering the inverse-Fourier transform of Eq. (2.14) (i.e., Eq. (2.32)) and deform the frequency integral in the complex frequency plane. When $\mathcal{R} = 0$ (i.e., standard BH ringdown) this procedure yields three contributions [74, 75]: (i) the high-frequency arcs that govern the prompt response, (ii) a sum-over-residues at the poles of the complex frequency plane (defined by $W_{\rm BH} = 0 = B_{\rm out}$), which correspond to the QNMs and dominate the signal at intermediate times, and (iii) a branch cut on the negative half of the imaginary axis, giving rise to late-time tails due to backscattering off the background curvature.

When $\mathcal{R} \neq 0$, the pole structure is more involved. The extension of the integral in Eq. (2.32) to the complex plane contains two types of complex poles: (i) those associated with $\tilde{Z}^{+}_{\rm BH}(\omega)$ ($\sim 1/W_{\rm BH} \sim 1/B_{\rm out}$) and with $\mathcal{K}\tilde{Z}^{-}_{\rm BH}(\omega)$ ($\sim \mathcal{T}_{\rm BH}/W_{\rm BH} \sim 1/B_{\rm out}^2$) which are the standard BH QNMs (but that do not appear in the ECO QNM spectrum [6]), and (ii) those associated with the poles of the transfer function $\mathcal{K}$ (i.e. when $\mathcal{R}_{\rm BH} = e^{2ikx_0}/\mathcal{R}$), which correspond to the ECO QNMs.

The late-time signal in the post-merger is dominated by the second type of poles, since the latter have a longer damping time and survive longer. The prompt ringdown is dominated by the first type of poles, i.e., by the dominant QNMs of the corresponding BH spacetime [6]. Finally, the intermediate region between prompt ringdown and late-time ECO QNM ringing depends on the other parts of the contour integral on the complex plane. As such, they are more complicated to model, since they do not depend on the QNMs alone and might also depend on the source, as in the standard BH case.

2.4 Projected constraints on ECOs

In this section we use the template derived in Sec. 2.2 for a preliminary error estimation of the ECO properties using current and future GW detectors.

The ringdown+echo signal displays sharp peaks which originate from the resonances of the transfer function $\mathcal{K}$ and correspond to the long-lived QNMs of the ECO [4]. The relative amplitude of each resonance in the signal depends on the source and the dominant modes are not necessarily the fundamental harmonics [31, 33]. We stress that the amplitude of the echo signal depends strongly on the value of $\mathcal{R}$, especially when $|\mathcal{R}| \approx 1$. This suggests that the detectability of (or the constraints on) the echoes strongly depends on $\mathcal{R}$ and would be much more feasible when $|\mathcal{R}| \approx 1$. Below we quantify this expectation using a Fisher matrix technique, which is accurate at large SNR (see, e.g., Ref. [76]). This is performed as in Ref. [2], but by including the spin of the object consistently and allowing for a complex reflection coefficient, $\mathcal{R} = |\mathcal{R}|e^{i\phi}$.

The Fisher information matrix Γ of a template $\tilde{h}(f)$ for a detector with noise spectral density $S_n(f)$ reads as

$$\Gamma_{ij} = \langle \partial_i \tilde{h} | \partial_j \tilde{h} \rangle \,, \tag{2.41}$$

where $i, j = 1, ..., N$, with N being the number of parameters in the template. The SNR ρ is defined such as $\rho^2 = \langle \tilde{h} | \tilde{h} \rangle$. The covariance matrix, Σ_{ij}, of the errors on the template's parameters is the inverse of Γ_{ij} and $\sigma_i = \sqrt{\Sigma_{ii}}$ (no summation) gives the statistical error associated with the measurement of i-th parameter.

We computed numerically the Fisher matrix (2.41) with our template $\tilde{h}(f) \equiv \tilde{Z}^{+}(f)$ using the sensitivity curves of aLIGO with the design-sensitivity `ZERO_DET_high_P` [70] and two configurations for the third-generation (3G) instruments: Cosmic Explorer in the narrow band variant [77, 78], and Einstein Telescope in its `ET-D` configuration [79]. We also consider the LISA's noise spectral density proposed in Ref. [80]. We focus on the most relevant case of gravitational perturbations with $l = m = 2$ and consider $M = 30\,M_\odot$ ($M = 10^6\,M_\odot$) for ground- (space-) based detectors.

As previously discussed, the most generic BH ringdown template contains seven parameters (mass, spin, two phases, two amplitudes, and starting time). For simplicity, we reduce it to a linearly-polarized ringdown. In particular, we do not include $\mathcal{A}_\times$ and $\phi_\times$ in the parameters and inject $\mathcal{A}_\times = 0$. This implies that we have five standard-ringdown parameters in our analysis.

The template also depends on two ECO quantities (the frequency-dependent reflection coefficient $\mathcal{R}(\omega)$ and the parameter δ) which fully characterize the model. The parameter δ is directly related to physical quantities, in particular, the compactness of the ECO or (equivalently) the redshift at the surface. We parametrize the reflectivity coefficient as

$$\mathcal{R}(\omega) = |\mathcal{R}| e^{i\phi} \,, \tag{2.42}$$

where $|\mathcal{R}|$ and ϕ are assumed to be frequency independent for simplicity and we remark that $x_0 = x_0(\delta)$ (see Eq. (2.4)). This yields three ECO parameters: δ, $|\mathcal{R}|$, and ϕ.

We consider two cases: (i) a conservative case in which we extract the errors on all the 5 + 3 parameters in a Fisher matrix framework and (ii) a more optimistic case in which we assume that the standard-ringdown parameters can be independently and reliably measured through the prompt ringdown, so that we are left with the measurements errors on the three ECO parameters.

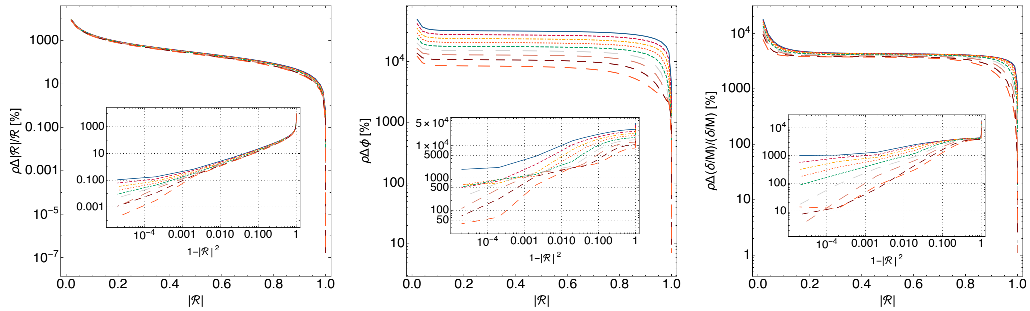

Figure 2.5: Left panel: relative (percentage) error on the reflection coefficient, $\Delta|\mathcal{R}|/|\mathcal{R}|$ multiplied by the SNR, as a function of $|\mathcal{R}|$ for different values of injected spin. The inset shows the same quantity as a function of $1-|\mathcal{R}|^2$ in a logarithmic scale. From top to bottom: $\chi = (0.9, 0.8, 0.7, 0.6, 0.5, 0.4, 0.3, 0.2, 0.1)$. Middle panel: same but for the absolute (percentage) error on the phase ϕ of $\mathcal{R}$, i.e. $\rho\Delta\phi$. Right panel: same as in the left panel but for the compactness parameter, δ, i.e. $\Delta(\delta/M)/(\delta/M)$. We assume $\delta = 10^{-7}M$ but the errors are independent of δ when $\delta/M \ll 1$ [2]. We set $\phi = 0$ for the phase of $\mathcal{R}$ (i.e. we consider a real and positive $\mathcal{R}$, but other choices give very similar results.

Conservative case: $5+3$ parameters

Our main results for the statistical errors on the ECO parameters are shown in Fig. 2.5. In the large SNR limit, the errors scale as $1/\rho$ so we present the quantity $\rho\Delta|\mathcal{R}|/|\mathcal{R}|$ (left panel), $\rho\Delta\phi$ (middle panel), and $\rho\Delta(\delta/M)/(\delta/M)$ (right panel) for several values of the spin. We find that the main qualitative features already discussed in Ref. [2] do not depend significantly on the inclusion of the spin in the template. In particular, for fixed SNR the relative errors are almost independent of the specific sensitivity curve of the detector, at least for signals located near each minimum of the sensitivity curve, as those adopted in Fig. 2.5. In Fig. 2.5 we adopted the LISA curve [80] but other detectors give very similar results for the errors normalized by the SNR.

Furthermore, the statistical errors are almost independent of δ when $\delta/M \ll 1$, whereas they strongly depend on the reflection coefficient $\mathcal{R}$. The reason for this can be again traced back to the presence of resonances as $\mathcal{R} \to 1$. This feature confirms that it should be relatively straightforward to rule out or detect models with $|\mathcal{R}| \approx 1$, whereas it is increasingly more difficult to constrain models with smaller values of $|\mathcal{R}|$.

We also note that the value of the spin of the remnant affects the errors on $|\mathcal{R}|$ only mildly, whereas it has a stronger impact on the phase of $\mathcal{R}$ (probably due to the aforementioned mixing of the polarizations) and a moderate impact on the errors on

δ.

Overall, the specific value of ϕ does not affect the errors significantly, although it is important to include it as an independent parameter in order not to underestimate the errors.

Next, we calculate the SNR necessary to discriminate a partially-absorbing ECO from a BH on the basis of a measurement of $\mathcal{R}$ at some confidence level [2]. Clearly, if $\Delta\mathcal{R}/\mathcal{R} > 100\%$, any measurement would be compatible with the BH case ($\mathcal{R} = 0$). On the other hand, relative errors $\Delta\mathcal{R}/\mathcal{R} < (4.5, 0.27, 0.007, 0.00006)\%$ suggest that it is possible to detect or rule out a given model at $(2, 3, 4, 5)\sigma$ confidence level, respectively. The result of this analysis is shown in Fig. 2.6, where we present the exclusion plot for the parameter $\mathcal{R}$ as a function of the SNR in the ringdown phase only, $\rho_{\rm RD}$. Shaded areas represent regions which can be excluded at some given confidence level. Obviously, larger SNRs would allow to probe values of $\mathcal{R}$ close to the BH limit, $\mathcal{R} \approx 0$. The extent of the constraints strongly depends on the confidence level. For example, SNR ≈ 100 in the ringdown would allow to distinguish ECOs with $|\mathcal{R}|^2 \gtrsim 0.1$ from BHs at 2σ confidence level, but a 3σ detection would be possible only if $|\mathcal{R}|^2 \gtrsim 0.8$. The reason for this is again related to the strong dependence of the echo signal on $\mathcal{R}$. Note that Fig. 2.6 is very similar to that computed in Ref. [2], showing that including the spin and a phase term for $\mathcal{R}$ does not affect the final result significantly.

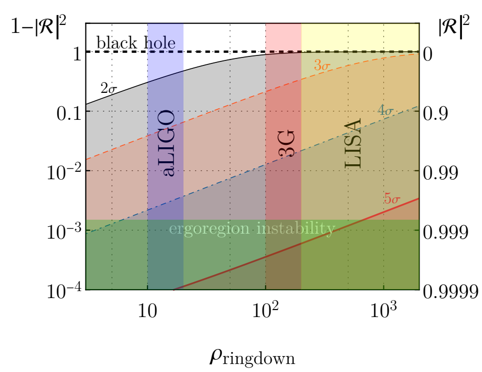

Figure 2.6: Projected exclusion plot for the ECO reflectivity $\mathcal{R}$ as a function of the SNR in the ringdown phase. The shaded areas represent regions that can be excluded at a given confidence level (2σ, 3σ, 4σ, 5σ). Vertical bands are typical SNR achievable by aLIGO/Virgo, 3G, and LISA in the ringdown phase, whereas the horizontal band is the region excluded by the ergoregion instability [3, 4]. We assumed $\chi = 0.7$ for the spin of the merger remnant, the result depends only mildly on the spin.

Optimistic case: 3 ECO parameters

Let us now assume that the standard ringdown parameters (mass, spin, phases, amplitudes, and starting time) can be independently measured through the prompt ringdown signal, which is identical for BHs and ECOs if $\delta/M \ll 1$ [6]. In such case the remaining three ECO parameters ($|\mathcal{R}|$, ϕ, and δ) can be measured a posteriori, assuming the standard ringdown parameters are known.

A representative example for this optimistic scenario is shown in Fig. 2.7. As expected, the errors are significantly smaller, especially those on the phase ϕ of the reflectivity. The errors on $\mathcal{R}$ are only mildly affected, and the projected constraints on $\mathcal{R}$ at different confidence levels are similar to those shown in Fig. 2.6. Nonetheless, we expect this strategy to be much more effective for actual searches.

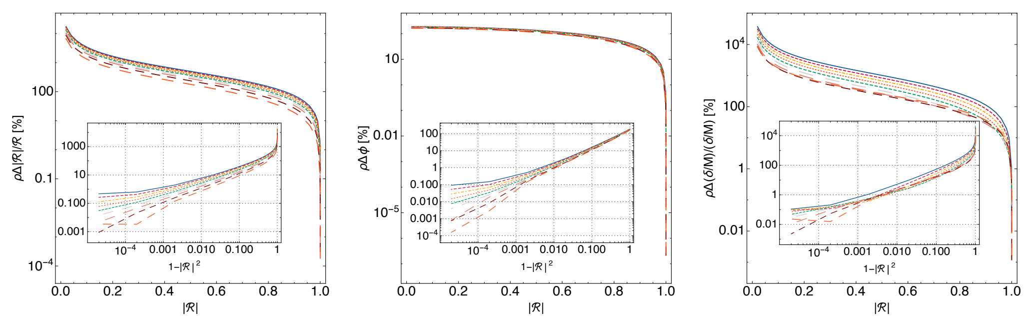

Figure 2.7: Same as in Fig. 2.5 but including only the three ECO parameters ($|\mathcal{R}|$, ϕ, and δ) in the Fisher analysis.

2.5 Discussion

We have presented an analytical template that describes the ringdown and subsequent echo signal of a spinning, ultracompact, Kerr-like horizonless object. This template depends on the physical parameters of the remnant: namely, the mass, the spin, the compactness and the reflection coefficient $\mathcal{R}$ at its surface. The analytical approximation is valid at low frequencies, where most of the SNR of an echo signal is accumulated in the case $|\mathcal{R}| \sim 1$. Our template becomes increasingly accurate at later times as the frequency content of the echo decreases.

The features of the signal are related to the physical properties of the ECO model. The time-domain waveform contains all features previously reported for the echo signal, namely amplitude and frequency modulation and possible phase inversion of each echo relative to the previous one, depending on the reflective boundary conditions. Furthermore, the presence of the spin and of a generically complex reflectivity introduce qualitatively different effects, most notably the amplitude and frequency modulation is more involved (also) due to mixing of the two polarizations. For (almost) perfectly-absorbing spinning ECOs, the perturbations can grow at late times due to superradiance and the ergoregion instability. However, even for highly-spinning remnants, this instability occurs on a time scale which is much longer than the echo delay time, and likely plays a negligible role in actual searches for echoes (see however Ref. [45] for a discussion of the stochastic background produced by this instability). The instability is quenched for partially-reflecting objects [3, 4, 9, 69].

The amplitude of subsequent echoes depends strongly on the reflectivity $\mathcal{R}$. When $|\mathcal{R}| \approx 1$ the echo signal can have energy significantly larger than those of the ordinary BH ringdown. This suggests that GW echoes in certain models might be detectable even when the ringdown is not. Likewise, ruling out models with $|\mathcal{R}| \approx 1$ is significantly easier than for smaller values of the reflectivity.

We have also highlighted the importance of including a model-dependent phase term in the reflection coefficient; this phase also depends on the radial perturbation variable used in the perturbation equation. To the best of our knowledge this issue has been so far neglected in previous analyses (but see Ref. [25] for a recent discussion). We showed that a complex reflectivity at the surface (or, generically, the spin of the remnant) introduce mixing among the two polarizations, drastically modifying the shape of the echoes.

Using a Fisher analysis, we have then estimated the statistical errors on the template parameters for a post-merger GW detection with current and future GW interferometers. Our analysis suggests that ECO models with $|\mathcal{R}|^2 \approx 1$ can be detected or ruled out with aLIGO/Virgo (for events with $\rho_{\rm ringdown} \gtrsim 8$) at 5σ confidence level. These events might also allow us to probe values of the reflectivity as small as $|\mathcal{R}|^2 \approx 0.8$ at $\approx 2\sigma$ confidence level.

ECOs with $|\mathcal{R}| = 1$ are already ruled out by the ergoregion instability [3, 41] and by the absence of GW stochastic background in LIGO O1 run [45]. Excluding/detecting echoes for models with smaller values of the reflectivity (for which the ergoregion instability is absent [3, 4]) requires SNRs in the post-merger phase of $\mathcal{O}(100)$. This will be achievable only with 3G detectors (ET and Cosmic Explorer) and with the space-based mission LISA. Our preliminary analysis confirms that very stringent constraints on (or detection of) ultracompact horizonless objects can be obtained with current (and especially future) interferometers.

Several interesting extensions of this work are left for the future. A natural next step is to to adopt the template developed here in a matched-filtered search for GW echoes using LIGO/Virgo public data and for a Bayesian parameter estimation. This can be done for a generic reflectivity coefficient $\mathcal{R}$, or for specific models, such as those motivated by effective field theory arguments [81] and the model recently proposed in Refs. [9, 69] for the Boltzmann reflectivity of quantum BHs.

An important open problem is to compare the echo template (obtained within perturbation theory) with the post-merger signal of an ECO coalescence producing an echoing merger. Unfortunately, numerical simulations of these systems are currently unavailable and so are inspiral-merger-ringdown waveforms for these models. Assessing the reliability of the analytical template and the importance of nonlinearities will require a comparison between analytical and numerical waveforms, following a path similar to what done in the past for the matching of standard BH ringdown templates with numerical-relativity waveforms (see, e.g., Ref. [68]).

A more technical extension deals with the modeling of the signal beyond the low-frequency approximation. The characteristic frequency of the echo signal is always smaller than the corresponding BH ringdown frequency. We expect our template to be robust to the prescription for transition to high frequencies. Nevertheless, it might be interesting to develop a high-frequency analytical approximation of the BH reflection and transmission coefficients to be matched smoothly with a low-frequency approximation. By performing the low-frequency and high-frequency expansions beyond the leading order it might be possible to obtain a better analytical approximation of the transfer function at all frequencies.

2.A Low-frequency solution of Teukolsky equation

In this appendix we derive an analytical solution for the reflection coefficient of a BH for gravitational perturbations in the small-frequency regime through a matched asymptotic expansion. The technique is detailed in Ref. [4].

For generic spin-s perturbations, Teukolsky's equations are [56–58]

$$\begin{aligned} &\Delta^{-s}\frac{d}{dr}\left(\Delta^{s+1}\frac{d\,{}_sR_{lm}}{dr}\right)\\ +\ &\left[\frac{K^2-2is(r-M)K}{\Delta}+4is\omega r-\lambda_s\right]\,{}_sR_{lm}=0\,, \end{aligned} \tag{A.1}$$

$$\begin{aligned} &\left[\left(1-y^2\right)\,{}_sS_{lm,y}\right]_{,y}+\left[(a\omega y)^2-2a\omega sy+s\right.\\ +\ &\left.{}_sA_{lm}-\frac{(m+sy)^2}{1-y^2}\right]{}_sS_{lm}=0\,, \end{aligned} \tag{A.2}$$

where ${}_sS_{lm}(\theta)e^{im\phi}$ are spin-weighted spheroidal harmonics, $y \equiv \cos\theta$, and the separation constants λ and ${}_sA_{lm}$ are related by $\lambda_s \equiv {}_sA_{lm} + a^2\omega^2 - 2am\omega$.

In the region near the surface of the ECO, the radial wave equation (A.1) for $M\omega \ll 1$ reduces to [64]

$$\begin{aligned}&[z(z+1)]^{1-s}\,\partial_z\left\{[z(z+1)]^{s+1}\,\partial_z R_s\right\}\\&\quad+\left[Q^2+iQs(1+2z)-(l-s)(l+s+1)z(z+1)\right]R_s=0\,,\end{aligned} \tag{A.3}$$

where $z = (r-r_+)/(r_+-r_-)$ and $R_s \equiv {}_sR_{lm}$ for brevity. The general solution of Eq. (A.3) is a linear combination of hypergeometric functions

$$\begin{aligned}R_s &= (1+z)^{iQ}\big[C_1 z^{-iQ}\\&\quad {}_2F_1(-l+s,l+1+s;1-\bar{Q}+s;-z)+C_2 z^{iQ-s}\\&\quad {}_2F_1(-l+\bar{Q},l+1+\bar{Q};1+\bar{Q}-s;-z)\big]\,,\end{aligned} \tag{A.4}$$

where $\bar{Q} = 2iQ$ and the integration constants C_1 and C_2 are related to the amplitudes of outgoing and ingoing waves near the surface of the ECO, respectively. For $s=-2$, we transform the solution (A.4) in the form given by Eq. (2.5). The near-horizon behavior of the solution is given by Eq. (2.16), where the coefficients $B_{\rm out}$ and $B_{\rm in}$ are related to the integration constants C_1 and C_2, respectively.

The large-r behavior of the solution (A.4) is

$$\begin{aligned}R_s &\sim \left(\frac{r}{r_+-r_-}\right)^{l-s}\Gamma(2l+1)\left[\frac{C_1\,\Gamma(1-\bar{Q}+s)}{\Gamma(l+1-\bar{Q})\Gamma(l+1+s)}\right.\\&+\left.\frac{C_2\,\Gamma(1+\bar{Q}-s)}{\Gamma(l+1+\bar{Q})\Gamma(l+1-s)}\right]+\left(\frac{r}{r_+-r_-}\right)^{-l-1-s}\\&\quad\frac{(-1)^{l+1+s}}{2\Gamma(2l+2)}\left[\frac{C_1\,\Gamma(l+1-s)\Gamma(1-\bar{Q}+s)}{\Gamma(-l-\bar{Q})}\right.\\&+\left.\frac{C_2\,\Gamma(l+1+s)\Gamma(1+\bar{Q}-s)}{\Gamma(-l+\bar{Q})}\right].\end{aligned} \tag{A.5}$$

At infinity, the radial wave equation (A.1) for $M\omega \ll 1$ reduces to [41]

$$r\partial_r^2 f_s + 2(l+1-i\omega r)\partial_r f_s - 2i(l+1-s)\omega f_s = 0\,, \tag{A.6}$$

where $f_s = e^{i\omega r} r^{-l+s} R_s$. The general solution of Eq. (A.6) is a linear combination of a confluent hypergeometric function and a Laguerre polynomial

$$\begin{aligned} R_s &= e^{-i\omega r} r^{l-s} \big[C_3 \, U(l+1-s, 2l+2, 2i\omega r) \\ &+ C_4 \, L^{2l+1}_{-l-1+s}(2i\omega r) \big] \,, \end{aligned} \tag{A.7}$$

where the absence of ingoing waves at infinity implies $C_4 = (-1)^{l-s} \, C_3 \, \Gamma(-l+s)$. For $s = -2$, the solution (A.7) is turned in the form given by Eq. (2.5). In order to have a purely outgoing wave with unitary amplitude at infinity, as in Eq. (2.16), we impose

$$C_3 = \frac{(-i\omega)^{1+l} \, 2^l \, \Gamma(3+l)}{\lambda_{-2} \, \lambda_0 \, \Gamma(-1+l)} \,. \tag{A.8}$$

The small-r behavior of the solution (A.7) is

$$\begin{aligned} R_s &\sim C_3 \, r^{l-s} \frac{(-1)^{l-s}}{2} \frac{\Gamma(l+1+s)}{\Gamma(2l+2)} \\ &+ C_3 \, r^{-l-1-s} (2i\omega)^{-(2l+1)} \frac{\Gamma(2l+1)}{\Gamma(l+1-s)} \,. \end{aligned} \tag{A.9}$$

The matching of Eqs. (A.5) and (A.9) in the intermediate region yields

$$\frac{C_1}{C_2} = -\frac{\Gamma(l+1+s)}{\Gamma(l+1-s)} \left[\frac{R_+ + i(-1)^l (\omega(r_+ - r_-))^{2l+1} L S_+}{R_- + i(-1)^l (\omega(r_+ - r_-))^{2l+1} L S_-} \right] , \tag{A.10}$$

where

$$\begin{aligned} R_\pm &\equiv \frac{\Gamma(1 \pm \bar{Q} \mp s)}{\Gamma(l+1 \pm \bar{Q})} \,, \quad S_\pm \equiv \frac{\Gamma(1 \pm \bar{Q} \mp s)}{\Gamma(-l \pm \bar{Q})} \,, \\ L &\equiv \frac{1}{2} \left[\frac{2^l \, \Gamma(l+1+s) \Gamma(l+1-s)}{\Gamma(2l+1)\Gamma(2l+2)} \right]^2 \,. \end{aligned} \tag{A.11}$$

The reflection coefficient $\mathcal{R}_{\rm BH} = B_{\rm in}/B_{\rm out}$ is computed in terms of C_2/C_1. By using Eq. (A.10), we derive an analytical expression for $\mathcal{R}_{\rm BH}$ at low frequencies. For $l = 2$, the equation for $\mathcal{R}_{\rm BH}$ reads

$$\begin{aligned} \mathcal{R}^{\rm LF}_{\rm BH} = -8Mk e^{\frac{\zeta(\gamma-1)}{\gamma+1}} \frac{2Mk - i(\gamma-1)}{(\gamma-1)^2} \left[\frac{-M(\gamma-1)\xi}{L} \right]^{\zeta(\gamma-1)} \left[\frac{16k^2M^2}{(\gamma-1)^2} + 1 \right] \times \\ \frac{\Gamma(-2+\zeta)\Gamma(-1-\zeta) \left[1800 i \Gamma(-2-\zeta) + (\omega M(\gamma-1)\xi)^5 \, \Gamma(3-\zeta) \right]}{\Gamma(-2-\zeta)\Gamma(3-\zeta) \left[1800 i \Gamma(-2+\zeta) + (\omega M(\gamma-1)\xi)^5 \, \Gamma(3+\zeta) \right]} \,, \end{aligned} \tag{A.12}$$

where $\gamma = r_-/r_+$, $\xi = 1 + \sqrt{1-\chi^2}$, $\zeta = i(2\omega M - m\sqrt{\gamma})(\gamma+1)\xi/(\gamma-1)$, and L is an arbitrary constant (with dimensions of a length) which is related to the integration constant of Eq. (2.7). The expression of $\mathcal{R}_{\rm BH}$ is provided in a publicly available Mathematica® notebook [1].

2.B BH response at the horizon in some particular cases

In this appendix we provide some particular case for the BH response at the horizon, $Z^-_{\rm BH}$, for some specific toy models of the source. We assume the latter is localized within the cavity.

The simplest case is that of a source localized in space, and for which the frequency dependence can be factored out:

$$\tilde{S}(\omega, x) = C(\omega)\exp\left(-(x-x_s)^2/\sigma^2\right), \tag{B.1}$$

where $|x_s| \ll M$. In this case, it is easy to show that

$$\tilde{\mathcal{Z}}^+_{\rm BH} = e^{2ikx_s}\tilde{Z}^+_{\rm BH}. \tag{B.2}$$

This, together with Eq. (2.27), yields

$$\tilde{Z}^-_{\rm BH} = \left(\frac{e^{2ikx_s} + \mathcal{R}_{\rm BH}}{\mathcal{T}_{\rm BH}}\right)\tilde{Z}^+_{\rm BH}. \tag{B.3}$$

Remarkably, the above relation is independent of the width of the Gaussian source σ and of the function $C(\omega)$ characterizing the source, and it is also valid for any spin. Note that the above result is formally equivalent to the case of localized source studied in Ref. [2], and in fact reduces to it when $\sigma \to 0$ and x_s coincides with the surface location x_0.

Inspired by Eq. (B.2), one could also parametrize the BH response $\tilde{\mathcal{Z}}^+_{\rm BH}$ relative to $\tilde{Z}^+_{\rm BH}$ in a model-agnostic way with a generic (complex) proportionality factor:

$$\tilde{\mathcal{Z}}^+_{\rm BH} = \eta e^{i\nu} Z^+_{\rm BH}, \tag{B.4}$$

where η and ν are (real) parameters of the template. Since the BH response is dominated by the QNMs, a model in which $\tilde{\mathcal{Z}}^+_{\rm BH} = \mathcal{F}(\omega)Z^+_{\rm BH}$ can be effectively reduced to $\tilde{\mathcal{Z}}^+_{\rm BH} = \mathcal{F}(\omega_R)Z^+_{\rm BH}$. In such case the term $\mathcal{F}(\omega_R) = \eta e^{i\nu}$ is a generic parametrization of a complex number.

Finally, another possible model is to consider a plane-wave source that travels towards $\pm\infty$, in this case we have

$$\begin{aligned}\tilde{S}(x,\omega) &= \int dt e^{i\omega t} S(x,t) \\ &= \int dt e^{i\omega t} S(0, t\mp x) = \tilde{S}(0,\omega)e^{\pm i\omega x}.\end{aligned} \tag{B.5}$$

Using Eq. (2.15), we obtain

$$\tilde{Z}^{+}_{\rm BH}(\omega) = \tilde{Z}^{-}_{\rm BH}(\omega)\frac{\int_{-\infty}^{+\infty} dx \Psi_{-} e^{\pm i\omega x}}{\int_{-\infty}^{+\infty} dx \Psi_{+} e^{\pm i\omega x}}\,, \tag{B.6}$$

or, more explicitly

$$\tilde{Z}^{+}_{\rm BH}(\omega) = \tilde{Z}^{-}_{\rm BH}(\omega)\frac{\int_{x\sim 0} dx \Psi_{-} e^{i\omega x} + \int^{\infty}(A_{\rm out}e^{2i\omega x} + A_{\rm in})dx + \int_{-\infty} dx e^{im\Omega x}}{\int_{x\sim 0} dx \Psi_{+} e^{i\omega x} + \int^{\infty} e^{2i\omega x}dx + \int_{-\infty}(B_{\rm out}e^{2i\omega x - im\Omega x} + B_{\rm in}e^{im\Omega x})dx}\,,$$

where $x \sim 0$ is the region where the potential is non-zero and we considered only the upper-sign case for ease of notation. Considering that $\tilde{Z}^{+}_{\rm BH}(\omega)$ has a pole at $\omega_{\rm QNM} = \omega_R + i\omega_I$ we expect also $\tilde{Z}^{-}_{\rm BH}(\omega)$ to have such a pole. Since $\Im\omega_{\rm QNM} < 0$ the terms $\int^{+\infty} dx$ dominate the numerator and the denominator for $\omega \approx \omega_{\rm QNM}$, and we obtain

$$\tilde{Z}^{+}_{\rm BH} \approx -\left(\frac{\mathcal{R}_{\rm BH}}{\mathcal{T}_{\rm BH}}\right)^{*}\tilde{Z}^{-}_{\rm BH}\,. \tag{B.7}$$

The case with the lower sign (plane wave traveling toward $-\infty$) gives the same result.

Chapter 3

IMPACT OF TRANSFORMING TO CONFORMAL FERMI COORDINATES ON QUASI-SINGLE FIELD NON-GAUSSIANITY

In general relativity predictions for observable quantities can be expressed in a coordinate independent way. Nonetheless it may be inconvenient to do so. Using a particular frame may be the easiest way to connect theoretical predictions to measurable quantities. For the cosmological curvature bispectrum such frame is described by the Conformal Fermi Coordinates. In single field inflation it was shown that going to this frame cancels the squeezed limit of the density perturbation bispectrum calculated in Global Coordinates. We explore this issue in quasi single field inflation when the curvaton mass and the curvaton-inflaton mixing are small. In this case, the contribution to the bispectrum from the coordinate transformation to Conformal Fermi Coordinates is of the same order as that from the inflaton-curvaton interaction term but does not cancel it.

3.1 Introduction

In standard single field inflationary cosmology [82–86] the cosmological density perturbations are almost Gaussian [87]. Non-Gaussianities express themselves as connected parts of curvature perturbation correlation functions. The Fourier transform of the three point function of the curvature fluctuations is called[1] the bispectrum and is denoted by $B_\zeta(\mathbf{k}_1, \mathbf{k}_2, \mathbf{k}_3)$. The bispectrum in standard single field inflation was first calculated by Maldacena [87] in Global Coordinates (GC) and it is suppressed by slow roll parameters.

A phenomenologically relevant limit of the bispectrum is the squeezed limit in which one of the wave-vectors $\mathbf{q} \equiv \mathbf{k}_1$ is very small in magnitude compared to the other two, $|\mathbf{q}| \ll |\mathbf{k}_{2,3}|$. Since $\mathbf{k}_1 + \mathbf{k}_2 + \mathbf{k}_3 = 0$ we have that $\mathbf{k} \equiv \mathbf{k}_2 \simeq -\mathbf{k}_3$. The squeezed limit of the bispectrum influences the galaxy power spectrum at small wavevectors [88].

It has been shown [89–92] that in standard single field inflation transforming to Conformal Fermi Coordinates (CFC) [90, 93] with respect to the very long wave-

[1] Up to a factor of $(2\pi)^3\delta(\mathbf{k}_1 + \mathbf{k}_2 + \mathbf{k}_3)$.

length (small wave-vector) curvature perturbations cancels the squeezed limit of the bispectrum calculated in GC. This cancellation is manifest in the de Sitter era before reheating takes place. Many inflationary models have been studied that can give rise to significant non-Gaussianities, see for example [94–108]. One of the most studied and simplest of these is called Quasi Single Field Inflation (QSFI). It has an additional scalar field called the curvaton that mixes with the inflaton creating a rich dynamics that can lead to measurable curvature non-Gaussianities. We work in the limit where the mass of the curvaton and the coupling between the curvaton and the inflaton are small compared to the Hubble constant during inflation. We calculate the bispectrum in this limit in GC and then transform it to CFC. The contribution from transforming to CFC and from the interaction vertex in GC are typically of the same order but do not cancel against each other[2]. Although QSFI can have large measurable non-Gaussianities, in the limit we work (where the potential interactions of the curvaton are negligible) $f_{\rm NL}$ is only about 10^{-2}. Throughout this chapter, we use $G = c = 1$ units and $\eta_{\mu\nu} = \mathrm{diag}(-1, +1, +1, +1)$.

3.2 Scale Invariance

In this chapter we consider a de Sitter background metric

$$ds^2 = -dt^2 + e^{2Ht} dx^i dx^i \tag{3.1}$$

and we work in the limit where the Hubble constant during inflation (H) and the derivative with respect to the time t of the inflaton field ($\dot{\phi}_0$) do not depend on time. Expressing the metric in terms of the conformal time $\tau = -e^{-Ht}/H$, we have

$$ds^2 = \frac{1}{H^2 \tau^2} \left(-d\tau^2 + dx^i dx^i \right) , \tag{3.2}$$

where the beginning and the end of inflation correspond to, respectively, $\tau \to -\infty$ and $\bar{\tau} \simeq 0$. The background metric exhibits scale invariance under the transformation $\tau \to \lambda\tau$ and $x^i \to \lambda x^i$ that is preserved when $\dot{\phi}_0$ and H are constant. This symmetry implies that the power spectrum is a homogeneous function of order minus three in $1/\tau$ and $|\mathbf{p}|$. That is,

$$\left(3 + \frac{\partial}{\partial \log |\mathbf{p}|} \right) P_\zeta(\tau, |\mathbf{p}|) = \frac{\partial}{\partial \log \tau} P_\zeta(\tau, |\mathbf{p}|) \, . \tag{3.3}$$

We will neglect the time evolution of H and $\dot{\phi}_0$ that is important towards the end of inflation and depends on the shape of the inflaton potential. Hence all our results will

[2] We expect the pure gravity contribution to be smaller.

be scale invariant. Scale invariance has implications for the higher point correlations of the curvature fluctuations as well. For example, it implies that the bispectrum $B_\zeta(\tau, \mathbf{k}_1, \mathbf{k}_2, \mathbf{k}_3)$ is a homogeneous function of $\mathbf{k}_1, \mathbf{k}_2, \mathbf{k}_3$ and $1/\tau$ of degree minus six.

3.3 Quasi Single Field Inflation

In QSFI the inflaton field ϕ is accompanied by another scalar field the curvaton s. Although s does not participate in the slow roll process, it does interact and mix with the inflaton through the term [109, 110]

$$\mathcal{L}_{\text{dim } 5} = -\frac{1}{\Lambda} g^{\mu\nu} \partial_\mu \phi \partial_\nu \phi s \,. \tag{3.4}$$

We work in the gauge where the inflaton field is only a function of time $\phi_0(t)$ with no fluctuations. The Goldstone field $\pi(x)$, associated with time translational invariance breaking (by the time dependence of ϕ_0) [111][3] gives rise to the curvature fluctuations ζ which are linearly related to π via

$$\zeta = -\frac{H}{\dot{\phi}_0} \pi \,. \tag{3.5}$$

In a de Sitter background, the Lagrangian describing $\pi(x)$ and $s(x)$ is then

$$\mathcal{L} = \mathcal{L}_0 + \mathcal{L}_{\text{int}} \,, \tag{3.6}$$

where

$$\mathcal{L}_0 = \frac{1}{2(H\tau)^2} \left[(\partial_\tau \pi)^2 - \nabla \pi \cdot \nabla \pi + (\partial_\tau s)^2 - \frac{m^2}{(H\tau)^2} s^2 - \nabla s \cdot \nabla s - \frac{2\mu}{H\tau} s \partial_\tau \pi \right] \tag{3.7}$$

and

$$\mathcal{L}_{\text{int}} = \frac{1}{\Lambda (H\tau)^2} \left[(\partial_\tau \pi)^2 - \nabla \pi \cdot \nabla \pi \right] s \,. \tag{3.8}$$

Note that we have neglected any potential interaction terms for the curvaton s. In Eq. (3.7) we introduced

$$\mu = 2\dot{\phi}_0 / \Lambda \tag{3.9}$$

and we rescaled π by $\dot{\phi}_0$ (we take $\dot{\phi}_0 > 0$) to obtain a more standard normalization for the π kinetic term. We have also included the measure factor $\sqrt{-g}$ in the Lagrangian so that the action is equal to $\int d^3x d\tau \mathcal{L}$. The kinetic mixing term between π and s in

[3] In [111] it is denoted by π_c.

Eq. (3.7) is the result of the background inflaton field breaking Lorentz invariance. We now introduce the quantities

$$\alpha_{\pm} = \frac{3}{2} \pm \sqrt{\frac{9}{4} - \frac{m^2 + \mu^2}{H^2}} \tag{3.10}$$

and

$$\bar{\eta} = |\mathbf{k}| \bar{\tau} \, , \tag{3.11}$$

where $\mathbf{k}$ is the wavevector associated to the shortest wavelenght mode that we consider in the bispectrum. We will work in the limit $(m^2 + \mu^2)/H^2 \ll 1$, which implies that

$$\alpha_{-} \simeq \frac{m^2 + \mu^2}{3H^2} \ll 1 \, . \tag{3.12}$$

We also assume that $\mu^2/(\mu^2 + m^2) = \mathcal{O}(1)$ and

$$\frac{1 - (-\bar{\eta})^{\alpha_{-}}}{\alpha_{-}} \gg 1 \, . \tag{3.13}$$

This last condition is required for the terms we keep in the power spectrum and bispectrum to be enhanced over those that we neglect. Using the methods developed in [110] we compute analytically the equal time correlation functions of the curvature perturbation at the end of inflation.

To compute correlation functions involving π and s, we expand the quantum fields in terms of creation and annihilation operators. Due to the kinetic mixing term in the Lagrangian, the fields π and s share a pair of creation and annihilation operators with commutation relations,

$$[a^{(i)}(\mathbf{p}), a^{(j)\dagger}(\mathbf{p}')] = (2\pi)^3 \delta^{ij} \delta^{(3)}(\mathbf{p} - \mathbf{p}') \, . \tag{3.14}$$

Introducing $\eta = |\mathbf{p}|\tau$ we write

$$\pi(\mathbf{x}, \tau) = \int \frac{d^3p}{(2\pi)^3} \left(a^{(1)}(\mathbf{p}) \pi^{(1)}_{|\mathbf{p}|}(\eta) e^{i\mathbf{p}\cdot\mathbf{x}} + a^{(2)}(\mathbf{p}) \pi^{(2)}_{|\mathbf{p}|}(\eta) e^{i\mathbf{p}\cdot\mathbf{x}} + \text{h.c.} \right) \tag{3.15}$$

and

$$s(\mathbf{x}, \tau) = \int \frac{d^3p}{(2\pi)^3} \left(a^{(1)}(\mathbf{p}) s^{(1)}_{|\mathbf{p}|}(\eta) e^{i\mathbf{p}\cdot\mathbf{x}} + a^{(2)}(\mathbf{p}) s^{(2)}_{|\mathbf{p}|}(\eta) e^{i\mathbf{p}\cdot\mathbf{x}} + \text{h.c.} \right) \, . \tag{3.16}$$

The mode functions $\pi^{(i)}_{|\mathbf{p}|}(\eta)$ and $s^{(i)}_{|\mathbf{p}|}(\eta)$ are determined by the equations of motion for the fields π and s and by the canonical commutation relations. For the calculation of the bispectrum when α_- is small it is the behaviour of these mode functions for $-\eta$ close to zero[4] that is important [110]. After rescaling the mode functions

$$\pi^{(i)}_{|\mathbf{p}|}(\eta) = \frac{H}{|\mathbf{p}|^{3/2}}\pi^{(i)}(\eta)\,, \tag{3.17}$$

$$s^{(i)}_{|\mathbf{p}|}(\eta) = \frac{H}{|\mathbf{p}|^{3/2}}s^{(i)}(\eta) \tag{3.18}$$

we can expand $\pi^{(i)}(\eta)$ and $s^{(i)}(\eta)$ in this region as

$$\begin{aligned}\pi^{(i)}(\eta) &= a_0^{(i)} + a_-^{(i)}(-\eta)^{\alpha_-} + a_{0,2}^{(i)}(-\eta)^2 + a_{-,2}^{(i)}(-\eta)^{\alpha_-+2} + a_+^{(i)}(-\eta)^{\alpha_+} + a_3^{(i)}(-\eta)^3 + \ldots\,,\\ s^{(i)}(\eta) &= b_-^{(i)}(-\eta)^{\alpha_-} + b_{0,2}^{(i)}(-\eta)^2 + b_{-,2}^{(i)}(-\eta)^{\alpha_-+2} + b_+^{(i)}(-\eta)^{\alpha_+} + b_3^{(i)}(-\eta)^3 + \ldots\,,\end{aligned} \tag{3.19}$$

where the ellipses represent terms with higher powers of $-\eta$ that we will not need. Using the equations of motion we get

$$b_0^{(i)} = 0, \quad b_-^{(i)} = \frac{Ha_-^{(i)}\alpha_-}{\mu}, \quad b_+^{(i)} = \frac{Ha_+^{(i)}\alpha_+}{\mu}, \quad b_3^{(i)} = \frac{-3H\mu}{m^2}a_3^{(i)}\,. \tag{3.20}$$

By matching this theory to an effective field theory in the small $-\eta$ limit [110] it is possible to prove that

$$\sum_{i=1,2}|a_0^{(i)}|^2 = \sum_{i=1,2}|a_-^{(i)}|^2 = -\sum_{i=1,2}\mathrm{Re}[a_0^{(i)}a_-^{(i)*}] = \frac{9\mu^2H^2}{2(\mu^2+m^2)^2} \tag{3.21}$$

and by using the canonical commutation relations for the fields π and s we find

$$\mathrm{Im}[a_0^{(i)}b_3^{(i)*}] = \frac{\mu H}{2(\mu^2+m^2)}, \quad \mathrm{Im}[a_-^{(i)*}b_+^{(i)*}] = -\frac{\mu H}{2(\mu^2+m^2)}\,. \tag{3.22}$$

All other similar quantities are subleading in our calculations. Using the above results the leading contribution to the power spectrum of the curvature perturbations in the limit of small $-\eta$ is

$$P_\zeta(\tau,|\mathbf{p}|) = \frac{9H^6\mu^2\left[1-(-\eta)^{\alpha_-}\right]^2}{2|\mathbf{p}|^3\dot\phi_0^2\left(\mu^2+m^2\right)^2}\,. \tag{3.23}$$

This is needed to compute the impact of the change of coordinates from GC to CFC on the bispectrum (see Appendix 3.A).

[4] Recall that η is negative.

3.4 Bispectrum in Global Coordinates

In this section we work in GC and we compute the bispectrum for ζ in the squeezed limit at the end of inflation. Working to first order in the interactions and using the in-in formalism [112] we have

$$\langle\zeta(\bar{\tau},\mathbf{x}_1)\zeta(\bar{\tau},\mathbf{x}_2)\zeta(\bar{\tau},\mathbf{x}_3)\rangle = i\int_{-\infty}^{\bar{\tau}} d\tau'\langle[H_{\rm int}(\tau'),\zeta(\bar{\tau},\mathbf{x}_1)\zeta(\bar{\tau},\mathbf{x}_2)\zeta(\bar{\tau},\mathbf{x}_3)]\rangle\,, \tag{3.24}$$

where $H_{\rm int}$ denotes the interaction Hamiltonian in the interaction picture. In the squeezed limit we can drop the terms proportional to the spatial derivatives of π from $\mathcal{L}_{\rm int}$ and the interaction Hamiltonian simplifies to

$$H_{\rm int}(\tau) = \int d^3x \frac{1}{(H\tau)^2\Lambda}(\partial_\tau\pi)^2 s\,. \tag{3.25}$$

Notice that $H_{\rm int} = \mathcal{L}_{\rm int}$ since we have a derivative interaction. Fourier transforming we find that the leading order contribution in α_- in the region of phase space that we are considering to the bispectrum in the squeezed limit is

$$B_\zeta^{\rm (GC)}(\mathbf{q},\mathbf{k},-\mathbf{k}) \simeq -4\left(\frac{H^7\mu}{\dot{\phi}_0^4}\right)\frac{1}{|\mathbf{k}|^3|\mathbf{q}|^3}\left(I_a+I_b+I_c\right)\,, \tag{3.26}$$

where

$$I_a = \int_{-1}^{\bar{\eta}}\frac{d\eta'}{(-\eta')^2}{\rm Re}\left[\pi^{(i)}(r\bar{\eta})\,\dot{\pi}^{(i)}(r\eta')^*\right]{\rm Re}\left[\pi^{(j)}(\bar{\eta})\dot{\pi}^{(j)}(\eta')^*\right]{\rm Im}\left[\pi^{(n)}(\bar{\eta})s^{(n)}(\eta')^*\right], \tag{3.27}$$

$$I_b = \int_{-1}^{\bar{\eta}}\frac{d\eta'}{(-\eta')^2}{\rm Re}\left[\pi^{(i)}(r\bar{\eta})\,\dot{\pi}^{(i)}(r\eta')^*\right]{\rm Im}\left[\pi^{(j)}(\bar{\eta})\dot{\pi}^{(j)}(\eta')^*\right]{\rm Re}\left[\pi^{(n)}(\bar{\eta})s^{(n)}(\eta')^*\right], \tag{3.28}$$

and

$$I_c = \int_{-1}^{\bar{\eta}}\frac{d\eta'}{(-\eta')^2}{\rm Re}\left[\pi^{(i)}(\bar{\eta})\,\dot{\pi}^{(i)}(\eta')^*\right]{\rm Im}\left[\pi^{(j)}(\bar{\eta})\dot{\pi}^{(j)}(\eta')^*\right]{\rm Re}\left[\pi^{(n)}(r\bar{\eta})\,s^{(n)}(r\eta')^*\right]\,. \tag{3.29}$$

In the above equations a dot indicates a derivative with respect to η', the repeated mode function indices i, j, n are summed over 1 and 2 and we introduced the parameter $r \equiv |\mathbf{q}|/|\mathbf{k}|$. Most of the contribution to the integrals comes from the region $-\eta' \ll 1$ and to leading order in $(\mu^2+m^2)/H^2$ we set the lower bound of the integrals to be -1. Using the results of Section 3.3 we find that

$${\rm Re}\left[\pi^{(i)}(r\bar{\eta})\,\dot{\pi}^{(i)}(r\eta')^*\right] \simeq \frac{1}{2}\left(\frac{3\mu^2}{\mu^2+m^2}\right)(-\eta')^{\alpha_--1}r^{\alpha_-}\left[1-(-r\bar{\eta})^{\alpha_-}\right]\,, \tag{3.30}$$

$$\mathrm{Re}\left[\pi^{(i)}(\bar{\eta})\,\dot{\pi}^{(i)}(\eta')^*\right] \simeq \frac{1}{2}\left(\frac{3\mu^2}{\mu^2+m^2}\right)(-\eta')^{\alpha_- -1}\left[1-(-\bar{\eta})^{\alpha_-}\right], \tag{3.31}$$

$$\mathrm{Im}\left[\pi^{(i)}(\bar{\eta})\,s^{(i)}(\eta')^*\right] \simeq \frac{1}{2}\left(\frac{H\mu}{\mu^2+m^2}\right)\left[(-\eta')^3-(-\eta')^{3-\alpha_-}(-\bar{\eta})^{\alpha_-}\right], \tag{3.32}$$

$$\mathrm{Re}\left[\pi^{(i)}(r\bar{\eta})\,s^{(i)}(r\eta')^*\right] \simeq \frac{3H\mu\left[(-r\bar{\eta})^{\alpha_-}-1\right](-r\eta')^{\alpha_-}}{2\left(\mu^2+m^2\right)}, \tag{3.33}$$

$$\mathrm{Re}\left[\pi^{(i)}(\bar{\eta})\,s^{(i)}(\eta')^*\right] \simeq \frac{3H\mu\left[(-\bar{\eta})^{\alpha_-}-1\right](-\eta')^{\alpha_-}}{2\left(\mu^2+m^2\right)}, \tag{3.34}$$

$$\mathrm{Im}\left[\pi^{(i)}(\bar{\eta})\,\dot{\pi}^{(i)}(\eta')^*\right] \simeq \frac{\eta'^2\left[\mu^2\left(\frac{\eta'}{\bar{\eta}}\right)^{-\alpha_-}+m^2\right]}{2\left(\mu^2+m^2\right)}, \tag{3.35}$$

and that $\mathrm{Im}\left[\pi^{(i)}(r\bar{\eta})\,s^{(i)}(r\eta')^*\right]$ and $\mathrm{Im}\left[\pi^{(i)}(r\bar{\eta})\,\dot{\pi}^{(i)}(r\eta')^*\right]$ are suppressed in the squeezed limit. Performing the η' integration we have that to leading order in small quantities

$$I_a = \frac{27H^3\mu^5\left[(-\bar{\eta})^{\alpha_-}-1\right]^3 r^{\alpha_-}\left[(-r\bar{\eta})^{\alpha_-}-1\right]}{16\left(\mu^2+m^2\right)^4} \tag{3.36}$$

and

$$I_b = I_c = \frac{27H^3\mu^3\left[(-\bar{\eta})^{\alpha_-}-1\right]^2 r^{\alpha_-}\left[(-r\bar{\eta})^{\alpha_-}-1\right]\left[(-\bar{\eta})^{\alpha_-}\left(2\mu^2+m^2\right)+m^2\right]}{16\left(\mu^2+m^2\right)^4}. \tag{3.37}$$

This completes the calculation of the bispectrum in GC and we now turn to transform it to CFC.

3.5 The Bispectrum in CFC

We are now ready to compute the bispectrum in CFC by using Eq. (A.21) to transform the result that we found in Section 3.4 for the bispectrum in GC. We have

$$B_\zeta(\mathbf{q},\mathbf{k},-\mathbf{k}) = B_\zeta^{(\mathrm{GC})}(\mathbf{q},\mathbf{k},-\mathbf{k}) + \Delta B_\zeta(\mathbf{q},\mathbf{k},-\mathbf{k}), \tag{3.38}$$

where

$$\Delta B_\zeta(\mathbf{q},\mathbf{k},-\mathbf{k}) = P_\zeta(\bar{\tau},|\mathbf{q}|)\frac{\partial}{\partial \log\bar{\tau}}P_\zeta(\bar{\tau},|\mathbf{k}|) \tag{3.39}$$

and to simplify the notation we dropped the superscript CFC. Using Eq (3.23) we get

$$\Delta B_\zeta(\mathbf{q},\mathbf{k},-\mathbf{k}) \simeq \frac{27H^{10}\mu^4\left[(-\bar{\eta})^{\alpha_-}-1\right](-\bar{\eta})^{\alpha_-}\left[(-r\bar{\eta})^{\alpha_-}-1\right]^2}{2|\mathbf{k}|^3|\mathbf{q}|^3\dot{\phi}_0^4\left(\mu^2+m^2\right)^3}. \tag{3.40}$$

Even though for modes of cosmological interest $-\bar{\eta} = -|\mathbf{k}|\bar{\tau} \simeq e^{-60}$ [113], $(-\bar{\eta})^{\alpha_-}$ can still be of order unity, for example if $\alpha_- \sim 1/50$. In this case, the contribution to the bispectrum from the change of coordinates from GC to CFC, is comparable to the one that comes from the three point vertex in GC.

In the limit $m \ll \mu$, we finally obtain

$$B_\zeta^{(\mathrm{GC})}(\mathbf{q}, \mathbf{k}, -\mathbf{k}) = -\frac{1}{|\mathbf{k}|^3|\mathbf{q}|^3} \frac{27H^{10}\left[(-\bar{\eta})^{\alpha_-} - 1\right]^2 \left[5(-\bar{\eta})^{\alpha_-} - 1\right] r^{\alpha_-} \left[(-r\bar{\eta})^{\alpha_-} - 1\right]}{4\mu^2\dot{\phi}_0^4} \tag{3.41}$$

and

$$\Delta B_\zeta(\mathbf{q}, \mathbf{k}, -\mathbf{k}) \simeq \frac{27H^{10}\left[(-\bar{\eta})^{\alpha_-} - 1\right](-\bar{\eta})^{\alpha_-}\left[(-r\bar{\eta})^{\alpha_-} - 1\right]^2}{2|\mathbf{k}|^3|\mathbf{q}|^3\dot{\phi}_0^4\mu^2} \tag{3.42}$$

that are plotted in Fig. 3.1. Notice that the leading contribution to the bispectrum in GC vanishes for $(-\bar{\eta})^{\alpha_-} = 0.2$. At this point the part from the change of coordinates dominates the bispectrum.

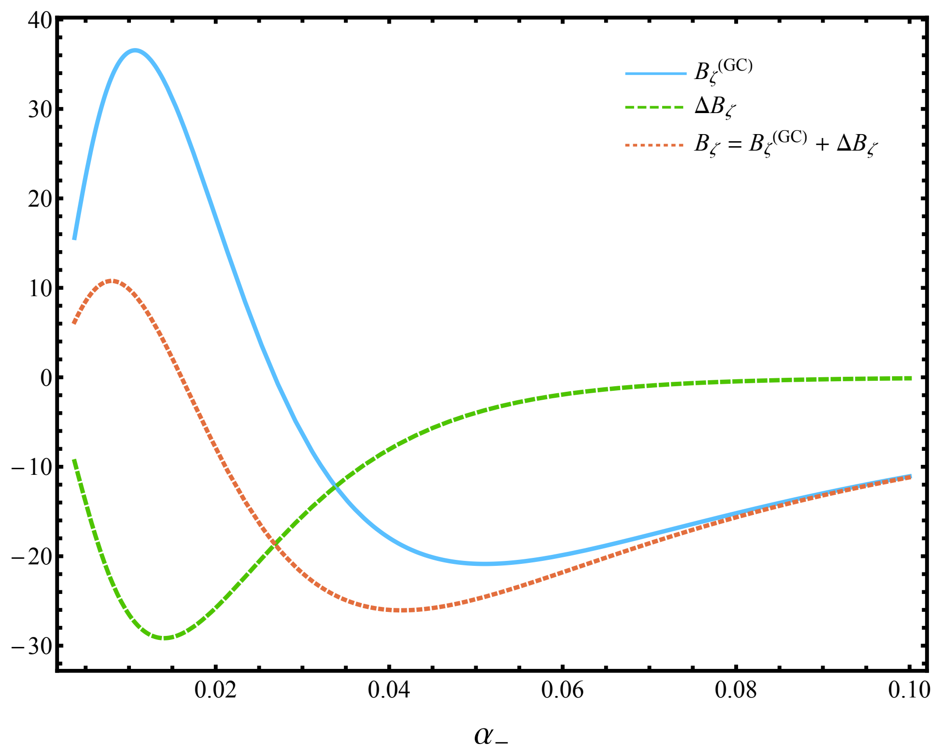

Figure 3.1: Contributions to the Bispectrum for $m \ll \mu$, $-\bar{\eta} = e^{-60}$ and $r = 10^{-3}$. We consider values of α_- that go from 0.0037 (corresponding to $(-\bar{\eta})^{\alpha_-} = 0.8$) to $\alpha_- = 0.1$. The y-axis is in units of $H^8/(|\mathbf{k}|^3|\mathbf{q}|^3\dot{\phi}_0^4)$.

In Fig. 3.2 we plot the local bispectrum f_{NL} in GC and CFC as a function of α_-

where

$$f_{\rm NL}^{\rm (GC)} = \frac{5}{12}\frac{B_\zeta^{\rm (GC)}(\mathbf{q},\mathbf{k},-\mathbf{k})}{P_\zeta(\bar\tau,|\mathbf{k}|)P_\zeta(\bar\tau,|\mathbf{q}|)}\,, \tag{3.43}$$

$$\Delta f_{\rm NL} = \frac{5}{12}\frac{\Delta B_\zeta(\mathbf{q},\mathbf{k},-\mathbf{k})}{P_\zeta(\bar\tau,|\mathbf{k}|)P_\zeta(\bar\tau,|\mathbf{q}|)} \tag{3.44}$$

and in the limit $m \ll \mu$ we have

$$f_{\rm NL}^{\rm (GC)} = -\frac{5\alpha_- r^{\alpha_-}\,[5(-\bar\eta)^{\alpha_-}-1]}{12\,[(-r\bar\eta)^{\alpha_-}-1]}\,, \tag{3.45}$$

$$\Delta f_{\rm NL} = \frac{5\alpha_-(-\bar\eta)^{\alpha_-}}{6\,[(-\eta)^{\alpha_-}-1]}\,. \tag{3.46}$$

Both $B|\mathbf{k}|^3|\mathbf{q}|^3$ and $f_{\rm NL}$ depend very weekly on the value of r. This is because r

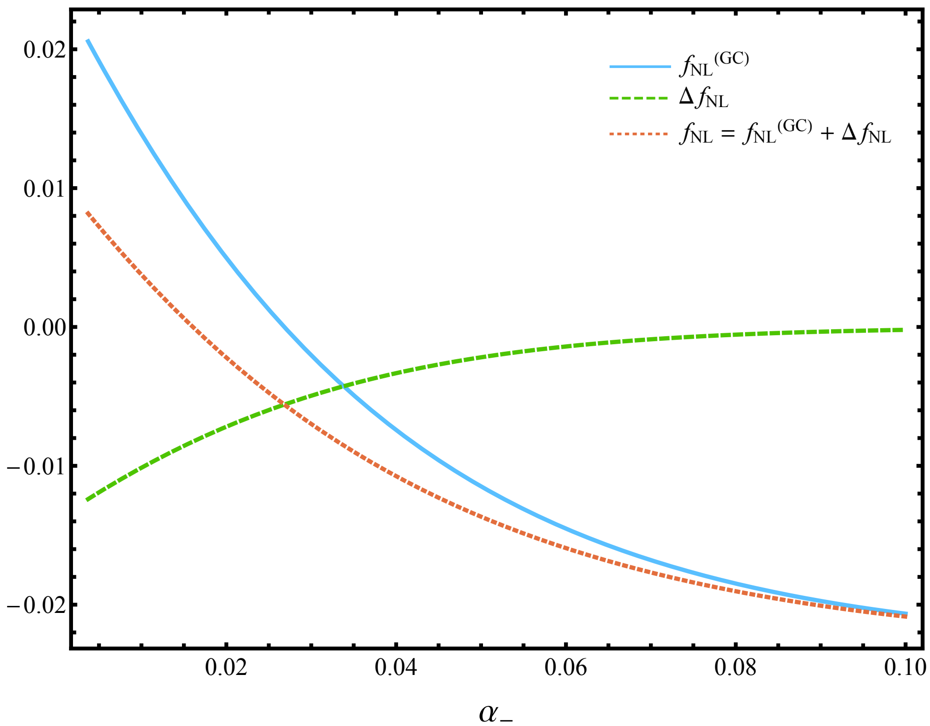

Figure 3.2: Contributions to $f_{\rm NL}$ for $m \ll \mu$, $-\bar\eta = e^{-60}$ and $r = 10^{-3}$. We consider values of α_- that go from 0.0037 (corresponding to $(-\bar\eta)^{\alpha_-} = 0.8$) to $\alpha_- = 0.1$.

only enters in these quantities raised to the power α_-.

3.6 Power Spectrum Constraint

We can constrain the parameter α_- by comparing the spectral index implied by Eq. (3.23) with the measured tilt [5] ($n_s = 0.9649 \pm 0.0042$). For $\bar\eta = -e^{-50}$ we find $\alpha_- < 0.0212$ and for $\bar\eta = -e^{-60}$ we find $\alpha_- \leq 0.0123$. In the third row of Fig. 3.3 we plot the tilt n_s in QSFI as a function of α_-.

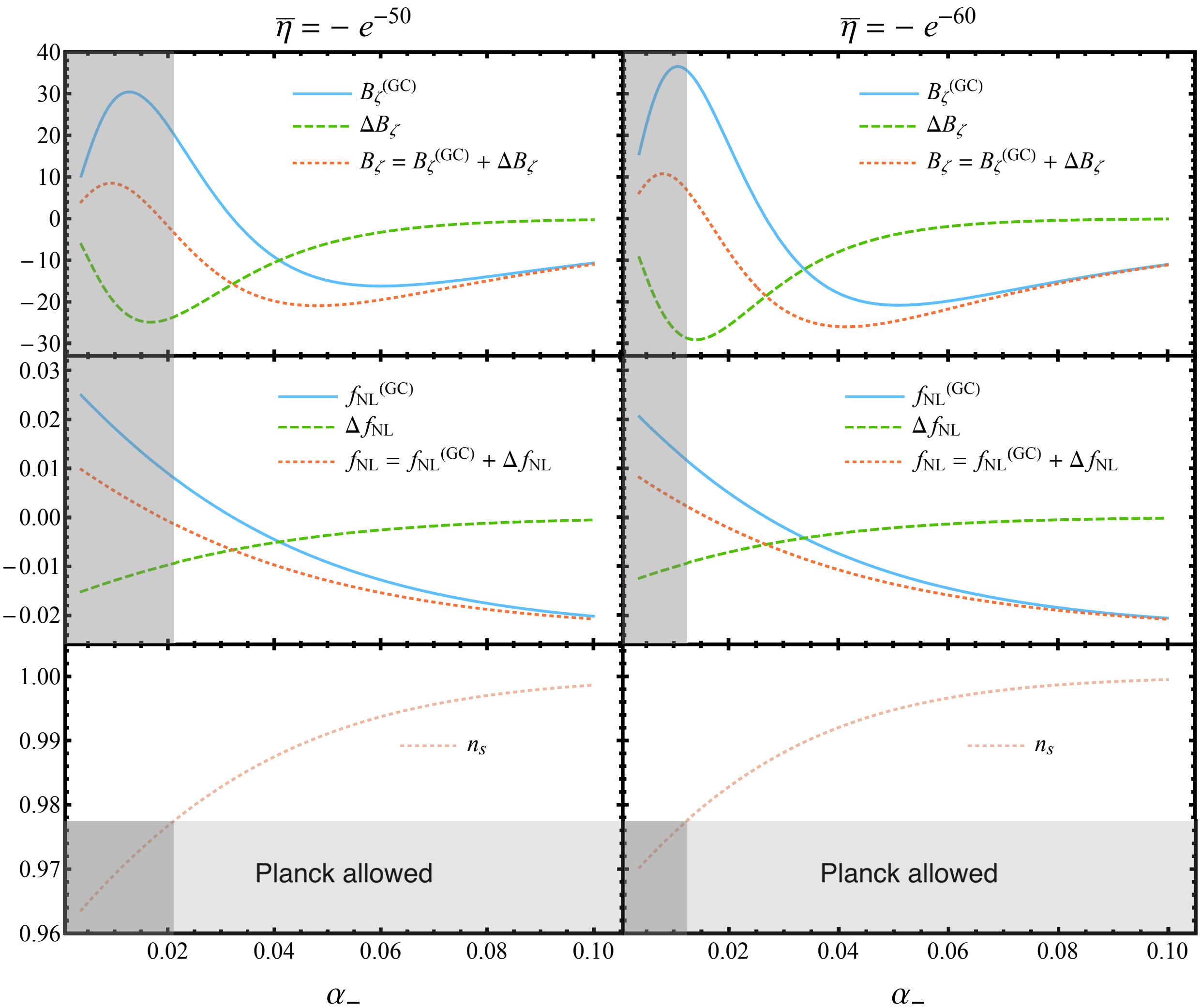

Figure 3.3: In the above panels we have $m \ll \mu$ and $r = 10^{-3}$. On the x-axes we consider values of α_- that go from 0.0037 to $\alpha_- = 0.1$. The first and second columns correspond to $\bar{\eta} = -e^{-50}$ and $\bar{\eta} = -e^{-60}$ respectively. In the first row we plot the contributions to the Bispectrum (the y-axis is in units of $H^8/(|\mathbf{k}|^3|\mathbf{q}|^3\dot{\phi}_0^4)$). In the second row we plot the contributions to $f_{\rm NL}$. In the the third row we plot the tilt n_s. The shaded regions in darker gray are the ones compatible with the measured tilt [5].

3.7 Concluding Remarks

In this chapter we considered QSFI where a dimension five operator couples the inflaton and the curvaton field. Working in the limit of small coupling and small curvaton mass we computed analytically the bispectrum in the squeezed limit in GC and in CFC. We found that transforming to CFC introduces a non-negligible correction to the result in GC. We also showed that $f_{\rm NL}$ can be either enhanced or suppressed by this effect, and in the region of parameter space that we considered

$f_{\rm NL} \simeq 10^{-2}$. In this model $f_{\rm NL}$ is small and hence these non-Gaussianities could not be observed in the near future. However, this is an interesting example where the change of coordinates from GC to CFC can have an order one effect on the bispectrum.

3.A Transformation of the Bispectrum to Conformal Fermi Coordinates

In this Appendix we rederive the coordinate transformation from GC to CFC and compute the bispectrum in CFC. Rather than taking the constructive approach of the previous literature we derive necessary and sufficient conditions that the coordinate transformation must satisfy.

The metric in GC is given by

$$g_{\mu\nu}(x) = a^2(\tau)\left[\eta_{\mu\nu} + h_{\mu\nu}(x)\right] \tag{A.1}$$

and the metric scalar perturbations in $h_{\mu\nu}$ are expressed in terms of the curvature perturbation ζ as follows:

$$h_{00} = -2\frac{\partial_\tau \zeta}{\mathcal{H}}, \tag{A.2}$$

$$h_{0i} = -\partial_i \frac{\zeta}{\mathcal{H}}, \tag{A.3}$$

$$h_{ij} = 2\zeta\delta_{ij}, \tag{A.4}$$

where $\mathcal{H} \equiv \frac{1}{a}\frac{da}{d\tau}$. We split the metric perturbation as

$$h_{\mu\nu}(x) = h^L_{\mu\nu}(x) + h^S_{\mu\nu}(x) \tag{A.5}$$

where $h^L_{\mu\nu}(k) \approx 0$ for $k \gtrsim \Lambda$ and $h^S_{\mu\nu}(k) \approx 0$ for $k \lesssim \Lambda$. Here Λ is a cutoff that divides the modes into short and long. In CFC with respect to the longest wavelength modes the metric has the form

$$g^F_{\mu\nu}(x_F) = a^2(\tau_F)\left[\eta_{\mu\nu} + h^S_{\mu\nu}(x_F) + \mathcal{O}(x^i_F x^j_F)\right] \tag{A.6}$$

where the terms $\mathcal{O}(x^i_F x^j_F)$ are made negligible by an appropriate choice of CFC. However this choice does not explicitly enter our analysis.

The coordinate transformation that takes us between these two frames can be expanded in x^i_F as [90–93]

$$x^\mu(x_F) = x^\mu_F + \xi^\mu(\tau_F) + A^\mu_{\ i}(\tau_F)x^i_F + B^\mu_{\ ij}(\tau_F)x^i_F x^j_F + \mathcal{O}(x^i_F x^j_F x^k_F) \tag{A.7}$$

where $\xi^\mu, A^\mu_{\ i}, B^\mu_{\ ij} = \mathcal{O}(h^L_{\mu\nu})$ and we neglect quantities $\mathcal{O}\left[(h^L_{\mu\nu})^2\right]$. Without loss of generality, we assume $B^\mu_{\ ij}(\tau_F) = B^\mu_{\ ji}(\tau_F)$. The transformation law for the metric tensor

$$g^F_{\mu\nu}(x_F) = \frac{\partial x^\alpha}{\partial x^\mu_F}\frac{\partial x^\beta}{\partial x^\nu_F} g_{\alpha\beta}(x) \tag{A.8}$$

gives ten differential equations for ξ^μ, $A^\mu_{\ i}$ and $B^\mu_{\ ij}$ that need to be satisfied in terms of $h^L_{\mu\nu}$ in order for $g^F_{\mu\nu}(x_F)$ to have the form of Eq. (A.6). Requiring each differential equation to hold order by order in x^i_F gives

$$(\partial_{\tau_F} + \mathcal{H})\xi^0(\tau_F) = -\frac{\partial_{\tau_F}\zeta_L(\mathbf{x}_F = \mathbf{0}, \tau_F)}{\mathcal{H}(\tau_F)} \tag{A.9}$$

$$(\partial_{\tau_F} + \mathcal{H})A^0_{\ i}(\tau_F) = -\frac{\partial_{\tau_F}\partial_i\zeta_L(\mathbf{x}_F = \mathbf{0}, \tau_F)}{\mathcal{H}(\tau_F)} \tag{A.10}$$

$$A^0_{\ i}(\tau_F) - \partial_{\tau_F}\xi_i(\tau_F) = -\partial_i\frac{\zeta_L(\mathbf{x}_F = \mathbf{0}, \tau_F)}{\mathcal{H}(\tau_F)} \tag{A.11}$$

$$2B^0_{\ ik}(\tau_F) - \partial_{\tau_F}A_{ik}(\tau_F) = -\frac{\partial_k\partial_i\zeta_L(\mathbf{x}_F = \mathbf{0}, \tau_F)}{\mathcal{H}(\tau_F)} \tag{A.12}$$

$$A_{ij}(\tau_F) + A_{ji}(\tau_F) + 2\mathcal{H}\xi^0(\tau_F)\delta_{ij} = -2\zeta_L(\mathbf{x}_F = \mathbf{0}, \tau_F)\delta_{ij} \tag{A.13}$$

$$B_{ijk}(\tau_F) + B_{jik}(\tau_F) + \frac{1}{2}\mathcal{H}A^0_{\ k}(\tau_F)\delta_{ij} = -\partial_k\zeta_L(\mathbf{x}_F = \mathbf{0}, \tau_F)\delta_{ij} \tag{A.14}$$

where the spatial indices were lowered using δ_{ij} and the quantities on the right hand side are the expressions in *comoving* coordinates. These are necessary *and* sufficient conditions for Eq. (A.6) to hold. With the coordinate transformation at hand we find how the connected three point function of ζ transforms in going from GC to CFC in the squeezed limit. Following [92], we have

$$\langle\tilde{\zeta}^F(\tau_F, \mathbf{k}_1)\tilde{\zeta}^F(\tau_F, \mathbf{k}_2)\tilde{\zeta}^F(\tau_F, \mathbf{k}_3)\rangle = \int d^3x^F_1 d^3x^F_2 d^3x^F_3\, e^{-i(\mathbf{k}_1\mathbf{x}^F_1 + \mathbf{k}_2\mathbf{x}^F_2 + \mathbf{k}_3\mathbf{x}^F_3)}\langle\zeta^F(x^F_1)\zeta^F(x^F_2)\zeta^F(x^F_3)\rangle$$

where $x^F_i \equiv (\tau_F, \mathbf{x}^F_i)$, $|\mathbf{k}_1| \ll |\mathbf{k}_2|, |\mathbf{k}_3|$.

Using spatial translational invariance we get

$$\langle\tilde{\zeta}^F(\tau_F, \mathbf{k}_1)\tilde{\zeta}^F(\tau_F, \mathbf{k}_2)\tilde{\zeta}^F(\tau_F, \mathbf{k}_3)\rangle = (2\pi)^3\delta(\mathbf{k}_1 + \mathbf{k}_2 + \mathbf{k}_3)B^{(\mathrm{CFC})}_\zeta(\mathbf{k}_1, \mathbf{k}_2, \mathbf{k}_3) \tag{A.15}$$

with

$$\begin{aligned} B^{(\mathrm{CFC})}_\zeta(\mathbf{k}_1, \mathbf{k}_2, \mathbf{k}_3) &= \int d^3y^F d^3z^F e^{-i\left[\mathbf{k}_1\mathbf{y}^F + \left(\mathbf{k}_3 + \frac{\mathbf{k}_1}{2}\right)\mathbf{z}^F\right]}\left\langle\zeta^F\left(\tau_F, \mathbf{y}^F\right)\zeta^F\left(\tau_F, -\frac{\mathbf{z}^F}{2}\right)\zeta^F\left(\tau_F, \frac{\mathbf{z}^F}{2}\right)\right\rangle \\ &= \int d^3y^F d^3z^F e^{-i\left[\mathbf{k}_1\mathbf{y}^F + (\mathbf{k}_3 + \frac{\mathbf{k}_1}{2})\mathbf{z}^F\right]}\langle 0_L|\zeta_L(\tau_F, \mathbf{y}^F)\langle 0_S|\zeta_S(x_a)\zeta_S(x_b)|0_S\rangle|0_L\rangle \end{aligned} \tag{A.16}$$

where $x_{a,b} = x_{a,b}(x^F_{a,b})$ and $x^F_a = (\tau_F, -\mathbf{z}^F/2)$, $x^F_b = (\tau_F, \mathbf{z}^F/2)$ and we assumed that ζ transforms as a scalar[5]. Moving forward we drop the designation $|0_S\rangle$ and write $\langle 0_S|\zeta_S(x_a)\zeta_S(x_b)|0_S\rangle \equiv \langle\zeta_S(x_a)\zeta_S(x_b)\rangle$ in terms of x^F_a and x^F_b up to linear order in ζ_L. Eq. (A.16) implies that the contribution to the three point function is dominated by $|\mathbf{z}^F| \ll 1/|\mathbf{k}_3|$. Thus, using Eq. (A.7) and working to linear order in the long mode, we find

$$\langle 0_S|\zeta^F_S(x^F_a)\zeta^F_S(x^F_b)|0_S\rangle = \langle 0_S|\zeta_S(x^F_a)\zeta_S(x^F_b)|0_S\rangle + \Big[\xi^0(\tau_F)\partial_{\tau_F} + A^k_i(\tau_F)(x^{F^i}_a - x^{F^i}_b)\partial^{(a)}_k + \\ +\xi^i(\tau_F)(\partial^{(a)}_i + \partial^{(b)}_i) + \frac{1}{2}A^0_i(\tau_F)(x^{F^i}_a + x^{F^i}_b)\partial_{\tau_F}\Big]\langle 0_S|\zeta_S(\tau_F, \mathbf{x}^F_a)\zeta_S(\tau_F, \mathbf{x}^F_b)|0_S\rangle \quad \text{(A.17)}$$

where the terms on the second line vanish because of translational invariance and because $\mathbf{x}^F_a = -\mathbf{x}^F_b$. Using Eq. (A.13) we obtain

$$\langle 0_S|\zeta^F_S(x^F_a)\zeta^F_S(x^F_b)|0_S\rangle = \langle 0_S|\zeta_S(x^F_a)\zeta_S(x^F_b)|0_S\rangle + \quad \text{(A.18)} \\ + \left\{\xi^0(\tau_F)\partial_{\tau_F} - \left[\mathcal{H}\xi^0(\tau_F) + \zeta_L(\mathbf{0}, \tau_F)\right]\mathbf{z}^F \frac{\partial}{\partial \mathbf{z}^F}\right\}\langle 0_S|\zeta_S(\tau_F, \mathbf{z}^F)\zeta_S(\tau_F, \mathbf{0})|0_S\rangle\,.$$

Inserting this expression back in Eq. (A.16) and using rotational invariance we get

$$B^{(\mathrm{CFC})}_\zeta(\mathbf{k}_1, \mathbf{k}_2, \mathbf{k}_3) = B^{(\mathrm{GC})}_\zeta(\mathbf{k}_1, \mathbf{k}_2, \mathbf{k}_3) - P_\zeta(\tau_F, |\mathbf{k}_1|)\left(-3 - \frac{\partial}{\partial \log|\mathbf{k}_3|}\right)P_\zeta(\tau_F, |\mathbf{k}_3|) \\ +\langle\tilde{\zeta}^F_L(\tau_F, \mathbf{k}_1)\xi^0(\tau_F)\rangle\left[\partial_{\tau_F} - \mathcal{H}\left(-3 - \frac{\partial}{\partial \log|\mathbf{k}_3|}\right)\right]P_\zeta(\tau_F, |\mathbf{k}_3|) \quad \text{(A.19)}$$

where

$$\langle\tilde{\zeta}(\tau_F, \mathbf{k}_1)\tilde{\zeta}(\tau_F, \mathbf{k}_2)\tilde{\zeta}(\tau_F, \mathbf{k}_3)\rangle = (2\pi)^3\delta(\mathbf{k}_1 + \mathbf{k}_2 + \mathbf{k}_3)B^{(\mathrm{GC})}_\zeta(\mathbf{k}_1, \mathbf{k}_2, \mathbf{k}_3) \quad \text{(A.20)}$$

and we used that $|\mathbf{k}_1| \ll |\mathbf{k}_3|$. In the limit in which scale invariance is preserved Eq. (3.3) and the fact that $\mathcal{H}\tau_F = -1$ imply that the final result does not depend on the integration constants of Eqs. (A.9)-(A.14). We finally obtain

$$B^{(\mathrm{CFC})}_\zeta(\mathbf{k}_1, \mathbf{k}_2, \mathbf{k}_3) = B^{(\mathrm{GC})}_\zeta(\mathbf{k}_1, \mathbf{k}_2, \mathbf{k}_3) + P_\zeta(\tau_F, |\mathbf{k}_1|)\frac{\partial}{\partial \log \tau_F}P_\zeta(\tau_F, |\mathbf{k}_3|)\,. \quad \text{(A.21)}$$

This expression coincides with the one in [92] for scale invariant models of inflation.

[5]We did not change the argument of ζ_L since it would have resulted in a disconnected piece that we discard.

Chapter 4

REGULARIZATION SCHEME DEPENDENCE OF THE COUNTERTERMS IN THE GALAXY BIAS EXPANSION

In this chapter we explore how different regularization prescriptions affect the counterterms in the renormalization of the galaxy bias expansion. We work in the context of primordial local non-Gaussianity including non-linear gravitational evolution. We carry out the one-loop renormalization of the field δ_ρ^2 (i.e. the square of the matter overdensity field) up to third order in gravitational evolution. Three regularization schemes are considered and their impact on the values of the counterterms is studied. We explicitly verify that the coefficients of the non-boost invariant operators are regularization scheme independent.

4.1 Introduction

The galaxy bias expansion (for a review see [114]) relates the galaxy overdensity field δ_g (i.e. the relative fluctuations in the number density of galaxies) to the mass overdensity field δ_ρ. In this chapter we don't distinguish between dark matter halos and galaxies. The composite fields in this expansion can be regulated by a short distance cutoff $(1/\Lambda)$. Renormalization renders the galaxy overdensity correlators cutoff independent. This has been studied both for Gaussian primordial curvature fluctuations [115–117] and for non-Gaussian primordial curvature fluctuations [118, 119].

In Section 4.2, we review the theoretical framework of local non-Gaussianity for primordial curvature fluctuations. The non-linear gravitational evolution of the matter overdensity field is discussed. We finally introduce three regularization schemes for the composite operator[1] δ_ρ^2 occurring in the galaxy bias expansion.

In Section 4.3, we re-examine the renormalization procedure for the composite operator δ_ρ^2 in the presence of primordial local non-Gaussianities up to third order in gravitational evolution. We explore the impact of three regularization prescriptions on renormalization. The first reproduces the coefficients and operators found in the literature [119]. The other two prescriptions close under renormalization using the same operators as the first one. However, in the presence of non-linear gravitational

[1] In this work we use the terms field and operator interchangeably.

evolution, the coefficients of the boost-invariant operators for the three prescriptions differ by quantities which can be written as surface terms in the UV diverging integrals.

In Appendix 4A, after introducing a diagrammatic notation, we prove the conformal invariance of the tree-level correlators of curvature fluctuations in the context of local primordial non-Gaussianity. In Appendix 4B, we introduce a diagrammatic notation to compute and estimate the correlators of the galaxy overdensity field and comment on an alternative way of regularizing IR divergences.

4.2 Theoretical Framework

Primordial Curvature Fluctuations and Local non-Gaussianity

Local non-Gaussianity is the hypothesis that the primordial curvature fluctuations δ_ζ are local functions of a Gaussian field ϕ_G of the form

$$\delta_\zeta(\mathbf{x}) = \sum_{n=1}^{\infty} f_n : \phi_G^n(\mathbf{x}) : \ . \tag{4.1}$$

In the above equation, operators surrounded by colons are normal ordered (i.e. any contraction between themselves in correlators vanishes), ϕ_G is a Gaussian field with zero expectation value and the f_n's are constants. In this chapter we set $f_1 = 1$. Demanding the correlators of ϕ_G to be invariant under translations, rotations, and scale transformations fixes the two-point function of ϕ_G to be

$$\langle \tilde{\phi}_G(\mathbf{k}_1)\tilde{\phi}_G(\mathbf{k}_2)\rangle = (2\pi)^3\delta(\mathbf{k}_1 + \mathbf{k}_2)\, P_\phi(k_1)\,, \tag{4.2}$$

where a tilde denotes a wavevector space quantity, $P_\phi(q) = A/q^{3-2\Delta}$ is the tree-level power spectrum of primordial curvature fluctuations (A is a constant), Δ is the scale dimension of the field ϕ_G, and $k_i = |\mathbf{k}_i|$. In this chapter we will set $\Delta = 0$.

Measurements of the Cosmic Microwave Background (CMB) anisotropy place bounds [120] on the local non-Gaussianity parameters, in particular (with the convention $f_1 = 1$) $A \sim 10^{-8}$, $f_2 = 3/5 f_{NL}^{\rm local} = 3/5(0.8 \pm 5)$, $f_3 = (9/25)g_{NL}^{\rm local}$ and $g_{NL}^{\rm local} = (-9.0 \pm 7.7) \times 10^4$. It can be seen, by rescaling $\phi_G \to \sqrt{A}\phi_G$ and factoring out a common $\sqrt{A}$, that a highly non-Gaussian theory would have $f_n \sim \mathcal{O}\left[A^{(-n+1)/2}\right]$. Hence, the above CMB bounds already indicate that our universe has nearly-Gaussian primordial curvature fluctuations.

In Appendix 4.A, after introducing a diagrammatic notation for the computation of the δ_ζ N-point functions, we prove by induction the conformal invariance of these correlators at tree-level.

Matter Density Perturbations

Even when the primordial curvature fluctuations are Gaussian, non-Gaussianities in the matter overdensity field arise at late times due to the non-linear gravitational evolution.

For simplicity, we shall assume that the all the matter in the universe is in the form of cold dark matter and behaves as a pressureless irrotational fluid. Labelling each fluid element trajectory by its initial position $\mathbf{x}_0$ (i.e. its Lagrangian coordinate), its Eulerian coordinate at conformal time τ is

$$\mathbf{x}(\mathbf{x}_0, \tau) = \mathbf{x}_0 + \mathbf{s}(\mathbf{x}_0, \tau) \tag{4.3}$$

where

$$\mathbf{s}(\mathbf{x}_0, \tau) = \int_0^\tau d\tau' \, \mathbf{v}(\mathbf{x}(\mathbf{x}_0, \tau'), \tau') \tag{4.4}$$

is called the displacement vector and $\mathbf{v}$ is the fluid element velocity.

Using standard gravitational perturbation theory [121–123] in the Newtonian approximation, the solutions to the Euler and Poisson equations in an expanding universe for the overdensity matter field $\delta_\rho(\mathbf{x}, \tau)$ can be written as

$$\delta_\rho(\mathbf{x}, \tau) = D(\tau)\delta_\rho^{(1)}(\mathbf{x}) + D^2(\tau)\delta_\rho^{(2)}(\mathbf{x}) + D^3(\tau)\delta_\rho^{(3)}(\mathbf{x}) + \dots, \tag{4.5}$$

where $D(\tau)$ is the growth factor, $D(\tau)\delta_\rho^{(1)}(\mathbf{x})$ is the solution to the linearized equations and we kept only the fastest growing modes at each order. We can express $\tilde{\delta}_\rho^{(n)}$ as

$$\tilde{\delta}_\rho^{(n)}(\mathbf{k}) = \left[\prod_{i=1}^n \int \frac{\mathrm{d}^3 k_i}{(2\pi)^3}\right] (2\pi)^3 \delta_\mathrm{D}^{(3)}\left(\mathbf{k} - \sum_{i=1}^n \mathbf{k}_i\right) F_n(\mathbf{k}_1, \cdots, \mathbf{k}_n) \tilde{\delta}_\rho^{(1)}(\mathbf{k}_1) \cdots \tilde{\delta}_\rho^{(1)}(\mathbf{k}_n), \tag{4.6}$$

where the F_n's are called splitting functions and $F_1 = 1$. The velocity field is described by its divergence $\theta(\mathbf{x}, \tau) = \nabla \cdot \mathbf{v}(\mathbf{x}, \tau)$ which, similarly to the field $\delta_\rho(\mathbf{x}, \tau)$, can be written as a perturbative solution of the Euler and Poisson equations as

$$\theta(\mathbf{x}, \tau) = -\frac{\mathrm{d}D(\tau)}{\mathrm{d}\tau}\left(\theta^{(1)}(\mathbf{x}) + D(\tau)\theta^{(2)}(\mathbf{x}) + \dots\right) \tag{4.7}$$

where

$$\tilde{\theta}^{(n)}(\mathbf{k}) = \left[\prod_{i=1}^n \int \frac{\mathrm{d}^3 k_i}{(2\pi)^3}\right] (2\pi)^3 \delta_\mathrm{D}^{(3)}\left(\mathbf{k} - \sum_{i=1}^n \mathbf{k}_i\right) G_n(\mathbf{k}_1, \cdots, \mathbf{k}_n) \tilde{\delta}_\rho^{(1)}(\mathbf{k}_1) \cdots \tilde{\delta}_\rho^{(1)}(\mathbf{k}_n) \tag{4.8}$$

and $G_1 = 1$. In this chapter, we only need the explicit expressions [124] for F_2, G_2 and F_3, which are

$$F_2(\mathbf{k}_1, \mathbf{k}_2) = \frac{5}{7} + \frac{1}{2}\frac{\mathbf{k}_1 \cdot \mathbf{k}_2}{k_1 k_2}\left(\frac{k_1}{k_2} + \frac{k_2}{k_1}\right) + \frac{2}{7}\frac{(\mathbf{k}_1 \cdot \mathbf{k}_2)^2}{k_1^2 k_2^2}, \tag{4.9}$$

$$G_2(\mathbf{k}_1, \mathbf{k}_2) = \frac{3}{7} + \frac{1}{2}\frac{\mathbf{k}_1 \cdot \mathbf{k}_2}{k_1 k_2}\left(\frac{k_1}{k_2} + \frac{k_2}{k_1}\right) + \frac{4}{7}\frac{(\mathbf{k}_1 \cdot \mathbf{k}_2)^2}{k_1^2 k_2^2}, \tag{4.10}$$

$$\begin{aligned} F_3(\mathbf{k}_1, \mathbf{k}_2, \mathbf{k}_3) = & \frac{2k_{123}^2}{54}\left[\frac{\mathbf{k}_1 \cdot \mathbf{k}_{23}}{k_1^2 k_{23}^2} G_2(\mathbf{k}_2, \mathbf{k}_3) + (2\text{ cyclic})\right] \\ & + \frac{7}{54}\mathbf{k}_{123} \cdot \left[\frac{\mathbf{k}_{12}}{k_{12}^2} G_2(\mathbf{k}_1, \mathbf{k}_2) + (2\text{ cyclic})\right] \\ & + \frac{7}{54}\mathbf{k}_{123} \cdot \left[\frac{\mathbf{k}_1}{k_1^2} F_2(\mathbf{k}_2, \mathbf{k}_3) + (2\text{ cyclic})\right], \end{aligned} \tag{4.11}$$

where $\mathbf{k}_{ijl\ldots} = \mathbf{k}_i + \mathbf{k}_j + \mathbf{k}_l + \cdots$.

The matter overdensity perturbation field at linear order $\tilde{\delta}_\rho^{(1)}$ is related to the primordial curvature fluctuation $\tilde{\delta}_\zeta$ by

$$\tilde{\delta}_\rho^{(1)}(\mathbf{k}) = M(k)\tilde{\delta}_\zeta(\mathbf{k}) \tag{4.12}$$

where for small wavevectors $M(k) \propto k^2$, and for large wavevectors (below the nonlinear scale) $M(k) \sim \sqrt{k}$ [117]. For the purposes of analytical estimates, we will use the following approximate expression for $M(k)$

$$M(k) \simeq \left(\frac{2}{5\Omega_m}\right)\left[\frac{k^2}{H_0^2}\theta(q_0 - k) + \sqrt{\frac{k}{q_0}}\frac{q_0^2}{H_0^2}\theta(k - q_0)\right]. \tag{4.13}$$

Here $H_0 \simeq 70\,\mathrm{km\,s^{-1}Mpc^{-1}}$ is the Hubble constant today, $\Omega_m \simeq 0.3$ is the fraction of matter energy density, and $q_0 \simeq 0.015\,\mathrm{Mpc}^{-1}$.

Matter overdensity correlators are computed using the Effective Field Theory of Large Scale Structure (EFT-of-LSS) [125, 126]. We work only to leading order in this theory.

Galaxy Density Perturbations and Regularization Schemes

As mentioned in the Introduction, the galaxy overdensity field δ_g can be written as a biased tracer of the underlying matter overdensity field δ_ρ

$$\delta_g(\mathbf{x}) = b_1\delta_\rho(\mathbf{x}) + \frac{b_2}{2}\delta_\rho^2(\mathbf{x}) + \ldots . \tag{4.14}$$

In the equation above we omitted operators that are outside the scope of this chapter as well as the terms that set the expectation value of δ_g to zero. The general form of the additional terms represented by the ellipses in the bias expansion above is known [114] (even for different forms of the power spectrum) and it could include other operators that do not appear as counterterms [127].

The composite operators in Eq. (4.14) need to be regularized and renormalized. Here we will focus on the operator δ_ρ^2 as an illustration of the dependence of the counterterms on the regularization scheme. What we conclude could be generalized to other composite operators in the galaxy bias expansion. Generically, regularization is achieved by introducing a wavevector cutoff Λ in divergent integrals. Here we present three possible choices for the cutoff regulator.

The first regularization scheme we consider consists in cutting off the large wavevector component of the linearized solution $\delta_\rho^{(1)}$ of the gravitational evolution equations, i.e. performing the following replacement:

$$\delta_\rho^{(1)}(\mathbf{q}) \to \delta_\rho^{(1)}(\mathbf{q})\theta(\Lambda - q)\,. \tag{4.15}$$

As we will discuss in Sec. 4.3 this prescription reproduces the results previously found in [119] after assuming the UV asymptotic behavior for M given in Eq. (4.13). This prescription has the advantage that, had we worked at higher order in the EFT-of-LSS, it would have regulated both the correlators of δ_ρ and of the composite operator δ_ρ^2.

Since we are working to lowest order in the EFT-of-LSS we introduce a second and a third renormalization prescriptions for δ_ρ^2 that do not explicitly cut off large wavevectors in the non-linear gravitational evolution equations.

One choice is to cut off the large wavevectors of the *full* solution δ_ρ of the gravitational equations, i.e.

$$\delta_\rho(\mathbf{q}) \to \delta_\rho(\mathbf{q})\theta(\Lambda - q)\,, \tag{4.16}$$

which implies

$$\tilde{\delta}_\rho^2(\mathbf{k}) \to \int \frac{\mathrm{d}^3 q}{(2\pi)^3}\tilde{\delta}_\rho(\mathbf{q})\tilde{\delta}_\rho(\mathbf{k}-\mathbf{q})\theta(\Lambda - q)\theta(\Lambda - |\mathbf{k}-\mathbf{q}|)\,. \tag{4.17}$$

The third prescription is obtained from the second one by expanding for $k \ll q$ one of the two thetas in the convolution integral of δ_ρ^2 and keeping only the leading term.

$$\begin{aligned}\tilde{\delta}_\rho^2(\mathbf{k}) &\to \int \frac{\mathrm{d}^3 q}{(2\pi)^3}\tilde{\delta}_\rho(\mathbf{q})\tilde{\delta}_\rho(\mathbf{k}-\mathbf{q})\theta(\Lambda - q) \\ &= \int \frac{\mathrm{d}^3 q}{(2\pi)^3}\tilde{\delta}_\rho(\mathbf{q})\tilde{\delta}_\rho(\mathbf{k}-\mathbf{q})\left[\frac{\theta(\Lambda - q)+\theta(\Lambda - |\mathbf{k}-\mathbf{q}|)}{2}\right]. \end{aligned} \tag{4.18}$$

In the square bracket of the above equation we explicitly symmetrized the regularization kernel, thus rendering the expression manifestly symmetric in the two $\tilde{\delta}_\rho$'s. This last prescription leads to a spherically symmetric integration region (hence simplifying the integrals).

We find that all three regulators give the same non-boost invariant terms[2] and that they can be removed by expressing ϕ_G in Lagrangian coordinates as expected from the results of [119, 128]. After assuming a UV asymptotic behavior for M (e.g. the one in Eq. (4.13)), the second and third regulators give the same coefficients for the boost invariant terms which, however, differ from the ones in the first prescription. Hence, in the following, we will only discuss the first and the third regularization schemes.

We will deal with infrared divergences that arise in the computation of correlators of the galaxy overdensity field by expanding the integrands around $q = \infty$ and retaining only the terms that contribute to the UV divergence. These terms are infrared safe.

4.3 Renormalization of the operator δ_ρ^2 at one loop

The correlators of δ_g are sensitive to the physics of large wavevectors where perturbation theory is no longer valid. To make analytic predictions using a perturbative approach, composite operators in the galaxy bias expansion need to be regularized and renormalized adding counterterms that remove the sensitivity to the physics of large wavevectors. Following [115], we only keep the fastest growing modes in the computation of the counterterms.

Note that the composite operator δ_ρ^2 can ultimately be written as a convolution of fields ϕ_G at different wavevectors. Therefore, we find the one-loop counterterms by contracting two such fields, introducing a UV regulator Λ (as described in Sec. 4.2), and by selecting the parts that diverge as Λ goes to infinity.

Even though all the amplitudes presented in this chapter can be obtained applying Wick's theorem, such operation can be tedious and cumbersome. Therefore, we will

[2] In this chapter we refer to operators that diverge as a single wave-vector vanishes as non-boost invariant.

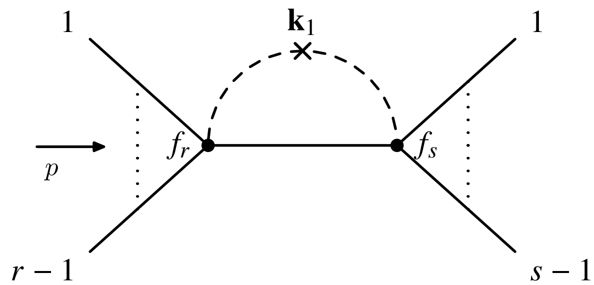

Figure 4.1: Generic one-loop divergent diagrams at first order in gravitational evolution.

use a diagrammatic formalism to graphically keep track of the different contributions in the renormalization of the operator δ_ρ^2 (see Appendix 4.B for details). Diagrams with N cross vertices represent contributions to the N-point galaxy overdensity field correlator $\langle\tilde{\delta}_g(\mathbf{k}_1)\ldots\tilde{\delta}_g(\mathbf{k}_N)\rangle$.

In this section, we discuss the one-loop renormalization of the quadratic operator δ_ρ^2 for local primordial non-Gaussianity. At the end of the section, we give the full renormalized expression of the operator δ_ρ^2 up to third order in gravitational evolution in the first and the third renormalization schemes introduced above. Using the first regularization prescription, we reproduce the results found in [119] after assuming the UV asymptotic behavior for M of Eq. (4.13).

First Order in Gravitational Evolution

In this subsection, we work at linear order in gravitational evolution, i.e. we set all the F_n's and G_n's (for $n>1$) to zero. We compute the counterterms needed to renormalize the operator δ_ρ^2 at one loop in the presence of primordial non-Gaussian perturbations of the form of Eq. (4.1). In Fig. 4.1, we show all the (amputated) one-loop divergent diagrams with a single insertion of δ_ρ^2. These diagrams are obtained by contracting a single ϕ_G from each δ_ρ in δ_ρ^2.

Here, the first regularization prescription gives

$$(2-\delta_{rs})rsf_rf_s\int\frac{\mathrm{d}^3q}{(2\pi)^3}M(q)M(|\mathbf{k}_1-\mathbf{q}|)P_\phi(|\mathbf{p}+\mathbf{q}|)\theta(\Lambda-q)\theta(\Lambda-|\mathbf{k}_1-\mathbf{q}|) \quad (4.19)$$

where $\mathbf{p}$ is the total wavevector entering the f_r vertex. We evaluate this kind of integral in cylindrical coordinates where the product of the two thetas can naturally be embedded in the integration measure.

The third regularization prescription gives

$$(2-\delta_{rs}) rs f_r f_s \sigma^2(\mathbf{k}_1, \mathbf{p}; \Lambda) \tag{4.20}$$

where

$$\sigma^2(\mathbf{k}_1, \mathbf{p}; \Lambda) = \int \frac{\mathrm{d}^3 q}{(2\pi)^3} M(q) M(|\mathbf{k}_1 - \mathbf{q}|) P_\phi(|\mathbf{p}+\mathbf{q}|) \left[\frac{\theta(\Lambda - q) + \theta(\Lambda - |\mathbf{k}_1 - \mathbf{q}|)}{2}\right] . \tag{4.21}$$

We embed the thetas in the integration measure and we expand the remaining part of the integrand around $q = \infty$, using the large wavevector asymptotic expression of Eq. (4.13) for M. We keep only the powers that give rise to UV divergent terms (i.e. all the terms up to q^{-2}). Note that terms in the integrand suppressed by powers of k/q give rise to finite contributions that are dropped. These terms do not contain IR or collinear divergences. After this procedure the divergent parts of the integral in Eq. (4.19) are

$$\sigma^2_{\mathrm{asy}} \equiv \frac{4}{25} \frac{A q_0^3}{\Omega_m^2 H_0^4} \frac{\Lambda}{2\pi^2} . \tag{4.22}$$

Due to the spherical symmetry of the integration region of Eq. (4.21), for the third prescription an alternative procedure can be followed. Expanding the integrand for $k_1, p \ll q$ and performing the angular integral $\mathrm{d}\Omega_q$, the linearly divergent part of Eq. (4.21) is

$$\sigma^2 \equiv \sigma^2(0, 0; \Lambda) = \int \frac{\mathrm{d}^3 q}{(2\pi)^3} M^2(q) P(q) \theta(\Lambda - q) . \tag{4.23}$$

σ^2 coincides with σ^2_{asy} when using the UV asymptotic expression for M of Eq. (4.13).

We therefore introduce the following position space counterterms to make correlators involving the operator $\tilde{\delta}^2_\rho$ finite as Λ goes to infinity

$$c_{r-1,s-1}(\Lambda) : \phi_G^{r-1}(\mathbf{x}) :: \phi_G^{s-1}(\mathbf{x}) : \tag{4.24}$$

where

$$c_{r-1,s-1}(\Lambda) = -rs f_r f_s \sigma^2_{\mathrm{asy}} \tag{4.25}$$

and σ^2 can be used in place of σ^2_{asy}. At one loop the two normal orderings in Eq. (4.24) can be merged to a single overall one, and consequently the counterterms take the form

$$c_n(\Lambda) : \phi_G^n(\mathbf{x}) : = \left(\sum_{i=0}^{n} c_{i,n-i}(\Lambda)\right) : \phi_G^n(\mathbf{x}) : \ . \tag{4.26}$$

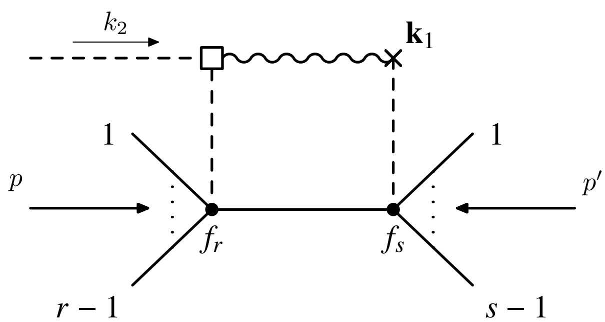

Figure 4.2: Diagrams with a single F_2 vertex used to determine the counterterm for δ_ρ^2 linear in δ_ρ.

As mentioned above the first and the third prescriptions give the same counterterms which up to second order in the field ϕ_G are

$$-\sigma_{\text{asy}}^2 \left[4 f_2\, \phi_G(\mathbf{x}) + (6 f_3 + 4 f_2^2)\; : \phi_G^2(\mathbf{x}) :\right] \,. \tag{4.27}$$

Second Order in Gravitational Evolution

We now study the effect of non-linear gravitational evolution on renormalization for non-Gaussian primordial fluctuations of the local type. In this case the renormalization of δ_ρ^2 will generate counterterms linear in $\delta_\rho^{(1)}$ (which will reassemble to δ_ρ when higher order terms are included).

We begin by considering Gaussian primordial fluctuations (see Fig. 4.2 choosing $r = 1$ and $s = 1$) and we evaluate its divergent coefficient in the first and third regularization prescriptions described in Sec. 4.2.

The first prescription gives

$$4 \int \frac{\mathrm{d}^3 q}{(2\pi)^3} F_2(\mathbf{q}, -\mathbf{k}_1) M^2(q) P_\phi(q) \theta(\Lambda - q) \,, \tag{4.28}$$

where we dropped thetas of the type $\theta(\Lambda - k_i)$ since $k_i < \Lambda$. Expanding for small k_1/q and performing the angular integral $\mathrm{d}\Omega_q$, the linearly divergent part of the above equation is

$$\frac{68}{21} \int \frac{\mathrm{d}q}{2\pi^2} q^2 M^2(q) P_\phi(q) \theta(\Lambda - q) = \frac{68}{21}\sigma^2 \simeq \frac{68}{21}\sigma_{\text{asy}}^2 \,, \tag{4.29}$$

where in the last step we assumed the UV asymptotic behavior of Eq.(4.13) for M. This result reproduces the counterterms already found in the literature [117].

For the third prescription, $\tilde{\delta}_\rho^2$ at this order is

$$\int \frac{\mathrm{d}^3 q}{(2\pi)^3} \left[\tilde{\delta}_\rho^{(2)}(\mathbf{q})\tilde{\delta}_\rho^{(1)}(\mathbf{k}_1 - \mathbf{q}) + \tilde{\delta}_\rho^{(1)}(\mathbf{q})\tilde{\delta}_\rho^{(2)}(\mathbf{k}_1 - \mathbf{q})\right] \theta(\Lambda - q) \,. \tag{4.30}$$

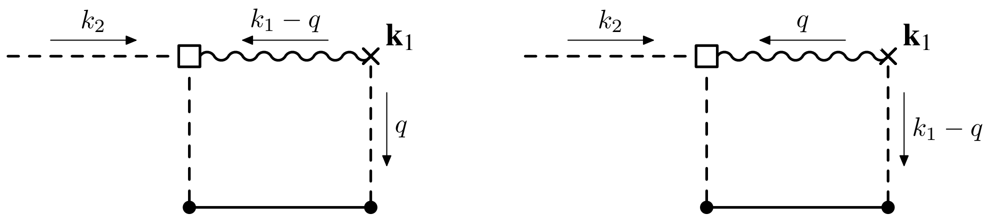

Figure 4.3: Two routings of the loop diagram with a single F_2 vertex used to determine the counterterm for δ_ρ^2 linear in δ_ρ with Gaussian primordial fluctuations.

Contracting one of the $\tilde{\phi}_G$ fields in $\tilde{\delta}_\rho^{(2)}$ with the $\tilde{\phi}_G$ field in $\tilde{\delta}_\rho^{(1)}$ gives an operator proportional to $\tilde{\delta}_\rho^{(1)}(\mathbf{k}_1)$ with (divergent) coefficient

$$2\int \frac{\mathrm{d}^3 q}{(2\pi)^3}\left[F_2(-\mathbf{q},\mathbf{k}_1)M^2(q)P_\phi(q)\right. \\ \left. + F_2(-\mathbf{k}_1+\mathbf{q},\mathbf{k}_1)M^2(|\mathbf{k}_1-\mathbf{q}|)P_\phi(|\mathbf{k}_1-\mathbf{q}|)\right]\theta(\Lambda-q)\,. \quad (4.31)$$

In diagrammatic notation, the two terms above are represented by the (amputated) diagrams of Fig. 4.3 and correspond to two ways of *routing* the loop wavevector. We observe that the two terms in the square bracket can be made equal to each other with the change of variable $\mathbf{q} \to \mathbf{k}_1 - \mathbf{q}$, however the *integrands* are not equal because of the presence of the theta function. Thus, we expect the above integrals to differ by a surface term which will impact the explicit form of the counterterms.

Expanding for small k_1/q and performing the angular integral $\mathrm{d}\Omega_q$, the linearly divergent parts of Eq. (4.31) are

$$\int \frac{\mathrm{d}q}{2\pi^2}\left\{\frac{34}{21}q^2M^2(q)P_\phi(q) + \frac{34}{21}q^2M^2(q)P_\phi(q) - \frac{1}{3}\frac{\mathrm{d}}{\mathrm{d}q}\left(q^3M^2(q)P_\phi(q)\right)\right\}\theta(\Lambda-q) = \frac{68}{21}\sigma^2 - \frac{1}{3}\rho^2 \quad (4.32)$$

where

$$\rho^2 = \int \frac{\mathrm{d}q}{2\pi^2}\left[\frac{\mathrm{d}}{\mathrm{d}q}\left(q^3M^2(q)P_\phi(q)\right)\right]\theta(\Lambda-q)\,. \quad (4.33)$$

On the left hand side of Eq. (4.32), the first term corresponds to the first routing while the other two terms correspond to the second routing. Notice that ρ^2 coincides with σ^2_{asy} when using the UV asymptotic expression for M of Eq. (4.13). As anticipated, the contributions from the two routings differ by a total derivative term. Since this term is linearly divergent, it will contribute to the value of the counterterm. We observe that the first term (bulk) on the right hand side of Eq. (4.32) is the same as the counterterm for the first prescription of Eq. (4.28). In loops containing box vertices (representing non-linear gravitational evolution), the third prescription — in diagrammatic formalism — entails symmetrizing the contribution of a diagram over the two possible routings in analogy to Fig. 4.3.

Non-Gaussian primordial fluctuations generate counterterms proportional to the operators $\delta_\rho^{(1)}\phi_G^n$. To determine their divergent coefficients we evaluate the diagrams in Fig. 4.2 in the regularization prescriptions described above. For each choice of r and s (s.t. $r+s=n$) we need to sum over two diagrams. Letting $\mathbf{p}$ and $\mathbf{p}'$ be the sum of the wavevectors entering the f_r and f_s vertices, respectively, the total amplitude is

$$2\,rsf_rf_s\int\frac{\mathrm{d}^3q}{(2\pi)^3}F_2(\mathbf{k}_1+\mathbf{k}_2-\mathbf{q},-\mathbf{k}_2)M(q)M(|\mathbf{k}_1+\mathbf{k}_2-\mathbf{q}|)\left[P_\phi(|\mathbf{p}+\mathbf{q}|)+P_\phi(|\mathbf{p}'+\mathbf{q}|)\right]\mathcal{R}_i \tag{4.34}$$

where the $\mathcal{R}_i$ is the regularization kernel in scheme i and

$$\mathcal{R}_1 = \theta(\Lambda-q)\theta(\Lambda-|\mathbf{k}_1+\mathbf{k}_2-\mathbf{q}|)\,, \tag{4.35}$$

$$\mathcal{R}_3 = \frac{\theta(\Lambda-q)+\theta(\Lambda-|\mathbf{k}_1-\mathbf{q}|)}{2}\,. \tag{4.36}$$

Proceeding as before, we obtain for the divergent parts

$$2\,rsf_rf_s\left(\frac{68}{21}+\frac{\mathbf{k}_2\cdot(\mathbf{p}+\mathbf{p}')}{k_2^2}\right)\sigma^2_{\mathrm{asy}}\,, \tag{4.37}$$

$$2\,rsf_rf_s\left[\left(\frac{68}{21}+\frac{\mathbf{k}_2\cdot(\mathbf{p}+\mathbf{p}')}{k_2^2}\right)\sigma^2-\frac{1}{3}\rho^2\right]\,. \tag{4.38}$$

We observe that within each regularization prescription presented in this chapter, the Gaussian and non-Gaussian coefficients of the k-independent parts coincide [119] up to a factor of $2rsf_rf_s$ (compare Eqs. (4.29) and (4.32) with Eqs. (4.37) and (4.38)). However, as expected [128], in the non-Gaussian case non-boost invariant terms proportional to $\mathbf{k}_2\cdot(\mathbf{p}+\mathbf{p}')/k_2^2$ appear. These shift the argument of the field ϕ_G from its Eulerian coordinate $\mathbf{x}$ to its initial Lagrangian position $\mathbf{x}_0$ (see Eq. (4.48)) and are the same in the three regularization schemes studied in this chapter.

Finally we notice that the two routings in the third prescription generate equal and opposite surface terms that are non-boost invariant. For example, for the counterterm

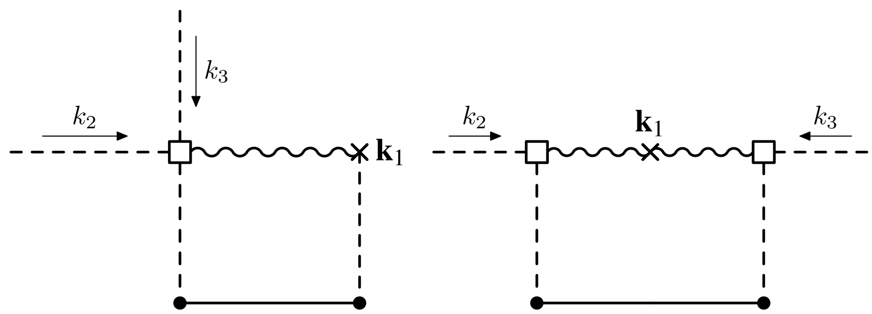

Figure 4.4: Diagrams with one F_3 and two F_2's used to determine the counterterms for δ_ρ^2 quadratic in δ_ρ with Gaussian primordial fluctuations.

proportional to $\delta_\rho^{(1)}\phi_G$ we get

$$4f_2 \int \frac{\mathrm{d}q}{2\pi^2}\left\{\left(\frac{34}{21}+\frac{\mathbf{k}_2\cdot\mathbf{k}_3}{2k_2^2}\right)q^2M^2(q)P_\phi(q)-\left(\frac{\mathbf{k}_2\cdot\mathbf{k}_3}{6k_2^2}+\frac{1}{3}\right)\frac{\mathrm{d}}{\mathrm{d}q}\left(q^3M^2(q)P_\phi(q)\right)\right.$$
$$\left.+\left(\frac{34}{21}+\frac{\mathbf{k}_2\cdot\mathbf{k}_3}{2k_2^2}\right)q^2M^2(q)P_\phi(q)+\frac{\mathbf{k}_2\cdot\mathbf{k}_3}{6k_2^2}\frac{\mathrm{d}}{\mathrm{d}q}\left(q^3M^2(q)P_\phi(q)\right)\right\}\theta(\Lambda-q) \tag{4.39}$$

where in this case $\mathbf{p} = \mathbf{k}_3$ and $\mathbf{p}' = 0$, and the two lines correspond to the two possible routings of the loop wavevector. Again we note that the non-boost invariant surface terms proportional to $(\mathbf{k}_2\cdot\mathbf{k}_3)/k_2^2$ cancel when considering both routings.

Third Order in Gravitational Evolution

We now consider the one-loop counterterms at second order in the field $\delta_\rho^{(1)}$. We have two different diagram topologies (the Gaussian ones are shown in Fig. 4.4). The amplitudes for the two topologies at arbitrary order in primordial local non-Gaussianity are

$$12\,rs f_r f_s \int \frac{\mathrm{d}^3q}{(2\pi)^3}F_3(\mathbf{k}_1+\mathbf{k}_2+\mathbf{k}_3-\mathbf{q},-\mathbf{k}_2,-\mathbf{k}_3)M(q)M(|\mathbf{k}_1+\mathbf{k}_2+\mathbf{k}_3-\mathbf{q}|)$$
$$\left[P_\phi(|\mathbf{q}+\mathbf{p}|)+P_\phi(|\mathbf{q}+\mathbf{p}'|)\right]\mathcal{R}_i^{(a)}\,, \tag{4.40}$$

and

$$16\,rs f_r f_s \int \frac{\mathrm{d}^3q}{(2\pi)^3}F_2(\mathbf{q}+\mathbf{k}_2,-\mathbf{k}_2)F_2(\mathbf{k}_1+\mathbf{k}_3-\mathbf{q},-\mathbf{k}_3)M(|\mathbf{q}+\mathbf{k}_2|)M(|\mathbf{k}_1+\mathbf{k}_3-\mathbf{q}|)$$
$$\left[P_\phi(|\mathbf{q}+\mathbf{p}+\mathbf{k}_2|)+P_\phi(|\mathbf{q}+\mathbf{p}'+\mathbf{k}_2|)\right]\mathcal{R}_i^{(b)}\,. \tag{4.41}$$

In the equations above,

$$\mathcal{R}_1^{(a)} = \theta(\Lambda - q)\theta(\Lambda - |\mathbf{k}_1 + \mathbf{k}_2 + \mathbf{k}_3 - \mathbf{q}|)\,, \tag{4.42}$$

$$\mathcal{R}_1^{(b)} = \theta(\Lambda - |\mathbf{q} + \mathbf{k}_2|)\theta(\Lambda - |\mathbf{k}_1 + \mathbf{k}_3 - \mathbf{q}|)\,, \tag{4.43}$$

and $\mathcal{R}_3^{(a)} = \mathcal{R}_3^{(b)}$ are given in Eq. (4.36).

We now give the full renormalized expression of the operator δ_ρ^2 up to third order in the gravitational evolution for local primordial non-Gaussianity. For completeness we reintroduce the subtraction of the vacuum expectation value $\langle\delta_\rho^2\rangle$.

For the first prescription we have

$$\delta_\rho^2(\mathbf{x})\big|_R = \delta_\rho^2(\mathbf{x}) - \sigma_{\rm asy}^2 \mathcal{S}[\phi_G]\left[1 + \frac{68}{21}\delta_\rho(\mathbf{x}) + \frac{2624}{735}\delta_\rho^2(\mathbf{x}) + \frac{254}{2205}\left(\frac{\partial_i\partial_j}{\nabla^2}\delta_\rho(\mathbf{x})\right)\left(\frac{\partial_i\partial_j}{\nabla^2}\delta_\rho(\mathbf{x})\right)\right]\,, \tag{4.44}$$

which reproduces the results of [119] after using the UV asymptotic expression $\sigma_{\rm asy}^2$ in place of σ^2 for the Gaussian cases.

When using the third prescription we obtain

$$\begin{aligned}\delta_\rho^2(\mathbf{x})\big|_R = \delta_\rho^2(\mathbf{x}) - \mathcal{S}[\phi_G]\Bigg[&\sigma^2 + \left(\frac{68}{21}\sigma^2 - \frac{1}{3}\rho^2\right)\delta_\rho(\mathbf{x}) + \\ &+ \left(\frac{2624}{735}\sigma^2 - \frac{73}{105}\rho^2 + \frac{1}{30}\gamma^2\right)\delta_\rho^2(\mathbf{x}) + \\ &+ \left(\frac{254}{2205}\sigma^2 - \frac{16}{105}\rho^2 + \frac{1}{15}\gamma^2\right)\left(\frac{\partial_i\partial_j}{\nabla^2}\delta_\rho(\mathbf{x})\right)\left(\frac{\partial_i\partial_j}{\nabla^2}\delta_\rho(\mathbf{x})\right)\Bigg]\,,\end{aligned} \tag{4.45}$$

where

$$\gamma^2 = \int \frac{\mathrm{d}q}{2\pi^2}\left\{\frac{\mathrm{d}}{\mathrm{d}q}\left[q^4\frac{\mathrm{d}}{\mathrm{d}q}\left(M^2(q)P_\phi(q)\right)\right]\right\}\theta(\Lambda - q). \tag{4.46}$$

In the above equations

$$\mathcal{S}[\phi_G] = 1 + 4f_2\phi_G(\mathbf{x}_0) + (6f_3 + 4f_2^2) : \phi_G^2(\mathbf{x}_0) : + \cdots \tag{4.47}$$

where, at this order in the gravitational evolution,

$$\begin{aligned}\phi_G(\mathbf{x}_0) = \phi_G(\mathbf{x}) &+ \left(\frac{\partial_\ell}{\nabla^2}\delta_\rho(\mathbf{x})\right)\partial_\ell\phi_G(\mathbf{x}) - \frac{1}{2}\frac{\partial_\ell}{\nabla^2}\left\{\delta_\rho^2(\mathbf{x}) - \left(\frac{\partial_i\partial_j}{\nabla^2}\delta_\rho(\mathbf{x})\right)^2\right\}\partial_\ell\phi_G(\mathbf{x}) \\ &+ \frac{1}{2}\left(\frac{\partial_i}{\nabla^2}\delta_\rho(\mathbf{x})\right)\left(\frac{\partial_j}{\nabla^2}\delta_\rho(\mathbf{x})\right)\partial_i\partial_j\phi_G(\mathbf{x})\end{aligned} \tag{4.48}$$

and the ellipses in Eq. (4.47) can be deduced from Eq. (4.25) and Eq. (4.26). In Eq.(4.47) the one corresponds to the Gaussian case and the remaining terms arise from primordial non-Gaussianity. The relationship between the counterterms in the Gaussian and non-Gaussian cases was first noted in [119].

4.4 Concluding Remarks

Composite operators in the bias expansion for the galaxy overdensity field are defined with a large wavevector cutoff (Λ) and are renormalized to remove the dependence of galaxy overdensity correlators on the wavevector cutoff. In this chapter we explored the regularization scheme dependence of the counterterms in the Galaxy bias expansion. We showed by explicit computation how different regularization prescriptions affect the coefficients of the counterterms. As expected the coefficients of the non-boost invariant operators coincide for the regularization schemes explored in this chapter and they rearrange to shift the argument of the field ϕ_G from Eulerian to Lagrangian coordinates. On the other hand, the boost-invariant terms are dependent on the regularization scheme. Our calculations illustrate the power of the general methods developed in Refs. [119, 128].

4.A Conformal Invariance of δ_ζ correlators at tree-level

In this Appendix, we prove that in local non-Gaussianity all the tree-level correlators of the curvature fluctuations δ_ζ are conformally invariant.

We start by introducing a diagrammatic notation for the N-point correlators $P^{(N)}$ defined as

$$\langle \tilde{\delta}_\zeta(\mathbf{k}_1) \dots \tilde{\delta}_\zeta(\mathbf{k}_N) \rangle = (2\pi)^3 \delta(\mathbf{k}_1 + \dots + \mathbf{k}_N) P^{(N)}(\mathbf{k}_1, \dots, \mathbf{k}_N) \,. \tag{A.1}$$

We separate the sum of all the tree-level contributions ($T^{(N)}$) from the sum of the loop contributions using the following notation

$$P^{(N)}(\mathbf{k}_1, \dots, \mathbf{k}_N) = T^{(N)}(\mathbf{k}_1, \dots, \mathbf{k}_N) + \text{loops} \,, \tag{A.2}$$

and we shall refer to $T^{(N)}$ as the tree-level correlator in wavevector space.

Using δ_ζ as in Eq. (4.1), we first consider the case where only f_1 and f_2 are non-zero. Then, it is straightforward to see that the tree-level N-point correlator is

$$T^{(N)}(\mathbf{k}_1, \dots, \mathbf{k}_N) = 2^{N-2} A^{N-1} f_1^2 f_2^{N-2} \frac{1}{2} \sum_{\mathcal{P}(\mathbf{k}_1 \dots \mathbf{k}_N)} \frac{1}{k_1^3} \frac{1}{|\mathbf{k}_1 + \mathbf{k}_2|^3} \cdots \frac{1}{|\mathbf{k}_1 + \dots + \mathbf{k}_{N-1}|^3} \,, \tag{A.3}$$

Figure A.1: Generic chain diagram.

where the sum is over all the permutations $\mathcal{P}(\mathbf{k}_1 \ldots \mathbf{k}_N)$ of the wavevectors. The diagram in Figure A.1 represents the identity permutation contribution to $T^{(N)}$ above.

More generally, contributions to the N-point function can be represented by diagrams with N vertices (dots) connected by solid lines.

To compute the connected tree-level N-point function of $\tilde{\delta}_\zeta$, we first draw all the connected tree diagrams with N vertices, i.e. different topologies. For each diagram we arbitrarily assign the wavevectors $\mathbf{k}_1, \mathbf{k}_2, \ldots \mathbf{k}_N$ to the various vertices.

We then use the following rules to compute the contribution to $T^{(N)}$ of each diagram.

- Every vertex with n lines emerging from it contributes a factor of f_n.
- Every line between two vertices contributes a factor $\dfrac{A}{|\sum_i \mathbf{k}_i|^3}$ where the sum is over the wavevectors that precede and include either of the two vertices along the tree (these two choices are equivalent due to overall wavevector conservation).
- Every diagram has a combinatorial factor that is given by the number of ways in which the lines from the various vertices can be joined together.
- Every diagram has a symmetry factor that is given by the inverse of the number of symmetries the diagram has. For example, the diagram in Fig. A.1 has a symmetry factor of $1/2$ because of the reflection symmetry of the chain around its center while the second diagram in Fig. A.2 has a symmetry factor of $1/3!$.

Finally, we sum over the $N!$ permutations of the wavevectors $\mathcal{P}(\mathbf{k}_1, \ldots, \mathbf{k}_N)$.

For example, the full expression for $T^{(4)}$ is given below and corresponds to the two diagrams in Fig. A.2, where we didn't label the vertices since the sum over

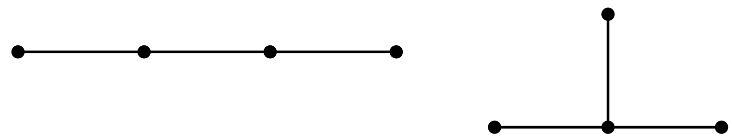

Figure A.2: Contributions to $T^{(4)}$.

permutations is implied

$$T^{(4)} = 2^2 A^3 f_1^2 f_2^2 \frac{1}{2} \sum_{\mathcal{P}(\mathbf{k}_1,\ldots,\mathbf{k}_N)} \frac{1}{k_1^3 k_2^3 |\mathbf{k}_1 + \mathbf{k}_2|^3} + A^3 f_1^3 f_3 3! \frac{1}{3!} \sum_{\mathcal{P}(\mathbf{k}_1,\ldots,\mathbf{k}_N)} \frac{1}{k_1^3 k_2^3 k_4^3} . \tag{A.4}$$

It is convenient to introduce the following notation:

$$T^{(N)}(\mathbf{k}_1, \ldots, \mathbf{k}_N) = \sum_{i \in \left\{\substack{\text{topologies} \\ \text{with } N \\ \text{vertices}}\right\}} T_i^{(N)}(\mathbf{k}_1, \ldots, \mathbf{k}_N) = \sum_{i \in \left\{\substack{\text{topologies} \\ \text{with } N \\ \text{vertices}}\right\}} \sum_{\mathcal{P}(\mathbf{k}_1,\ldots,\mathbf{k}_N)} t_i^{(N)}(\mathbf{k}_1, \ldots, \mathbf{k}_N) , \tag{A.5}$$

where we split each tree-level N-point function into a sum of terms from different topologies each of which is further expressed as a sum over the $N!$ permutations $[\mathcal{P}(\mathbf{k}_1, \ldots, \mathbf{k}_N)]$ of the external wavevectors.

Most inflationary models predict almost scale invariant δ_ζ correlators (with conformal weight $\Delta = 0$), some of which are also conformally invariant [129].

In Primordial local Non-Gaussianity, δ_ζ is a function of powers of ϕ_G only (and not its derivatives). Being that the two point function of the Gaussian field ϕ_G is scale invariant, we expect δ_ζ correlators to be scale invariant as well. In the following, we demonstrate that the conformal invariance of any tree-level N-point correlator of δ_ζ follows from the conformal invariance of the $N = 2$ correlator of ϕ_G. Moreover, we explicitly show that this holds separately for each topology and each permutation. Conformal invariance of the correlators implies that the conformal Ward identities are satisfied,

$$\left[\left(\sum_{\substack{j=1 \\ j \neq \alpha}}^{N} \mathcal{K}_j\right) t_i^{(N)}(\mathbf{k}_1, \ldots, \bar{\mathbf{k}}_\alpha, \ldots, \mathbf{k}_N)\right]_{\bar{\mathbf{k}}_\alpha = -\sum_{\beta \neq \alpha} \mathbf{k}_\beta} = 0 , \tag{A.6}$$

where

$$\mathcal{K}_j \equiv 2(\Delta - 3)\nabla_j - 2(\mathbf{k}_j \cdot \nabla_j)\nabla_j + \mathbf{k}_j \nabla_j^2 . \tag{A.7}$$

Here, $\mathcal{K}_j$ are the generators of special conformal transformations in wavevector space and $\nabla_j \equiv \partial_{\mathbf{k}_j}$. In our case Δ is equal to zero.

We choose the α'th wavevector to be the dependent one and we use the overall wavevector conservation to express that wavevector in terms of the others. Any tree-level $(N+1)-$point diagram can be constructed from an $N-$point tree-level diagram by adding a line to one of its N vertices. Labelling this vertex with the wavevector $\mathbf{k}_\alpha$ and choosing it to be the dependent one as before, we have the recursion relation

$$t_{i'}^{(N+1)}(\mathbf{k}_1, \ldots, \mathbf{k}_\alpha, \ldots, \mathbf{k}_{N+1}) = \frac{f_{m(\alpha)+1}}{f_{m(\alpha)}} t_i^{(N)}(\mathbf{k}_1, \ldots, \mathbf{k}_\alpha, \ldots, \mathbf{k}_N) \frac{A}{|\mathbf{k}_{N+1}|^3} \tag{A.8}$$

where $m(\alpha)$ is the number of legs emerging from the α'th vertex in $t_i^{(N)}$. Therefore, the conformal Ward identities for the $t_{i'}^{(N+1)}$ diagram are

$$\begin{aligned}
&\left[\left(\sum_{j=1,\, j\neq\alpha}^{N+1} \mathcal{K}_j\right) t_{i'}^{(N+1)}(\mathbf{k}_1, \ldots, \bar{\mathbf{k}}_\alpha, \ldots, \mathbf{k}_{N+1})\right]_{\bar{\mathbf{k}}_\alpha = -\sum_{\beta\neq\alpha}\mathbf{k}_\beta} \\
= \quad & \frac{A}{|\mathbf{k}_{N+1}|^3}\left[\frac{f_{m(\alpha)+1}}{f_{m(\alpha)}}\left(\sum_{j=1,\, j\neq\alpha}^{N} \mathcal{K}_j\right) t_i^{(N)}(\mathbf{k}_1, \ldots, \bar{\mathbf{k}}_\alpha, \ldots, \mathbf{k}_N)\right]_{\bar{\mathbf{k}}_\alpha = -\sum_{\beta\neq\alpha}\mathbf{k}_\beta} + \\
+ \quad & \mathcal{K}_{N+1}\left(\frac{A}{|\mathbf{k}_{N+1}|^3}\right)\left[\frac{f_{m(\alpha)+1}}{f_{m(\alpha)}} t_i^{(N)}(\mathbf{k}_1, \ldots, \bar{\mathbf{k}}_\alpha, \ldots, \mathbf{k}_N)\right]_{\bar{\mathbf{k}}_\alpha = -\sum_{\beta\neq\alpha}\mathbf{k}_\beta} .
\end{aligned} \tag{A.9}$$

Using the above equation recursively the conformal invariance of the $N-$point function follows from the conformal invariance of the two-point function. The above proof can be trivially extended to $\Delta \neq 0$.

4.B Feynman Rules for the Galaxy Bias expansion

Here we describe the diagrammatic formalism we use to graphically keep track of the different contributions in the renormalization of the operator δ_ρ^2. We find the diagrammatic notation introduced here closer to the Feynman diagrams typically used in particle physics compared to what is present in the literature.

For the calculations performed in this chapter we need three kinds of vertices — the dot, the box and the cross — and three kinds of lines — the solid, the dashed and the wavy. Fig B.1 shows the factors associated with each of the above elements. The f_i and F_n vertices describe the effect of primordial non-Gaussianities and non-linear gravitational evolution respectively. The b_i vertices represent the insertion of the operator $\left(\delta_\rho\right)^i$ in correlators of the galaxy overdensity field. Solid and dashed lines

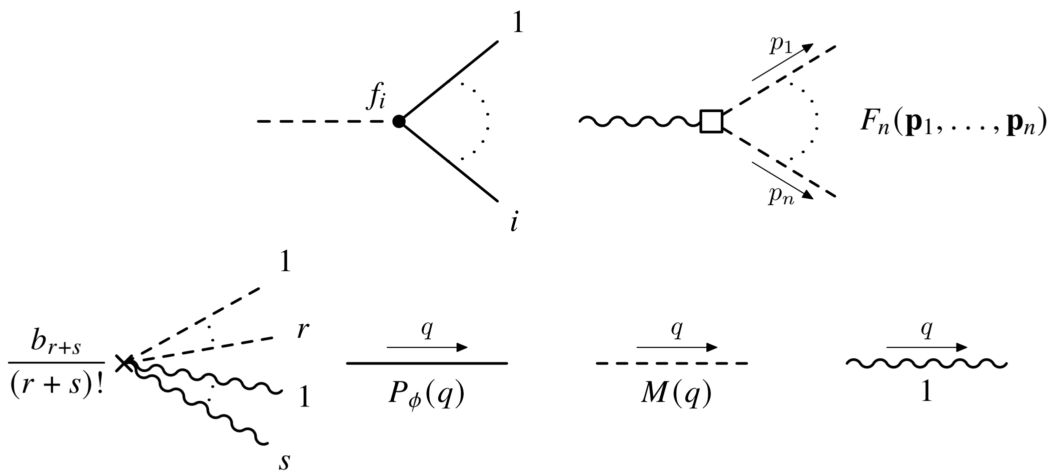

Figure B.1: Feynman rules for the vertices and the lines used in the computation of galaxy overdensity field correlators.

denote the power spectrum P_ϕ of the Gaussian field and the transfer function M introduced in Eqs. (4.2) and (4.12), respectively.

Valid diagrams representing contributions to the connected correlators of the galaxy overdensity field δ_g in wavevector space are drawn using the following rules,

- Every f_i vertex (dot) is connected to a dashed line and to i solid lines;
- Every F_n vertex (box) is connected to a wavy line and to n dashed lines. Each dashed line is connected to a solid line;
- Every b_i vertex (cross) is connected to r wavy lines and s dashed lines where $r + s = i$, $r, s \geq 0$.

Diagrams with N cross vertices represent contributions to the galaxy overdensity field correlator $\langle \tilde{\delta}_g(\mathbf{k}_1) \ldots \tilde{\delta}_g(\mathbf{k}_N) \rangle$. To translate a diagram into a formula, we label the N cross vertices (arbitrarily) with wavevectors $\mathbf{k}_1, \ldots, \mathbf{k}_N$ conventionally considered to be incoming. Then, we multiply the factors obtained using the following rules and sum over all the distinct ($N!$) labelings of the $\mathbf{k}_i$'s.

- Label each internal line with a different wavevector $\mathbf{q}_j$ and assign a factor $P_\phi(q_j)$ to solid lines, $M(q_j)$ to dashed lines and 1 to wavy lines;
- Assign factors of f_i, $F_n(\mathbf{p}_1, \ldots, \mathbf{p}_n)$ and $b_{r+s}/(r+s)!$ to the dot, the box, and the cross vertices as shown in Fig. B.1;

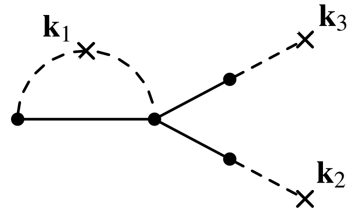

Figure B.2: Diagram contributing to the three point function of the galaxy overdensity field.

- Further assign a factor of $(2\pi)^3\delta^3(\mathbf{k}_i - \mathbf{p})$ to each cross labelled with wavevector $\mathbf{k}_i$, and a factor of $(2\pi)^3\delta^3(\mathbf{p})$ to each dot and box vertex, being $\mathbf{p}$ the sum of the outgoing wavevectors at the vertex. This imposes wavevector conservation at each vertex;
- Integrate over all the internal wavevectors $\int d^3\mathbf{q}_j/(2\pi)^3$. For each loop, this procedure will leave an unconstrained wavevector $\mathbf{q}_i$ to be integrated over;
- Assign a factor that takes into account the number of possible "Wick contractions".

As anticipated in Sec.4.2 for loop diagrams regularization is needed to make the results finite. The three regularization prescriptions discussed in the main text are implemented in this diagrammatic notation as follows:

- For the first regularization scheme adopted in this chapter, we assign a $\theta(\Lambda - p)$ to each dashed line in a loop with wavevector $\mathbf{p}$ flowing into it;
- For the second regularization scheme, we assign a $\theta(\Lambda - p)$ to each line stemming from the cross vertex in the loop with wavevector $\mathbf{p}$ flowing into it;
- For the third regularization scheme (i.e. cutting off the convolution integral of δ_ρ^2) the additional Feynman rule for loops prescribes summing over two thetas as in Eq. (4.18) and dividing by a factor of two. This corresponds to the two ways of *routing* the loop wavevector $\mathbf{q}$ (e.g. Fig. 4.3).

We will now present an illustrative example to familiarize the reader with the notation.

The contribution to the bispectrum of the diagram in Fig. B.2 in the third regularization scheme is

$$12\, b_1^2 \frac{b_2}{2} f_3 M(k_2)M(k_3)P_\phi(k_2)P_\phi(k_3) \int \frac{d^3q}{(2\pi)^3} M(q)M(|\mathbf{k}_1 - \mathbf{q}|)P_\phi(q) \left[\frac{\theta(\Lambda - q) + \theta(\Lambda - |\mathbf{k} - \mathbf{q}|)}{2}\right]. \tag{B.1}$$

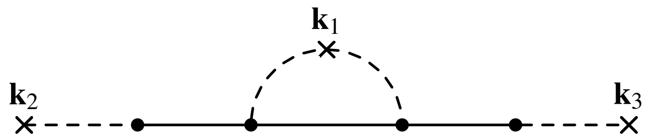

Figure B.3: Example of an infrared divergent diagram.

Using Eq. (4.13) the finite parts of loop integrals can easily be estimated in the region $k_i < q_0$. For example for the integral in Eq. (B.1) we have

$$\int \frac{d^3q}{(2\pi)^3} P_\phi(q) M(q) \left[M(|\mathbf{q} - \mathbf{k}_1|) - M(q) \right] \theta(\Lambda - q) \underset{|\mathbf{k}_1| < q_0}{\sim} \frac{A}{2\pi^2} \left(\frac{2}{5\Omega_m} \right)^2 \frac{k_1^2 q_0^2}{H_0^4} . \tag{B.2}$$

In the text we addressed infrared divergences by expanding the integrands of loop diagrams and truncating the infrared divergent parts. Alternatively, infrared divergences in correlators of the galaxy overdensity field can be removed by introducing an infrared regulator m, modifying the tree-level power spectrum of the primordial curvature fluctuations as

$$P_\phi(q) \to \frac{A}{(q^2 + m^2)^{3/2}} . \tag{B.3}$$

For example, the contribution to the galaxy overdensity bispectrum in Fig. B.3 is

$$2 \frac{b_2}{2} b_1^2 f_2^2 M(k_2) M(k_3) P_\phi(k_2) P_\phi(k_3) \sigma^2(\mathbf{k}_1, \mathbf{k}_2; \Lambda, m) + \{\mathbf{k}_2 \leftrightarrow \mathbf{k}_3\} \tag{B.4}$$

where

$$\sigma^2(\mathbf{k}_1, \mathbf{k}_2; \Lambda, m) = \int \frac{d^3q}{(2\pi)^3} \frac{A M(q) M(|\mathbf{k}_1 - \mathbf{q}|)}{(|\mathbf{q} + \mathbf{k}_2|^2 + m^2)^{3/2}} \theta(\Lambda - q) . \tag{B.5}$$

Most of the dependence on the infrared regulator m in the above integral is from the region of integration where the argument of M is less than q_0. We find that

$$\sigma^2(\mathbf{k}_1, \mathbf{k}_2; m; \Lambda) = \left(\frac{2}{5\Omega_m H_0} \right)^2 A \frac{k_3^2 |\mathbf{k}_1 - \mathbf{k}_2|^2}{4\pi^2} \log\left(\frac{q_0^2}{m^2} \right) + \text{IR finite as } \frac{m}{q_0} \to 0 . \tag{B.6}$$

For a wide range of $m/H_0 \ll 1$, the correlators of the galaxy overdensity field depend very weakly on the exact value of m.

Chapter 5

THE GALAXY BISPECTRUM IN THE SPHERICAL FOURIER-BESSEL BASIS

The bispectrum, the three-point correlation in Fourier space, is a crucial statistic for studying many effects targeted by the next-generation galaxy surveys, such as primordial non-Gaussianity (PNG) and general relativistic (GR) effects on large scales. In this chapter we develop a formalism for the bispectrum in the Spherical Fourier-Bessel (SFB) basis — a natural basis for computing correlation functions on the curved sky, as it diagonalizes the Laplacian operator in spherical coordinates. Working in the SFB basis allows for line-of-sight effects such as redshift space distortions (RSD) and GR to be accounted for exactly, i.e. without having to resort to perturbative expansions to go beyond the plane-parallel approximation. Only analytic results for the SFB bispectrum exist in the literature given the intensive computations needed. We numerically calculate the SFB bispectrum for the first time, enabled by a few techniques: We implement a template decomposition of the redshift-space kernel Z_2 into Legendre polynomials, and separately treat the PNG and velocity-divergence terms. We derive an identity to integrate a product of three spherical harmonics connected by a Dirac delta function as a simple sum, and use it to investigate the limit of a homogeneous and isotropic Universe. Moreover, we present a formalism for convolving the signal with separable window functions, and use a toy spherically symmetric window to demonstrate the computation and give insights into the properties of the observed bispectrum signal. While our implementation remains computationally challenging, it is a step toward a feasible full extraction of information on large scales via a SFB bispectrum analysis.

5.1 Introduction

Current and next-generation large-scale-structure (LSS) surveys such as DESI [130], Euclid [131], SPHEREx [132] and the *Nancy Grace Roman* Space Telescope [133] will measure the galaxy density field over increasingly larger angular scales, enabling us to constrain interesting physical effects that become important on those scales, such as primordial non-Gaussianity [134] (PNG) and general relativistic effects [135].

While many of our current techniques for estimators and modeling are well-suited for small-area surveys, they are challenged in larger surveys due to the breaking down of previously used approximations on the full sky. In particular, the plane-parallel approximation, which assumes that each galaxy has the same line-of-sight, breaks down when the galaxy separation becomes large in a full-sky survey. Additionally, the Newtonian modeling of galaxy density also breaks down as general relativistic effects that grow as $1/k$ become important on large scales (for details see Refs. [136–139]).

More precisely, redshift space distortions (RSD) induce effects in the observed galaxy density field that depend on the line-of-sight (LOS) of individual galaxies. Estimators assuming a fixed LOS for the entire survey will inevitably lose information at large galaxy separations. Even if one uses Yamamoto-like estimators [140–142] which assume a fixed LOS for each galaxy pair or triplet, there is still loss of information as the galaxies could have large angular separations in a given pair or triplet. The signal picked up by the Yamamoto estimator also includes wide-angle effects that are usually modeled either perturbatively as an expansion in the angular separation of the galaxy pair (i.e. an expansion whose zero-order term is the plane-parallel approximation) [143–146], or non-perturbatively via an exact calculation in the correlation function space [147].

This raises the question of whether the Fourier basis is the optimal basis to use on the full sky. Indeed, the Fourier basis consists of the eigenfunctions of the Laplacian in Cartesian coordinates; the spherical Fourier-Bessel (SFB) basis, consisting of the eigenfunctions of the Laplacian in spherical coordinates, is a more natural basis for data analysis on the curved sky. The SFB basis was proposed for studying galaxy surveys since the early '90s [148, 149], and was applied to data in the context of a power spectrum analysis in Refs. [150–152].

Recently, an important limitation of the SFB analysis has been overcome in Ref. [153], rendering computations of the power spectrum much more feasible: a boundary condition at the lower end of the redshift range was introduced, avoiding the need to carry many modes to model vanishing power outside of the survey footprint, which can introduce numerical instabilities. Later, the authors of Ref. [154] developed a SFB power spectrum estimator with a public code release, which builds on this improvement as well as those in Ref. [155] on pixel window effects and the separation of angular and radial transforms, making a SFB analysis feasible for surveys measuring the power spectrum such as *Nancy Grace Roman*, SPHEREx, and Euclid (see also [156, 157]).

An alternative to the SFB basis called tomographic spherical harmonics (TSH) has also been explored in the literature, where the galaxy density contrast in a redshift bin is decomposed into spherical harmonics, and many redshift bins are used. In the limit of thin bins, neighboring bins are highly correlated, and the covariance matrix could become nearly degenerate. For thick bins, one loses information about the radial modes that are smaller than the bin size. SFB modes, in contrast, are more efficient basis functions since the radial modes are captured by spherical Bessel functions which are orthogonal to each other, unlike in the case of the redshift bin decomposition. See Ref. [158] for a detailed analysis comparing the SFB and TSH power spectrum (at $\Delta z = 0.1$) for current and future surveys, showing better $f_{\rm NL}$ constraints in general for the SFB method.

Limited effort, however, has been dedicated to the study of the SFB bispectrum. The bispectrum is the 3-point correlation function in Fourier space and is of great importance to next-generation surveys. It is shown to be powerful at breaking parameter degeneracies when combined with the power spectrum for constraining galaxy bias parameters, neutrino masses, and primordial non-Gaussianities (see e.g. [132, 159–162]); the odd-parity bispectrum is also a smoking-gun signature for general relativistic effects that become more important on large scales [163–165].

A comprehensive derivation of the SFB bispectrum including all first and second-order GR effects, geometric effects and PNG was achieved in Ref. [166]. However, due to the complexity of the computations involved, there has not yet been any work numerically evaluating the SFB bispectrum signal. In fact, while most of the integrals involved in calculating the signal are three-dimensional and are doable, some of the most important and interesting ones involving RSD and PNG contributions are four-dimensional and are intractable to compute naively.

In this chapter, we derive a mathematical identity to express the six dimensional angular integral of three spherical harmonics connected by a Dirac-delta function as a simple sum, and use it to study the bispectrum signal in a homogeneous and isotropic Universe, to build intuition for later understanding the observed bispectrum in a realistic Universe. We also use this identity to accelerate the computation of RSD and PNG terms contributing to the observed bispectrum signal. Furthermore, we employ a template decomposition of the second-order coupling kernel in redshift space Z_2 into products of Legendre polynomials to evaluate all three-dimensional integrals. These techniques allow us to calculate and visualize for the first time the SFB bispectrum signal.

We apply a general formalism we develop for convolution with a separable window function (in the angular and radial direction) to the toy example of a spherically symmetric window function to obtain numerical results that we study in detail. We derive key insights into the properties of the observed SFB bispectrum in a realistic Universe, highlighting those due to geometric effects.

The structure of this chapter is as follows. In Section 5.2 we review the SFB basis and the modeling of the SFB galaxy power spectrum; we also describe the modeling of the Fourier space tree-level galaxy bispectrum and define the SFB bispectrum. Then in Section 5.3 we explore the calculation of the SFB bispectrum in the simplest case of a homogeneous and isotropic Universe, building up key intuition for interpreting the features of the observed bispectrum in the next section. In Section 5.4, we incorporate various observational effects into the bispectrum, including growth of structure, galaxy bias, RSD, PNG, and the survey window function. We present our template decomposition technique to enable its calculation, deferring the details of the derivation to the appendices; we then visualize and analyze the behavior of the observed bispectrum signal. Finally, we conclude and discuss future work in Section 5.5.

5.2 Background

In this section, we begin by reviewing the SFB formalism and the SFB power spectrum following Ref. [154], to which we refer the readers for more details. We then review the Fourier space bispectrum, and describe the modeling of the observed galaxy bispectrum in redshift space including local PNG. Finally, we define the SFB bispectrum, which we later compute in Sections 5.3 and 5.4.

The SFB formalism

The spherical Fourier-Bessel mode $\delta_{\ell m}(k)$ of the density contrast field $\delta(\boldsymbol{r})$ is defined by

$$\delta_{\ell m}(k) \equiv \int \mathrm{d}^3\boldsymbol{r} \left[\sqrt{\frac{2}{\pi}}\, k\, j_\ell(kr)\, Y^*_{\ell m}(\hat{\boldsymbol{r}})\right] \delta(\boldsymbol{r})\,. \tag{5.1}$$

The inverse transform is then

$$\delta(\boldsymbol{r}) = \int \mathrm{d}k \sum_{\ell m} \left[\sqrt{\frac{2}{\pi}}\, k\, j_\ell(kr)\, Y_{\ell m}(\hat{\boldsymbol{r}})\right] \delta_{\ell m}(k)\,, \tag{5.2}$$

where $\boldsymbol{r} = r\hat{\boldsymbol{r}}$ is the position vector, r is the comoving distance from the origin, and $\hat{\boldsymbol{r}}$ is the line-of-sight direction.

The spherical Fourier-Bessel modes are related to the Fourier modes via

$$\delta_{\ell m}(k) = \frac{k}{(2\pi)^{\frac{3}{2}}}\, i^{\ell} \int \mathrm{d}^2\hat{\boldsymbol{k}}\, Y^*_{\ell m}(\hat{\boldsymbol{k}})\, \delta(\boldsymbol{k})\,, \tag{5.3}$$

for which the inverse relation is

$$\delta(\boldsymbol{k}) = \frac{(2\pi)^{\frac{3}{2}}}{k} \sum_{\ell m} i^{-\ell}\, Y_{\ell m}(\hat{\boldsymbol{k}})\, \delta_{\ell m}(k)\,. \tag{5.4}$$

Note that in this chapter we use the following convention for the Fourier transform:

$$f(\boldsymbol{k}) = \int \mathrm{d}^3 r\, e^{-i\boldsymbol{k}\cdot\boldsymbol{r}}\, f(\boldsymbol{r})\,, \tag{5.5}$$

$$f(\boldsymbol{r}) = \int \frac{\mathrm{d}^3 k}{(2\pi)^3}\, e^{i\boldsymbol{k}\cdot\boldsymbol{r}}\, f(\boldsymbol{k})\,. \tag{5.6}$$

If unambiguous, we use the same symbol in configuration space (e.g., $f(\boldsymbol{r})$) as in Fourier space (e.g., $f(\boldsymbol{k})$).

Observed galaxy SFB power spectrum

Let us denote the expansion of the matter density in cosmological perturbation theory by

$$\delta(\boldsymbol{k}, r) = \sum_{n=1}^{\infty} D^n(r)\delta^{(n)}(\boldsymbol{k})\,, \tag{5.7}$$

with $D(r)$ the growth factor. Then, in the linear regime, the observed galaxy density contrast to first order can be modeled as

$$\delta^{g,\mathrm{obs},(1)}(\boldsymbol{r}) = W(\boldsymbol{r})\, D(r) \int \frac{\mathrm{d}^3\boldsymbol{q}}{(2\pi)^3}\, e^{i\boldsymbol{q}\cdot\boldsymbol{r}}\, \widetilde{A}_{\mathrm{RSD}}(\mu, q\mu, r) b(r,q)\, \delta^{(1)}(\boldsymbol{q})\,, \tag{5.8}$$

where $W(\boldsymbol{r})$ is the survey window, $b(r,q)$ is the linear galaxy bias, $\mu = \hat{\boldsymbol{r}}\cdot\hat{\boldsymbol{q}}$, and $\delta^{(1)}(\boldsymbol{q})$ is the matter density contrast in Fourier space. In what follows, the matter density contrast will always be denoted δ without any superscript, while the galaxy density contrast is denoted by δ^g.

RSD effects are contained in $\widetilde{A}_{\mathrm{RSD}}(\mu, q\mu, r)$, which can be modeled as

$$\widetilde{A}_{\mathrm{RSD}}(\mu, q\mu, r) = \left(1 + \beta\mu^2\right) \widetilde{A}_{\mathrm{FoG}}(q\mu)\,, \tag{5.9}$$

where $\beta = f/b$ and $f = \mathrm{d}\ln D/\mathrm{d}\ln a$ (with a the scale factor) is the linear growth rate. In this chapter we ignore the Fingers-of-God effect and set $\widetilde{A}_{\mathrm{FoG}}(q\mu) = 1$.

Transforming to spherical Fourier-Bessel space we have that

$$\delta_{\ell m}^{g,\mathrm{obs},(1)}(k) = \int \mathrm{d}q \sum_{LM} \mathcal{W}_{\ell m}^{LM}(k,q)\, \delta_{LM}^{(1)}(q)\,, \tag{5.10}$$

where the observed galaxy density $\delta_{\ell m}^{g,\mathrm{obs}}(k)$ is related to the matter density $\delta_{LM}(q)$ by the mode coupling matrix $\mathcal{W}_{\ell m}^{LM}(k,q)$. In our convention, this mode coupling matrix encodes galaxy physics such as galaxy bias and RSD effects, unequal time effects such as the growth of structure, and the survey window function $W(\mathbf{r})$:

$$\mathcal{W}_{\ell m}^{LM}(k,q) = \int \mathrm{d}^2\hat{\boldsymbol{r}}\, Y_{LM}(\hat{\boldsymbol{r}})\, Y_{\ell m}^*(\hat{\boldsymbol{r}})\, \mathcal{W}_\ell^L(k,q,\hat{\boldsymbol{r}})\,, \tag{5.11}$$

where

$$\mathcal{W}_\ell^L(k,q,\hat{\boldsymbol{r}}) = \frac{2qk}{\pi} \int \mathrm{d}r\, r^2\, W(\boldsymbol{r})\, D(r)\, b(r,q)\, j_\ell(kr) \widetilde{A}_{\mathrm{RSD}}(-i\partial_{qr}, -iq\partial_{qr}, r) j_L(qr)\,, \tag{5.12}$$

where we replace the argument μ of $\widetilde{A}_{\mathrm{RSD}}$ by $-i\partial_{qr}$ which acts on $e^{i\boldsymbol{q}\cdot\boldsymbol{r}} = e^{iqr\mu}$.

Noting that in a homogeneous and isotropic Universe, the matter power spectrum satisfies

$$\langle \delta(\boldsymbol{k})\delta^*(\boldsymbol{k}')\rangle = (2\pi)^3 \delta^D\left(\boldsymbol{k}-\boldsymbol{k}'\right) P(k)\,, \tag{5.13}$$

it follows that the 2-point function of the SFB modes is

$$\left\langle \delta_{\ell m}^{g,\mathrm{obs}}(k)\, \delta_{\ell' m'}^{g,\mathrm{obs},*}(k') \right\rangle = \int \mathrm{d}q \sum_{LM} \mathcal{W}_{\ell m}^{LM}(k,q)\, \mathcal{W}_{\ell' m'}^{LM,*}(k',q)\, P(q)\,. \tag{5.14}$$

In the full-sky limit where $W(\mathbf{r}) = W(r)$, we have that $\mathcal{W}_\ell^L(k,q,\hat{\boldsymbol{r}}) \to \mathcal{W}_\ell^\ell(k,q)$ is independent of $\hat{\boldsymbol{r}}$. Let us define $\mathcal{W}_\ell(k,q) \equiv \mathcal{W}_\ell^\ell(k,q)$. Then the SFB power spectrum $C_\ell(k,k')$ defined via

$$\left\langle \delta_{\ell m}^{g,\mathrm{obs}}(k)\, \delta_{\ell' m'}^{g,\mathrm{obs},*}(k') \right\rangle = \delta^K_{\ell\ell'}\delta^K_{mm'}\, C_\ell(k,k')\,, \tag{5.15}$$

can be expressed as

$$C_\ell(k,k') = \int \mathrm{d}q\, \mathcal{W}_\ell(k,q)\, \mathcal{W}_\ell^*(k',q)\, P(q)\,, \tag{5.16}$$

where

$$\mathcal{W}_\ell(k,q) = \frac{2qk}{\pi} \int \mathrm{d}r\, r^2\, W(r)\, D(r)\, j_\ell(kr) \Big(b(r,q) j_\ell(qr) - f(r) j_\ell''(qr) \Big), \tag{5.17}$$

where we use Eq. 5.9 with $\mu \to -i\partial_{qr}$.

Note that in a homogeneous and isotropic Universe, for which $b(r,q) = D(r) = \widetilde{A}_{\rm RSD} = W(\boldsymbol{r}) = 1$, $\mathcal{W}_\ell(k,q)$ becomes a Dirac delta function and we have that $C_l(k,k') = \delta_D(k-k')P(k)$. In reality, the kernels $\mathcal{W}_\ell(k,q)$ are peaked at $k \approx q$. We show examples of $\mathcal{W}_\ell(k,q)$ for the spherical window $W(r) = \mathbf{1}_{[0,r_{\rm max}]}(r)$ for various values of $r_{\rm max}$ in Fig. 5.1, where we fix $k = 4.18 \times 10^{-2}$ and vary q/k for $\ell = 20$. Here and in the remainder of this chapter we use the Planck 2018 cosmology [5] as our fiducial cosmology. The matter power spectrum at zero redshift and the linear growth factors f and D are computed with the Boltzmann code `CAMB`[1] [167]. All other calculations are performed in Julia [168].

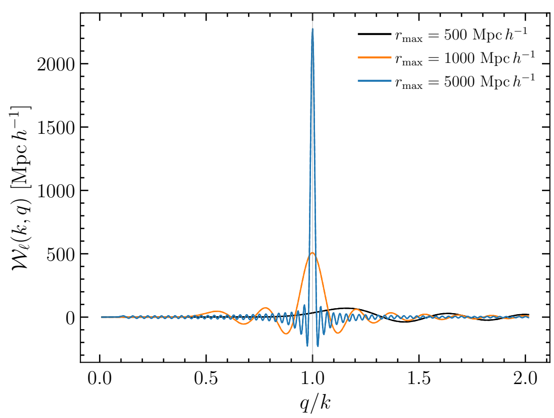

Figure 5.1: $\mathcal{W}_\ell(k,q)$ for fixed $\ell = 20$, $k = 4.18 \times 10^{-2}$ hMpc^{-1} and for various sizes $r_{\rm max}$ of the survey window $W(r) = \mathbf{1}_{[0,r_{\rm max}]}(r)$.

Observed Fourier galaxy bispectrum

We now review the observed galaxy bispectrum in Fourier space including observational effects such as the RSD and galaxy bias, but without the window function convolution. For details on the derivation of the various quantities, we refer the readers to Ref. [169] and [170] which we follow closely. As we will also be concerned with modeling the effects of PNG in the SFB bispectrum, we will include its effects in the Fourier bispectrum as well.

We consider PNG of the local type, for which the fluctuations of the potential are parameterized by

$$\Phi_{\rm NG}(\boldsymbol{x}) = \varphi(\boldsymbol{x}) + f_{\rm NL}\left(\varphi^2(\boldsymbol{x}) - \left\langle \varphi^2 \right\rangle\right)\,, \tag{5.18}$$

[1] https://camb.info/

where φ is a primordial Gaussian potential. Using the Poisson equation, we may relate the long-wavelength Gaussian potential to the linearly evolved primordial matter density perturbation via

$$\Phi_{\mathrm{NG}}(\boldsymbol{k}) = \frac{\delta^{(1)}(\boldsymbol{k}, z)}{\alpha(k, z)}\,, \tag{5.19}$$

where

$$\alpha(k, z) = \frac{2k^2 c^2 D(z) T(k)}{3H_0^2 \Omega_{\mathrm{m}}}\,. \tag{5.20}$$

Here Ω_m is the matter density, H_0 is the Hubble constant, and $T(k)$ is the transfer function of matter perturbations, normalized to 1 at low k. Eq. 5.19-5.20 are valid in the Newtonian limit on subhorizon scales [171–173].

In perturbation theory, the observed galaxy density contrast field at position $\boldsymbol{r}$ is given by

$$\begin{aligned}\delta^{g}(\boldsymbol{k}, \boldsymbol{r}) = \sum_{n=1}^{\infty} D^n(r) \int \frac{\mathrm{d}^3\boldsymbol{k}_1}{(2\pi)^3} \cdots \int \frac{\mathrm{d}^3\boldsymbol{k}_n}{(2\pi)^3} (2\pi)^3 \delta_D(\boldsymbol{k}_1 + \cdots + \boldsymbol{k}_n - \boldsymbol{k}) \\ \times Z_n(\boldsymbol{k}_1, \ldots, \boldsymbol{k}_n, \boldsymbol{r})\, \delta^{(1)}(\boldsymbol{k}_1) \cdots \delta^{(1)}(\boldsymbol{k}_n)\,,\end{aligned} \tag{5.21}$$

where $\delta^{(1)}$ is the linear matter density field, and the n-th order redshift space kernels Z_n encode the mode coupling effects from gravitational evolution, PNG and galaxy biasing. We assume the bivariate galaxy biasing model

$$\delta^{\mathrm{g}}(\boldsymbol{x}) = b_{10}^{\mathrm{E}}\delta(\boldsymbol{x}) + b_{01}^{\mathrm{E}}\varphi(\boldsymbol{x}) + b_{20}^{\mathrm{E}}\left(\delta(\boldsymbol{x})\right)^2 + b_{11}^{\mathrm{E}}\delta(\boldsymbol{x})\varphi(\boldsymbol{x}) + b_{02}^{\mathrm{E}}(\varphi(\boldsymbol{x}))^2 + b_{s_2}\left(s^2 - \left\langle s^2\right\rangle\right) - b_{01}^{\mathrm{E}} n^2\,. \tag{5.22}$$

Above we define the tidal term [174, 175]

$$s^2(\boldsymbol{k}) = \int \frac{d\boldsymbol{q}}{(2\pi)^3} S_2(\boldsymbol{q}, \boldsymbol{k}-\boldsymbol{q})\delta^{(1)}(\boldsymbol{q})\delta^{(1)}(\boldsymbol{k}-\boldsymbol{q}), \tag{5.23}$$

and the (non-Gaussian) term encoding displacement of galaxies from their initial Lagrangian coordinate positions $\boldsymbol{q}$

$$n^2(\boldsymbol{k}) = 2\int \frac{d\boldsymbol{q}}{(2\pi)^3} N_2(\boldsymbol{q}, \boldsymbol{k}-\boldsymbol{q}) \frac{\delta^{(1)}(\boldsymbol{q})\delta^{(1)}(\boldsymbol{k}-\boldsymbol{q})}{\alpha(|\boldsymbol{k}-\boldsymbol{q}|)}\,, \tag{5.24}$$

where above we use the kernels

$$N_2\left(\boldsymbol{k}_1, \boldsymbol{k}_2\right) = \frac{\boldsymbol{k}_1 \cdot \boldsymbol{k}_2}{2k_1^2}\,, \tag{5.25}$$

$$S_2\left(\boldsymbol{k}_1, \boldsymbol{k}_2\right) = \frac{(\boldsymbol{k}_1 \cdot \boldsymbol{k}_2)^2}{k_1^2 k_2^2} - \frac{1}{3}\,. \tag{5.26}$$

The redshift space kernels at first and second order, respectively, are given by

$$Z_1(\boldsymbol{k},\boldsymbol{r}) = b^{\mathrm{E}}_{10} + f(r)\mu^2 + \frac{b^{\mathrm{E}}_{01}}{\alpha(k)}, \tag{5.27}$$

$$\begin{aligned}
Z_2(\boldsymbol{k}_1,\boldsymbol{k}_2,\boldsymbol{r}) = {} & b^{\mathrm{E}}_{10}\left[F_2\left(\boldsymbol{k}_1,\boldsymbol{k}_2\right) + f_{\mathrm{NL}}\frac{\alpha(k)}{\alpha\left(k_1\right)\alpha\left(k_2\right)}\right] + \left[b^{\mathrm{E}}_{20} - \frac{2}{7}b^{\mathrm{L}}_{10}S_2\left(\boldsymbol{k}_1,\boldsymbol{k}_2\right)\right] \\
& + \frac{b^{\mathrm{E}}_{11}}{2}\left[\frac{1}{\alpha\left(k_1\right)} + \frac{1}{\alpha\left(k_2\right)}\right] + \frac{b^{\mathrm{E}}_{02}}{\alpha\left(k_1\right)\alpha\left(k_2\right)} - b^{\mathrm{E}}_{01}\left[\frac{N_2\left(\boldsymbol{k}_1,\boldsymbol{k}_2\right)}{\alpha\left(k_2\right)} + \frac{N_2\left(\boldsymbol{k}_2,\boldsymbol{k}_1\right)}{\alpha\left(k_1\right)}\right] \\
& + f(r)\mu^2\left[G_2\left(\boldsymbol{k}_1,\boldsymbol{k}_2\right) + f_{\mathrm{NL}}\frac{\alpha(k)}{\alpha\left(k_1\right)\alpha\left(k_2\right)}\right] + \frac{f(r)^2k^2\mu^2}{2}\frac{\mu_1\mu_2}{k_1k_2} \\
& + b^{\mathrm{E}}_{10}\frac{f(r)\mu k}{2}\left(\frac{\mu_1}{k_1} + \frac{\mu_2}{k_2}\right) + b^{\mathrm{E}}_{01}\frac{f(r)\mu k}{2}\left[\frac{\mu_1}{k_1\alpha\left(k_2\right)} + \frac{\mu_2}{k_2\alpha\left(k_1\right)}\right],
\end{aligned} \tag{5.28}$$

where $\mu \equiv \hat{\boldsymbol{k}}\cdot\hat{\boldsymbol{r}}$, $\boldsymbol{k} \equiv \boldsymbol{k}_1 + \boldsymbol{k}_2$, $\mu_i \equiv \hat{\boldsymbol{k}}_i\cdot\hat{\boldsymbol{r}}$, and where the coupling kernels for the real-space density and velocity-divergence fields are

$$F_2(\boldsymbol{q}_1,\boldsymbol{q}_2) = \frac{5}{7} + \frac{1}{2}\left(\frac{q_1}{q_2} + \frac{q_2}{q_1}\right)\frac{\boldsymbol{q}_1\cdot\boldsymbol{q}_2}{q_1q_2} + \frac{2}{7}\frac{(\boldsymbol{q}_1\cdot\boldsymbol{q}_2)^2}{(q_1q_2)^2}, \tag{5.29}$$

$$G_2(\boldsymbol{q}_1,\boldsymbol{q}_2) = \frac{3}{7} + \frac{1}{2}\left(\frac{q_1}{q_2} + \frac{q_2}{q_1}\right)\frac{\boldsymbol{q}_1\cdot\boldsymbol{q}_2}{q_1q_2} + \frac{4}{7}\frac{(\boldsymbol{q}_1\cdot\boldsymbol{q}_2)^2}{(q_1q_2)^2}. \tag{5.30}$$

From Eq. 5.27 it follows that we may write the linear galaxy bias appearing in Eq. 5.17 as $b(r,q) = b^{\mathrm{E}}_{10} + b^{\mathrm{E}}_{01}/\alpha(q,r)$.

The galaxy bispectrum in Fourier space is defined via

$$\langle\delta^g(\boldsymbol{k}_1,\boldsymbol{r}_1)\delta^g(\boldsymbol{k}_2,\boldsymbol{r}_2)\delta^g(\boldsymbol{k}_3,\boldsymbol{r}_3)\rangle = B_s(\boldsymbol{k}_1,\boldsymbol{k}_2,\boldsymbol{k}_3,\boldsymbol{r}_1,\boldsymbol{r}_2,\boldsymbol{r}_3)(2\pi)^3\delta_D(\boldsymbol{k}_1+\boldsymbol{k}_2+\boldsymbol{k}_3). \tag{5.31}$$

Working up to second order in the galaxy density field expansion, the tree-level bispectrum is

$$\begin{aligned}
B_s(\boldsymbol{k}_1,\boldsymbol{k}_2,\boldsymbol{k}_3,\boldsymbol{r}_1,\boldsymbol{r}_2,\boldsymbol{r}_3) \equiv {} & 2D(r_1)D(r_2)D^2(r_3)P(k_1)P(k_2)Z_1(\boldsymbol{k}_1,\boldsymbol{r}_1)Z_1(\boldsymbol{k}_2,\boldsymbol{r}_2)Z_2(\boldsymbol{k}_1,\boldsymbol{k}_2,\boldsymbol{r}_3) \\
& + 2\text{ cyc. perm.},
\end{aligned} \tag{5.32}$$

where we sum over all cyclic permutations of the subscripts of the quantities in parentheses. Note that in the absence of RSD, linear growth, galaxy bias, and PNG, Eq. 5.32 reduces to the matter bispectrum

$$B_m(\boldsymbol{k}_1,\boldsymbol{k}_2,\boldsymbol{k}_3) \equiv 2P(k_1)P(k_2)F_2(\boldsymbol{k}_1,\boldsymbol{k}_2) + 2\text{ cyc. perm.}. \tag{5.33}$$

We follow Ref. [169] to model the Eulerian biases

$$b_{10}^{\mathrm{E}} = 1 + b_{10}^{\mathrm{L}}\,, \tag{5.34}$$
$$b_{01}^{\mathrm{E}} = b_{01}^{\mathrm{L}}\,, \tag{5.35}$$
$$b_{20}^{\mathrm{E}} = \frac{8}{21} b_{10}^{\mathrm{L}} + b_{20}^{\mathrm{L}}\,, \tag{5.36}$$
$$b_{11}^{\mathrm{E}} = b_{01}^{\mathrm{L}} + b_{11}^{\mathrm{L}}\,, \tag{5.37}$$
$$b_{02}^{\mathrm{E}} = b_{02}^{\mathrm{L}}\,, \tag{5.38}$$

in terms of the Lagrangian biases, which are given by

$$b_{01}^{\mathrm{L}} = 2 f_{\mathrm{NL}} \delta_c b_{10}^{\mathrm{L}}, \tag{5.39}$$
$$b_{11}^{\mathrm{L}} = 2 f_{\mathrm{NL}} \left(\delta_c b_{20}^{\mathrm{L}} - b_{10}^{\mathrm{L}} \right), \tag{5.40}$$
$$b_{02}^{\mathrm{L}} = 4 f_{\mathrm{NL}}^2 \delta_c \left(\delta_c b_{20}^{\mathrm{L}} - 2 b_{10}^{\mathrm{L}} \right)\,, \tag{5.41}$$

if one assumes a Universal Mass Function, and where δ_c is the critical overdensity for halo collapse, here set to its value for spherical collapse $\delta_c = 1.686$.

Note that only b_{10}^{E} and b_{20}^{E} need to be specified in order to determine all the other bias parameters. Specifically for our SFB bispectrum computation later, we will set $b_{10}^{E} = 1.8$ and $b_{20}^{E} = 0.305$. While there is no technical obstacle to including redshift-dependent biases in the SFB calculation, we choose flat biases here for simplicity.

SFB bispectrum definition

We now review the formalism for the SFB bispectrum. We seek to compute the 3-point correlation function of the observed galaxy over-density field in SFB space:

$$\left\langle \delta_{l_1 m_1}^{g,\mathrm{obs}}(k_1)\, \delta_{l_2 m_2}^{g,\mathrm{obs}}(k_2) \delta_{l_3 m_3}^{g,\mathrm{obs}}(k_3) \right\rangle\,. \tag{5.42}$$

In the following, it will be useful to distinguish between two notions of isotropy, which we term *observational* isotropy and *intrinsic* isotropy. Intrinsic isotropy refers to the statistically isotropic distribution of galaxies on the largest-scales in real-space. Due to RSD, the galaxy clustering observed in surveys is not intrinsically isotropic since, in redshift space, it depends on the angle to a given LOS. On the other hand, the distribution observed by a full-sky survey remains invariant under rotations about the observer position. This observational isotropy is only broken by a survey window which is not spherically symmetric. We show in Appendix 5.B that, assuming observational isotropy, Eq. 5.42 is real and proportional to the Gaunt factor

$$\mathcal{G}^{l_1 l_2 l_3}_{m_1 m_2 m_3} \equiv \int \mathrm{d}^2\hat{\boldsymbol{r}}\, Y_{l_1 m_1}(\hat{\boldsymbol{r}})\, Y_{l_2 m_2}(\hat{\boldsymbol{r}})\, Y_{l_3 m_3}(\hat{\boldsymbol{r}})\,, \tag{5.43}$$

which can be expressed in terms of Wigner-$3j$ symbols,

$$\mathcal{G}^{l_1 l_2 l_3}_{m_1 m_2 m_3} = \left(\frac{(2l_1+1)(2l_2+1)(2l_3+1)}{4\pi}\right)^{\frac{1}{2}} \begin{pmatrix} l_1 & l_2 & l_3 \\ 0 & 0 & 0 \end{pmatrix} \begin{pmatrix} l_1 & l_2 & l_3 \\ m_1 & m_2 & m_3 \end{pmatrix}\,. \tag{5.44}$$

The Wigner-$3j$'s ensure the SFB 3-point function vanishes unless the following conditions are satisfied: (i) $m_1 + m_2 + m_3 = 0$, (ii) triangle inequality on the l_i: $l_i \geq l_j - l_k$, and (iii) $l_1 + l_2 + l_3$ is even.

In order to rid of the purely geometric information contained in the m_i, we compute the "angle-averaged" bispectrum

$$B^{\mathrm{SFB}}_{l_1 l_2 l_3}(k_1, k_2, k_3) \equiv \sum_{m_1, m_2, m_3} \begin{pmatrix} l_1 & l_2 & l_3 \\ m_1 & m_2 & m_3 \end{pmatrix} \left\langle \delta^{g,\mathrm{obs}}_{l_1 m_1}(k_1) \delta^{g,\mathrm{obs}}_{l_2 m_2}(k_2) \delta^{g,\mathrm{obs}}_{l_3 m_3}(k_3) \right\rangle\,. \tag{5.45}$$

Using the orthogonality relation in Eq. A.24 then gives

$$\left\langle \delta^{g,\mathrm{obs}}_{l_1 m_1}(k_1) \delta^{g,\mathrm{obs}}_{l_2 m_2}(k_2) \delta^{g,\mathrm{obs}}_{l_3 m_3}(k_3) \right\rangle = \begin{pmatrix} l_1 & l_2 & l_3 \\ m_1 & m_2 & m_3 \end{pmatrix} B^{\mathrm{SFB}}_{l_1 l_2 l_3}(k_1, k_2, k_3)\,. \tag{5.46}$$

In the following subsections we will always plot the dimensionless reduced bispectrum

$$Q^{\mathrm{SFB}}_{l_1 l_2 l_3}(k_1, k_2, k_3) \equiv \frac{B^{\mathrm{SFB}}_{l_1 l_2 l_3}(k_1, k_2, k_3)}{P(k_1)P(k_2) + P(k_1)P(k_3) + P(k_2)P(k_3)}\,, \tag{5.47}$$

which partially projects out the dependence of the signal on k_i coming from the matter power spectrum. Finally, we note that the bispectrum is invariant under simultaneous cyclic permutations of (l_1, l_2, l_3) and (k_1, k_2, k_3), which allows us to restrict to $l_1 \leq l_2 \leq l_3$.

Before delving into the computation of the SFB bispectrum, let us briefly remark on its relation to the angular bispectrum in spherical shells (i.e., the TSH bispectrum) $b_{l_1 l_2 l_3}(r_1, r_2, r_3)$ of Ref. [147], defined via

$$\begin{aligned} \mathcal{G}^{l_1 l_2 l_3}_{m_1 m_2 m_3}\, b_{l_1 l_2 l_3}(r_1, r_2, r_3) \equiv \int d^2\hat{\boldsymbol{r}}_1 d^2\hat{\boldsymbol{r}}_2 d^2\hat{\boldsymbol{r}}_3\, & Y^*_{l_1 m_1}(\hat{\boldsymbol{r}}_1) Y^*_{l_2 m_2}(\hat{\boldsymbol{r}}_2) Y^*_{l_3 m_3}(\hat{\boldsymbol{r}}_3) \\ & \times \left\langle \delta^{g,\mathrm{obs}}(\boldsymbol{r}_1)\, \delta^{g,\mathrm{obs}}(\boldsymbol{r}_2)\, \delta^{g,\mathrm{obs}}(\boldsymbol{r}_3) \right\rangle\,. \end{aligned} \tag{5.48}$$

Using Eq. 5.46 in combination with Eq. 5.1, it follows that

$$B^{\mathrm{SFB}}_{l_1l_2l_3}(k_1,k_2,k_3) = \left(\frac{2}{\pi}\right)^{\frac{3}{2}} k_1k_2k_3 \int \left(\prod_i \mathrm{d}r_i r_i^2 j_{l_i}(k_ir_i)\right) b_{l_1l_2l_3}(r_1,r_2,r_3)\,. \quad (5.49)$$

We see that the SFB bispectrum and the TSH bispectrum are related by an invertible linear transformation, and that the multipole indices l_i are the same in the SFB and TSH formalisms (the wavenumbers k_i are the same between SFB and Fourier space). In practice, in the TSH formalism many radial bins are desirable to fully exploit the large scale radial modes (see [158], which studied this for the power spectrum), leading to a covariance matrix which is difficult to invert, whereas this issue does not arise in the SFB basis.

5.3 SFB bispectrum in a homogeneous and isotropic Universe

Key identity for fast computation

We first examine the bispectrum in the limit of a homogeneous and intrinsically isotropic Universe (by ignoring the growth of structure, galaxy bias evolution, redshift-space distortions and window function effects) in order to study its features and build up intuition for understanding the observed SFB bispectrum later in Section 5.4.

We can relate the SFB bispectrum to the Fourier bispectrum using the relation between the SFB and Fourier modes in Eq. 5.3:

$$\begin{aligned}\left\langle \delta_{l_1m_1}(k_1)\,\delta_{l_2m_2}(k_2)\,\delta_{l_3m_3}(k_3)\right\rangle &= \frac{k_1k_2k_3}{(2\pi)^{9/2}}\, i^{l_1+l_2+l_3} \\ \times \int d^2\hat{\boldsymbol{k}}_1\, d^2\hat{\boldsymbol{k}}_2\, d^2\hat{\boldsymbol{k}}_3\, Y^*_{l_1m_1}(\hat{\boldsymbol{k}}_1)\, Y^*_{l_2m_2}(\hat{\boldsymbol{k}}_2)\, Y^*_{l_3m_3}(\hat{\boldsymbol{k}}_3)\, &\langle \delta(\boldsymbol{k}_1)\,\delta(\boldsymbol{k}_2)\,\delta(\boldsymbol{k}_3)\rangle\,. \end{aligned} \quad (5.50)$$

Due to homogeneity and isotropy, the Fourier bispectrum $B_m(k_1,k_2,k_3)$ (Eq. 5.33) depends only on the lengths k_1, k_2, and k_3, so that we may write

$$\left\langle \delta_{l_1m_1}(k_1)\,\delta_{l_2m_2}(k_2)\delta_{l_3m_3}(k_3)\right\rangle = \frac{k_1k_2k_3}{(2\pi)^{\frac{9}{2}}} i^{l_1+l_2+l_3}(2\pi)^3 B_m(k_1,k_2,k_3)\; I^{l_1l_2l_3}_{m_1m_2m_3}(k_1,k_2,k_3), \quad (5.51)$$

where

$$I^{l_1l_2l_3}_{m_1m_2m_3}(k_1,k_2,k_3) \equiv \int d^2\hat{\boldsymbol{k}}_1 d^2\hat{\boldsymbol{k}}_2 d^2\hat{\boldsymbol{k}}_3 Y^*_{l_1,m_1}(\hat{\boldsymbol{k}}_1)Y^*_{l_2,m_2}(\hat{\boldsymbol{k}}_2)Y^*_{l_3,m_3}(\hat{\boldsymbol{k}}_3)\delta_D(\boldsymbol{k}_1+\boldsymbol{k}_2+\boldsymbol{k}_3). \quad (5.52)$$

Eq. 5.52 has typically been written in terms of an integral over the spherical Bessel functions [166] (for details, see Appendix 5.C) as

$$I^{l_1 l_2 l_3}_{m_1 m_2 m_3}(k_1, k_2, k_3) = 8 i^{l_1+l_2+l_3} \int r^2 \mathrm{d}r\, j_{l_1}(k_1 r) j_{l_2}(k_2 r) j_{l_3}(k_3 r) \int d^2\hat{\boldsymbol{r}} Y^*_{l_1,m_1}(\hat{\boldsymbol{r}}) Y^*_{l_2,m_2}(\hat{\boldsymbol{r}}) Y^*_{l_3,m_3}(\hat{\boldsymbol{r}}) \,. \tag{5.53}$$

where the second integral is the Gaunt factor (Eq. 5.43). Here we instead derive the identity (see derivation in Appendix 5.C)

$$\begin{aligned} I^{l_1 l_2 l_3}_{m_1 m_2 m_3}(k_1, k_2, k_3) &= \frac{4\pi^{\frac{3}{2}}}{k_1 k_2 k_3} \sqrt{2l_1 + 1} \begin{pmatrix} l_1 & l_2 & l_3 \\ m_1 & m_2 & m_3 \end{pmatrix} \\ &\quad \times \sum_{|m| \le \min(l_2, l_3)} Y_{l_2,m}(\theta_{12}, 0) Y_{l_3,-m}(\theta_{13}, 0)\, (-1)^m \begin{pmatrix} l_1 & l_2 & l_3 \\ 0 & m & -m \end{pmatrix} , \end{aligned} \tag{5.54}$$

which allows us to rapidly compute the angle-averaged bispectrum without any numerical integration[2]

$$\begin{aligned} B^{\text{SFB, iso/homo}}_{l_1 l_2 l_3}(k_1, k_2, k_3) &= B_m(k_1, k_2, k_3) i^{l_1+l_2+l_3} \sqrt{2(2l_1 + 1)} \\ &\quad \times \sum_{|m| \le \min(l_2, l_3)} Y_{l_2,m}(\theta_{12}, 0) Y_{l_3,-m}(\theta_{13}, 0)(-1)^m \begin{pmatrix} l_1 & l_2 & l_3 \\ 0 & m & -m \end{pmatrix} . \end{aligned} \tag{5.55}$$

Above we define θ_{ij} as the angle between $\boldsymbol{k}_i$ and $\boldsymbol{k}_j$, such that $\cos(\theta_{12}) \equiv \hat{\boldsymbol{k}}_1 \cdot \hat{\boldsymbol{k}}_2 = \vartheta(k_1, k_2, k_3)$, where $\vartheta(k_1, k_2, k_3) \equiv \frac{k_3^2 - k_1^2 - k_2^2}{2k_1 k_2}$, and $\cos(\theta_{13}) \equiv \vartheta(k_1, k_3, k_2)$. Furthermore, denoting the spherical coordinates of $\hat{\boldsymbol{r}}$ by (θ, ϕ), we define $Y_{\ell,m}(\hat{\boldsymbol{r}}) \equiv Y_{\ell,m}(\theta, \phi)$. It is clear from Eq. 5.55 that the SFB bispectrum in an isotropic and homogeneous Universe is proportional to the Fourier bispectrum by a geometric coupling factor depending on the l_i and the angles between the $\boldsymbol{k}_i$. This factor also imposes the triangle inequality on the wavenumbers, i.e., $k_i \le |k_j - k_k|$, which is relaxed as we shall see in the next section for the observed SFB bispectrum and is only imposed approximately for spherically symmetric surveys which extend to sufficiently large redshifts.

The identity Eq. 5.54 is one of our key results. In addition to trivializing the computation of the signal in a homogeneous and isotropic Universe, it provides analytic insight into the geometric features of the observed bispectrum. Crucially, we will employ this identity to render the computation of the observed bispectrum tractable. We will discuss these points in 5.4.

[2] For this purpose we precompute a lookup table of $Y_{lm}(\theta, 0)$ values and interpolate. Also note that we may halve the number of terms in the sum by using its invariance under $m \to -m$.

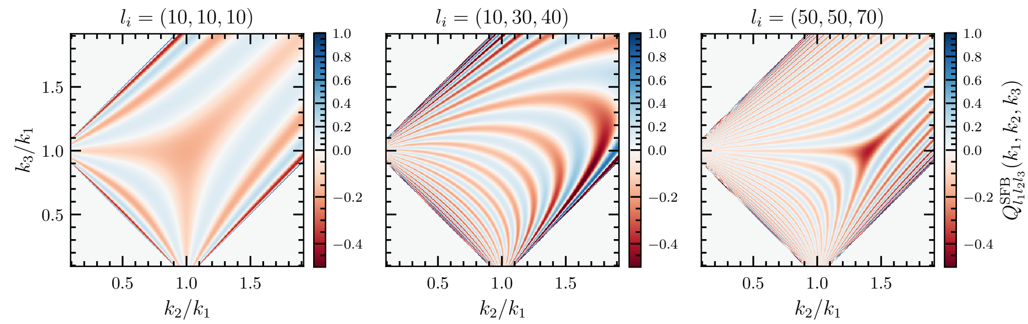

Figure 5.2: The reduced SFB bispectrum signal for an isotropic and homogeneous Universe, as a function of k_2 and k_3 in units of k_1, which is fixed to $k_1 = 4.18 \times 10^{-2}$ $h\mathrm{Mpc}^{-1}$ here. Each panel displays a different triplet $l_i \equiv (l_1, l_2, l_3)$. The bispectrum vanishes identically for configurations (k_1, k_2, k_3) which do not satisfy the triangle condition. The oscillations are a result of the geometric coupling in Eq. 5.56; their number is controlled by the values of l. Note that the colorbar limits are saturated in each panel.

Properties of the signal

In Fig. 5.2, we show two-dimensional cross-sections of the reduced bispectrum in an isotropic and homogeneous Universe as a function of k_2/k_1 and k_3/k_1 for fixed k_1, for three l-triplets (l_1, l_2, l_3). The most striking feature is the rectangular border outside of which the signal vanishes; this is the enforcement of the triangle inequality.

Another important feature is that the signal oscillates in the space of k_i's, which is not surprising, given that the products of spherical harmonics in $I^{l_1 l_2 l_3}_{m_1 m_2 m_3}(k_1, k_2, k_3)$,

$$Y_{l_2,m}(\theta_{12}, 0) Y_{l_3,-m}(\theta_{13}, 0)\,, \tag{5.56}$$

oscillate as the angles between the $\boldsymbol{k}_i$'s vary. Further, the number of oscillations as one moves from the center of the plot corresponding to an equilateral k-triangle, toward the borders of the rectangular region, corresponding to degenerate triangles, is higher for larger l_i values.

We also show a one-dimensional cross section in Fig. 5.3, taking the diagonal $k_2 = k_3$, for two different equilateral l shapes ($l_1 = l_2 = l_3 = l$). Perhaps the most important feature to note in this plot is that the SFB bispectrum effectively reduces to the matter bispectrum at the limit $k_2 = k_3 \gg k_1$ in the homogeneous and isotropic Universe. In this limit, we have $\cos(\theta_{12}) = \cos(\theta_{13}) \to 0$ and $B^{\mathrm{iso/homo}}_{l_1 l_2 l_3}(k_1, k_2, k_3)$ reduces to $C_{l_1 l_2 l_3} B_m(k_1, k_2, k_3)$ for a prefactor $C_{l_1 l_2 l_3}$, which quickly tends towards a constant as l grows.

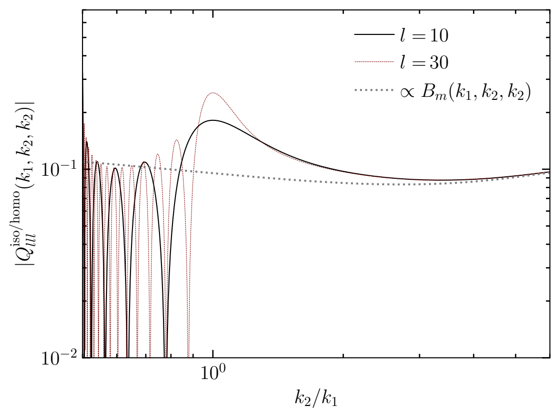

Figure 5.3: The reduced bispectrum signal in an isotropic and homogeneous Universe for fixed $k_1 = 4.18\times10^{-2}\ h\mathrm{Mpc}^{-1}$ as in Fig. 5.2, but now taking a cross-section along the diagonal $k_2 = k_3$. We show two equilateral l-triplets $l_1 = l_2 = l_3 = l$ with $l = 10$ and 30. The plot is cut at $k_2/k_1 = 0.5$ on the left since there is no signal below it where the triangle condition is violated (this property does not hold for the observed bispectrum in a realistic Universe, however). At high k_2, the SFB bispectrum is proportional to the Fourier-space bispectrum.

Similarly, in the limit of degenerate triangles e.g. $k_3 = k_2 + k_1$, we have $\cos(\theta_{12}) = \cos(\theta_{13}) = 1$, such that only the $m = 0$ term in Eq. 5.55 is nonzero, and the bispectrum reduces to

$$B_{l_1 l_2 l_3}^{\mathrm{SFB,\ iso/homo}}(k_1, k_2, k_3) = B_m(k_1, k_2, k_3) i^{l_1+l_2+l_3} \sqrt{2(2l_1+1)} \begin{pmatrix} l_1 & l_2 & l_3 \\ 0 & 0 & 0 \end{pmatrix}, \tag{5.57}$$

where again we have that the cosmological signal and the geometric coupling separate into a k-dependent and an l-dependent piece.

Requirement on the sampling frequency for resolving the oscillations

As we will see in the next section, the observed SFB bispectrum signal has a similar oscillation pattern in the space of k's as in the isotropic and homogeneous limit. With the analytic formula Eq. 5.55 at hand, we can easily estimate the local frequency of oscillations in k-space, and thus the minimum sampling of k_i's required to resolve these oscillations, assuming that the computation is performed on a uniform cubic grid of (k_1, k_2, k_3) with spacing Δk.

For example, consider for a given k_1, the oscillations along the diagonal $k_2 = k_3$, as are visible in Fig. 5.3. Estimating the frequency of the oscillations amounts to estimating the spacing between the roots of the associated Legendre polynomials in the products of Y_{lm}'s in Eq. 5.56. On the diagonal, the lowest point for which the signal is nonzero corresponds to the degenerate isosceles triangle $k_2 = k_3 = k_1/2$, and the diagonal extends to the top right into a squeezed triangle where $k_2, k_3 \gg k_1$. On this trajectory, θ_{12} and θ_{13} vary from 0 to $\pi/2$. The associated Legendre polynomial $P_m^l(\cos(\theta))$ has $l - |m|$ roots on the range $0 < \theta < \pi$, which are symmetric about $\pi/2$, so there are $(l - |m|)/2$ roots on the ranges we consider.

Consequently, the product of $Y_{l_2 m} Y_{l_3 m}$ crosses zero at most $(l_2 + l_3 - 2|m|)/2$ times[3]. The $m = 0$ term has the highest number of roots and may be used to estimate an upper bound on the spacing of roots. Towards that purpose, note that $P_l^0(\cos(\theta))$ is simply the Legendre polynomial $\mathcal{L}_l(\cos(\theta))$. Let $\theta_1, \ldots, \theta_l$ be the sequence of roots of $\mathcal{L}_l(\cos(\theta))$ in the interval $(0, \pi)$, listed in increasing order. Then we have the inequalities on the location of the roots [176]

$$\frac{\nu - \frac{1}{2}}{l}\pi < \theta_\nu < \frac{\nu}{l+1}\pi \quad (\nu = 1, 2, \cdots, \lceil l/2 \rceil) . \tag{5.58}$$

Hence, the first value of k_2 above $k_{2,\mathrm{min}} = k_1/2$ for which the spherical harmonic product of index $m = 0$ vanishes along the diagonal satisfies

$$k_2^{\mathrm{root}\,\nu=1} < \frac{k_1}{2\cos(\pi/(l_3+1))} . \tag{5.59}$$

Thus, to have at least N sampling points per oscillation, the sampling Δk must satisfy

$$N\Delta k < k_2^{\mathrm{root}\,\nu=1} - k_{2,\mathrm{min}} < k_1 \left[\frac{1}{2\cos(\frac{\pi}{l_3+1})} - \frac{1}{2} \right] \xrightarrow{l_3 \gg \pi} \frac{k_1}{4} \left(\frac{\pi}{l_3} \right)^2 . \tag{5.60}$$

We have verified numerically that the estimated l_3^{-2} scaling holds for bispectrum signal. Given the cost of computing the observed bispectrum, this means that resolving the oscillations of the signal within the triangle inequality region is challenging at high l.

In Section 5.4, we shall see that one property of the observed bispectrum signal is that for large enough l it is "Limber-suppressed" at low-k, in particular inside the region where the triangle inequality is satisfied. This means that we actually do not need to resolve the signal close to the borders of this region, where the local frequency of oscillations is higher, as the signal contains comparatively little information there.

[3] If $l_2 = l_3$, it crosses zero $\sim l_2/2$ times.

5.4 The observed SFB bispectrum

In this section, we begin by describing the template decomposition we use in order to render the computation of the observed SFB bispectrum feasible. We then give details of the signal computation before studying its properties.

Note that we now incorporate redshift evolution, RSD effects, PNG and survey window effects. Statistical homogeneity is now broken by the growth of structure and RSD[4], and the latter also breaks intrinsic isotropy. We restrict ourselves to the linear regime $k \lesssim 0.1\,h\mathrm{Mpc}^{-1}$ for which the tree-level bispectrum remains valid down to $z = 0$, and therefore do not include Fingers-of-God effects. We also choose to not model the monopole and dipole here, as they are affected by observer terms in GR such as the observer potential and peculiar velocity [166], i.e. we restrict ourselves to multipoles $l_i \geq 2$.

Template decomposition of the observed bispectrum

We begin by expressing the observed galaxy density field by applying the window function to the galaxy density field in redshift space,

$$\delta^{g,\mathrm{obs}}(\boldsymbol{r}) = W(\boldsymbol{r}) \int \frac{\mathrm{d}^3\boldsymbol{q}}{(2\pi)^3}\, e^{i\boldsymbol{q}\cdot\boldsymbol{r}} \delta^g(\boldsymbol{q},\boldsymbol{r})\,. \tag{5.61}$$

To second order in the linear matter density field $\delta^{(1)}$, we have from Eq. 5.21 that $\delta^{g,\mathrm{obs}}(\boldsymbol{r}) = \delta^{g,\mathrm{obs},(1)}(\boldsymbol{r}) + \delta^{g,\mathrm{obs},(2)}(\boldsymbol{r})$, where

$$\delta^{g,\mathrm{obs},(1)}(\boldsymbol{r}) = W(\boldsymbol{r}) \int \frac{\mathrm{d}^3\boldsymbol{q}}{(2\pi)^3}\, e^{i\boldsymbol{q}\cdot\boldsymbol{r}}\, D(r)\, Z_1(\boldsymbol{q},\boldsymbol{r})\, \delta^{(1)}(\boldsymbol{q})\,, \tag{5.62}$$

$$\begin{aligned}\delta^{g,\mathrm{obs},(2)}(\boldsymbol{r}) = W(\boldsymbol{r}) &\int \frac{\mathrm{d}^3\boldsymbol{q}}{(2\pi)^3}\, e^{i\boldsymbol{q}\cdot\boldsymbol{r}}\, D^2(r) \\ &\times \int \frac{1}{(2\pi)^3} \mathrm{d}^3\boldsymbol{k}_1\, \mathrm{d}^3\boldsymbol{k}_2\, Z_2(\boldsymbol{k}_1,\boldsymbol{k}_2,\boldsymbol{r})\, \delta^{(1)}(\boldsymbol{k}_1)\delta^{(1)}(\boldsymbol{k}_2)\, \delta_D(\boldsymbol{k}_1+\boldsymbol{k}_2-\boldsymbol{q})\,.\end{aligned} \tag{5.63}$$

Transforming the linear density contrast Eq. (5.62) into SFB space, we retrieve Eq. (5.10) where the kernel $\mathcal{W}_{\ell m}^{LM}(k,q)$ encodes (linear) galaxy physics and RSD. We aim to derive a similar relation for the second-order density contrast. We now transform Eq. 5.63 into SFB space using Eq. 5.1. Expressing the linear matter density contrast in the SFB basis from Eq. 5.4, and writing the Dirac-delta as an

[4]Note that in Fourier space, one can still assume statistical homogeneity by restricting to a given redshift bin and choosing an effective redshift for the entire bin.

integral over complex exponentials, we obtain

$$\delta^{g,(2)}_{\ell m}(k) = \sqrt{\frac{2}{\pi}}\, k \int \mathrm{d}^3\boldsymbol{r}\, j_\ell(kr)\, Y^*_{\ell m}(\hat{\boldsymbol{r}})\, W(\boldsymbol{r})\, D^2(r) \int \mathrm{d}^3\boldsymbol{q}\, e^{i\boldsymbol{q}\cdot\boldsymbol{r}} \int \frac{\mathrm{d}^3\boldsymbol{k}_1}{(2\pi)^3} \int \frac{\mathrm{d}^3\boldsymbol{k}_2}{(2\pi)^3}\, Z_2(\boldsymbol{k}_1,\boldsymbol{k}_2,\boldsymbol{r})$$
$$\times \int \mathrm{d}^3\boldsymbol{x}\, e^{i\boldsymbol{k}_1\cdot\boldsymbol{x}}\, e^{i\boldsymbol{k}_2\cdot\boldsymbol{x}}\, e^{-i\boldsymbol{q}\cdot\boldsymbol{x}} \frac{1}{k_1} \sum_{L_1 M_1} i^{-L_1}\, Y_{L_1 M_1}(\hat{\boldsymbol{k}}_1)\, \delta^{(1)}_{L_1 M_1}(k_1) \frac{1}{k_2} \sum_{L_2 M_2} i^{-L_2}\, Y_{L_2 M_2}(\hat{\boldsymbol{k}}_2)\, \delta^{(1)}_{L_2 M_2}(k_2)\,. \tag{5.64}$$

Naively inserting the expression for Z_2 (Eq. 5.28) into Eq. 5.64 would require evaluating high-dimensional angular integrals, which is intractable. To simplify the calculation, we remark that $Z_2(\boldsymbol{k}_1,\boldsymbol{k}_2,\boldsymbol{r})$ is nearly a polynomial in $\hat{\boldsymbol{k}}_1\cdot\hat{\boldsymbol{k}}_2$, $\hat{\boldsymbol{k}}_1\cdot\hat{\boldsymbol{r}}$, and $\hat{\boldsymbol{k}}_2\cdot\hat{\boldsymbol{r}}$. Indeed, defining $\tilde{Z}_2$ such that

$$Z_2(\boldsymbol{k}_1,\boldsymbol{k}_2,\boldsymbol{r}) = \tilde{Z}_2(\boldsymbol{k}_1,\boldsymbol{k}_2,\boldsymbol{r}) + f_{\mathrm{NL}} \frac{\alpha(k)}{\alpha(k_1)\,\alpha(k_2)} \left(b^{\mathrm{E}}_{10} + f(r)\mu^2\right) + f(r)\mu^2 G_2(\boldsymbol{k}_1,\boldsymbol{k}_2)\,, \tag{5.65}$$

we can decompose $\tilde{Z}_2$ into Legendre polynomials in those three variables and thereby factorize the dependence on the $\hat{\boldsymbol{k}}_i$ and $\hat{\boldsymbol{r}}$:

$$\tilde{Z}_2(\boldsymbol{k}_1,\boldsymbol{k}_2,\boldsymbol{r}) = \sum_{l_1 l_2 l_3} Z_{l_1 l_2 l_3}(k_1,k_2,r)\, \mathcal{L}_{l_1}(\hat{\boldsymbol{k}}_1\cdot\hat{\boldsymbol{k}}_2)\, \mathcal{L}_{l_2}(\hat{\boldsymbol{k}}_1\cdot\hat{\boldsymbol{r}})\, \mathcal{L}_{l_3}(\hat{\boldsymbol{k}}_2\cdot\hat{\boldsymbol{r}})\,. \tag{5.66}$$

Importantly, the sum over l_1, l_2, l_3 is finite, and indexed by 9 triplets (l_1, l_2, l_3) whose corresponding coefficients $Z_{l_1 l_2 l_3}$ are listed in Section 5.D. As we discuss below, the above Legendre decomposition permits to reduce the bispectrum to a triple integral.

Two other terms remain. The term proportional to f_{NL} in Eq. 5.65 depends on $k = |\boldsymbol{k}_1 + \boldsymbol{k}_2|$ through $\alpha(k)$, so it cannot be decomposed it in a similar fashion. In principle, the term proportional to $G_2(\boldsymbol{k}_1,\boldsymbol{k}_2)$ in Eq. 5.65 can be decomposed in this manner; however, since $\mu^2 = (\boldsymbol{k}_1\cdot\hat{\boldsymbol{r}} + \boldsymbol{k}_2\cdot\hat{\boldsymbol{r}})/(k_1^2 + k_2^2 + 2\boldsymbol{k}_1\cdot\boldsymbol{k}_2)$ it would render the sum Eq. 5.66 infinite and slowly-converging. Hence, we choose to treat the G_2 and f_{NL} terms separately (and exactly), as described in Section 5.D.

We summarize the remainder of the derivation here, leaving details to Appendix 5.D. First, we insert the decomposition Eq. 5.66 of $\tilde{Z}_2(\boldsymbol{k}_1,\boldsymbol{k}_2,\boldsymbol{r})$ into Eq. 5.64, and use the plane-wave expansion Eq. A.15 to decompose the complex exponentials into spherical harmonics and spherical Bessel functions. We rid of the angular integrals over $\hat{\boldsymbol{q}}$ with the orthogonality relation for spherical harmonics Eq. A.10.

Then we apply Wick's theorem to compute $\left\langle \delta^{g,(2)}_{\ell m}(k)\, \delta^{g,(1)}_{\ell' m'}(k')\, \delta^{g,(1)}_{\ell'' m''}(k'') \right\rangle$ in terms of the two-point functions. Finally, proceeding under the assumption of a spherically symmetric window $W(\boldsymbol{r}) = W(r)$, we compute the angle averaged bispectrum using Eq. 5.45 and obtain

$$B^{\mathrm{SFB}}_{l_1 l_2 l_3}(k_1,k_2,k_3) = 2\int \mathrm{d}q_2\, \mathcal{W}_{l_2}(k_2,q_2)\, P(q_2) \int \mathrm{d}q_3\, \mathcal{W}_{l_3}(k_3,q_3)\, P(q_3)\, \mathcal{V}^{l_1 l_2 l_3}_{\mathrm{tot.}}(k_1,q_2,q_3) \\ +\ 2 \text{ cyc. perm.} \tag{5.67}$$

where

$$\mathcal{V}^{l_1 l_2 l_3}_{\mathrm{tot.}}(k_1,q_2,q_3) \equiv \mathcal{V}^{l_1 l_2 l_3}(k_1,q_2,q_3) + \mathcal{V}^{l_1 l_2 l_3}_{f_{\mathrm{NL}},G_2}(k_1,q_2,q_3)\,, \tag{5.68}$$

where the specific forms of $\mathcal{V}^{l_1 l_2 l_3}$ and $\mathcal{V}^{l_1 l_2 l_3}_{f_{\mathrm{NL}},G_2}$ are given by Eqs. D.33 and D.45 respectively. Note that the kernel $\mathcal{W}_l(k,q)$ is already given by Eq. 5.17.

Let us briefly comment on the form of the dimensionless kernel Eq. 5.68. The first term of Eq. 5.68 is given by

$$\mathcal{V}^{\ell L_1 L_2}(k,k_1,k_2) \equiv (32\pi)^{\frac{3}{2}} k k_1 k_2 \sum_{l_1 l_2 l_3 L_3 L_4} g^{L_1 L_2 \ell}_{l_1 l_2 l_3 L_3 L_4} J^{\ell L_3 L_4}_{l_1 l_2 l_3}(k,k_1,k_2)\,, \tag{5.69}$$

where

$$J^{\ell L_3 L_4}_{l_1 l_2 l_3}(k,k_1,k_2) \equiv \int \mathrm{d}r\, r^2\, j_\ell(kr)\, j_{L_3}(k_1 r)\, j_{L_4}(k_2 r)\, W(r)\, D^2(r)\, Z_{l_1 l_2 l_3}(k_1,k_2,r)\,, \tag{5.70}$$

is the contribution to SFB mode coupling by cosmological sources (e.g. redshift evolution, RSD and PNG) and survey window, and where $g^{L_1 L_2 \ell}_{l_1 l_2 l_3 L_3 L_4}$ is a purely geometric mode coupling coefficient given by Eq. D.32.

In analogy to the SFB power spectrum, in which the matter power spectrum is convolved with kernels $\mathcal{W}_\ell(k,q)$ that describe the mode coupling through the product of two spherical Bessel functions, the kernel $\mathcal{V}^{l_1 l_2 l_3}(k_1,q_2,q_3)$ contains a product of three spherical Bessel functions. This endows the SFB bispectrum with key geometric features which we discuss shortly. The second term of Eq. 5.68, given by Eq. D.46, contains the contribution from the f_{NL} and G_2 terms and is of a similar form to Eq. 5.69. Our result matches the general form of the SFB bispectrum derived in Ref. [166].

Signal computation

We compute the bispectrum for a uniform grid of (k_1,k_2,k_3) of size 200^3 with k_i between $k_{\mathrm{min}} = 4\times10^{-3}\ h\mathrm{Mpc}^{-1}$ (note that future surveys like SPHEREx will be able to probe down to 10^{-3} $h\mathrm{Mpc}^{-1}$) and $k_{\max} = 8 \times 10^{-2}$ $h\mathrm{Mpc}^{-1}$ (to stay within linear regime) with uniform spacing $\Delta k = 3.8 \times 10^{-4}$ $h\mathrm{Mpc}^{-1}$. For the toy window function, we assume a sphere $W(\boldsymbol{r}) = \mathbf{1}_{[0,r_{\max}]}(r)$ with $r_{\max} = 5000\,\mathrm{Mpc}h^{-1}$, corresponding to a maximum redshift $z \sim 4.1$. As a result of the large redshift range chosen here, the kernels $\mathcal{W}_l(k,q)$ in Eq. 5.67 are highly peaked around $k \approx q$. For surveys with a smaller redshift extent $r_{\max}$, the kernel $\mathcal{W}_l(k,q)$ would have a smoother peak and lower frequency oscillations (as in Fig. 5.1), which would make the computation less computationally demanding.

Let us now examine more closely the form of the integrals to be computed. Note first that Eq. 5.67 is a two-dimensional integral (over q_2 and q_3) of the kernels $\mathcal{V}_{\mathrm{tot}}$. The first term in this kernel, $\mathcal{V}^{l_1l_2l_3}$ (Eq. D.30) is a sum of the one-dimensional Bessel integrals given in Eq. 5.70. The second term $\mathcal{V}^{l_1l_2l_3}_{f_{\mathrm{NL}},G_2}$ is also effectively a one-dimensional integral since the computationally-intensive parts of the integrand, the integrals $\mathcal{W}_l^{G_2}$, $\mathcal{W}_l^{f_{\mathrm{NL}}}$ and $I_{l_1l_2l_3}$, can be precomputed on a grid. The precomputation for $I_{l_1l_2l_3}$ requires a few seconds using the identity Eq. 5.54, which expresses it as a finite sum with l_3 terms.

Finally, the kernels $\mathcal{V}^{l_1l_2l_3}(k_1, q_2, q_3)$ themselves are precomputed on a q_2-q_3 grid to be reused for the various triplets (k_1, k_2, k_3). This, along with the final integration in Eq. 5.67, is the bottleneck of the calculation, and limits the number of l-triplets we may feasibly calculate. However, the signal is sufficiently smooth in l that this might not pose a problem for e.g., a Fisher forecast exercise. All grid computations are parallelized using Julia's multithreading functionality; computing the kernels $\mathcal{V}^{l_1l_2l_3}(k_1, q_2, q_3)$ requires a few hours per triplet (l_1, l_2, l_3) with multithreading across 256 AMD EPYC 7763 CPUs.

Beyond dimensionality, a second numerical concern is the oscillatory nature of the integrands. We perform all integrals via Gauss-Legendre quadrature. To accurately integrate $\mathcal{V}^{l_1l_2l_3}_{\mathrm{tot}}(k_1, q_2, q_3)$, we observe (empirically) that if the averaging r-spacing is Δr, then we must impose $k_1 + q_2 + q_3 \lesssim \pi/\Delta r$. We use $\Delta r = 5$ $\mathrm{Mpc}h^{-1}$. Further, to evaluate the bispectrum we must convolve the kernels $\mathcal{V}^{l_1l_2l_3}_{\mathrm{tot}}(k_1, q_2, q_3)$ with the $\mathcal{W}_{l_2}(k_2, q_2)$, both of which oscillate quickly as q_2 is varied. This requires a sufficient sampling in the q_i space. As the computation time is quadratic in the number of sampling points for each q_i, only modest samplings are feasible; we use 300 points for each q_i, chosen as Gauss-Legendre nodes.

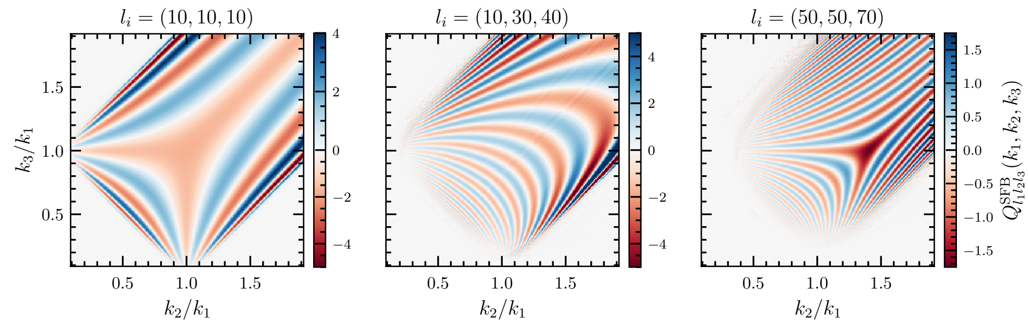

Figure 5.4: The observed reduced SFB bispectrum for a realistic Universe, assuming a spherically symmetric survey window, for the same set of l-triplets as in Fig. 5.2. The signal is sampled at 200^2 pairs (k_2, k_3) in each panel, whereas in Fig. 5.2 there are 400^2 sampled pairs.

Properties of the signal

The observed bispectrum signal displays a number of salient features which we now discuss.

Oscillations in k and mode coupling

A cross-section of the reduced bispectrum for fixed $k_1 = 0.0418\,h\text{Mpc}^{-1}$, for the same set of l-triplets as in Fig. 5.2, is shown in Fig. 5.4. Perhaps the most striking feature here is that the patterns of oscillations in k-space are similar to those visible in Fig. 5.2 for the isotropic and homogeneous case. We may understand this from the mode coupling coefficients $g^{L_1 L_2 \ell}_{l_1 l_2 l_3 L_3 L_4}$ in Eq. 5.69. Numerically we find that they are generally suppressed unless $(L_3, L_4) = (L_1, L_2)$, such that the dominant contribution to the bispectrum signal $B^{\rm SFB}_{l_1 l_2 l_3}$ is from integrals of type Eq. 5.70 where the spherical Bessel functions have the same indices l_1, l_2, l_3, as in the isotropic and homogeneous case (Eq. 5.51 – 5.53).

Limber suppression at low k and high l

In Fig. 5.5, we increase the l values to $l_1 = l_2 = l_3 = 90$, and see that the overall amplitude of the oscillations decreases by roughly an order of magnitude relative to the leftmost panel of Fig. 5.4. To understand the suppression with increasing l, which is generic, we note that for fixed r, the spherical Bessel function $j_l(kr)$ is proportional to $(kr)^l$ for small k; for large k, it oscillates with an amplitude proportional to $(kr)^{-1}$. Further, in the Limber approximation[5] (Eq. A.5), for a fixed

[5] Calling this the *Limber approximation* is standard in cosmology. However, the term is slightly misleading, since the original approximation by Limber [177] was in configuration space, and only

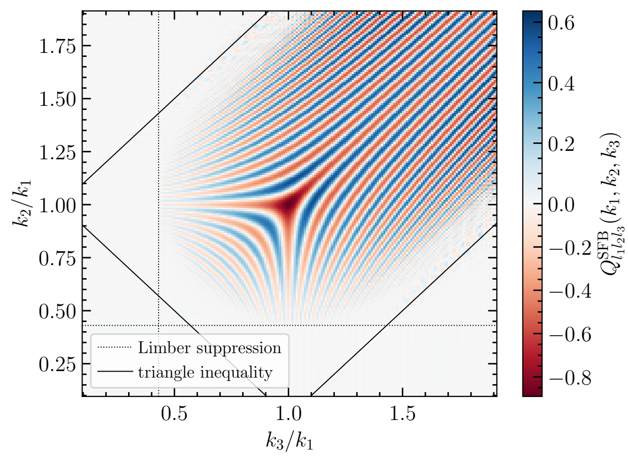

Figure 5.5: A illustration of the Limber suppression at low k, which becomes visible for the reduced observed SFB bispectrum signal within the triangle inequality region for sufficiently large l. Here we show the signal for $l_1 = l_2 = l_3 = 90$, while still fixing $k_1 = 4.18 \times 10^{-2}\, h\mathrm{Mpc}^{-1}$. The onset of Limber suppression is indicated by the gray dashed lines, where we expect the signal to be suppressed according to the Limber approximation $k_i = (l_i + \frac{1}{2})/r_{\mathrm{max}}$. The border of the region where the triangle inequality on (k_1, k_2, k_3) holds is shown by the solid lines.

l and k, the Bessel function $j_l(kr)$ is peaked around $r \sim (l + \frac{1}{2})/k$ with a peak value equal to $\sim \sqrt{\pi/(2l)}$ [179].

Physically, we may understand the suppression as follows. For fixed (k_1, k_2, k_3), the bispectrum at higher l_i probes higher redshifts. If the survey window has finite radial extent, these higher redshift contributions to the signal are necessarily smaller, and vanish once the redshift exceeds the extent of the survey. By contrast, when the survey window has infinite size as in the homogeneous and isotropic Universe, for every l_i there is a corresponding redshift which contributes non-negligibly to the signal, such that there is no such suppression at high l_i.

Given that the spherical Bessel functions go as $(kr)^l$ when $k \lesssim l/r$, we should also expect a sharp suppression of the bispectrum at low k. This suppression is not visible in the first panel of Fig. 5.4 because this effect is only relevant for $l \gtrsim k_{\mathrm{min}} r_{\mathrm{max}} = 20$ in our fiducial setup. On the other hand it visible in Fig. 5.5, for $l_1 = l_2 = l_3 = 90$. The onset of the low k suppression is inside of the region where the triangle inequality holds, and is indicated by the dotted gray lines.

Recall from the previous sections that the frequency of the oscillations increases

applied to Fourier-space by Kaiser [178]. The resulting approximation effectively is that of Eq. A.5 [179].

as we approach the triangle inequality boundary, making the computation increasingly difficult close to the boundary with higher sampling needed to resolve these oscillations. For small l, we have large spacings $\Delta k \propto l^{-2}$ which are manageable. For large l, the Limber suppression is helpful in the sense that it is not necessary to compute the signal at the boundary since it is suppressed there by several orders of magnitude. This is true both in a Fisher analysis or in a real data analysis where we can simply choose to ignore this part of the data vector as it contains almost no information.

Violation of the triangle condition

We saw that in an isotropic and homogeneous Universe, the bispectrum signal vanishes identically when (k_1, k_2, k_3) does not satisfy the triangle inequality. This is a consequence of (intrinsic) isotropy. In the case of the observed bispectrum, where this isotropy is broken by e.g., redshift space distortions, this is no longer true, though it holds approximately for wider survey windows. For lower values of $r_{\max}$, the signal strength is non-negligible even when (k_1, k_2, k_3) violate the triangle inequality.

This is due to two reasons. First, the kernels $\mathcal{W}_l(k, q)$ (Eq. 5.17) are less peaked for smaller $r_{\max}$, such that for (k_1, k_2, k_3) which violate the triangle inequality, the integral Eq. 5.67 can pick up a non-negligible contribution from the kernel $\mathcal{V}^{l_1 l_2 l_3}_{\text{tot}}(k_1, q_2, q_3)$ for (k_1, q_2, q_3) which do form a triangle. Secondly, for smaller $r_{\max}$, $\mathcal{V}^{l_1 l_2 l_3}_{\text{tot}}(k_1, q_2, q_3)$ itself can take non-negligible values for (k_1, q_2, q_3) which do not form a triangle (indeed, the Bessel integrals Eq. 5.70 do not come with any triangle condition). As a result, the triangle inequality is broken in the observed SFB bispectrum, with the violation more severe at lower $r_{\max}$. See Fig. 5.6, which illustrates this effect using $r_{\max} = 500, 1000$ and $2500\ \mathrm{Mpc}h^{-1}$.

5.5 Discussion

In this chapter, we computed the SFB bispectrum signal for the first time, discussing how to account for redshift space distortions and primordial non-Gaussianity. Starting with a toy example of the homogeneous and isotropic Universe, we built up intuition for later understanding some key features of the observed bispectrum convolved with a toy spherically symmetric window.

To render the computation tractable, we leveraged a decomposition of the second-order redshift space kernel into products of three Legendre polynomials, which

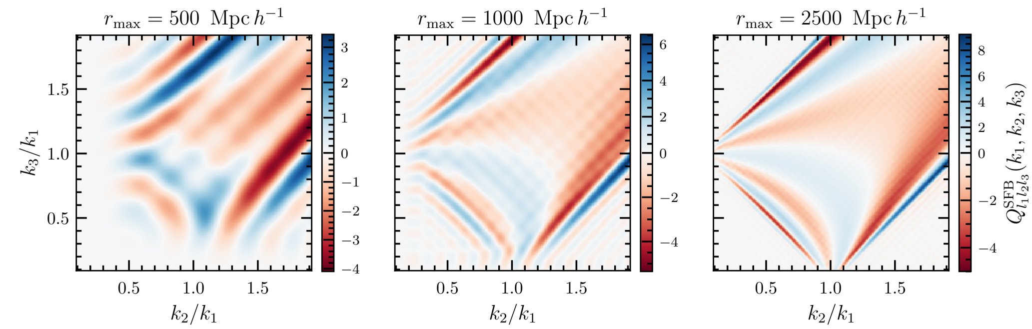

Figure 5.6: A demonstration of the triangle condition violation in a realistic Universe — the observed reduced bispectrum signal for different values of the redshift extent $r_{\max} = 500, 1000$ and $2500\,\mathrm{Mpc}h^{-1}$ (corresponding to $z \sim 0.18$, 0.37 and 1.2 respectively) at fixed $k_1 = 4.18 \times 10^{-2}\ h\mathrm{Mpc}^{-1}$ and $(l_1, l_2, l_3) = (4, 6, 8)$. For smaller $r_{\max}$, the violation of the triangle condition is more severe due to less peaked $\mathcal{W}_l$ kernels (see Section 5.4 for more explanations).

allowed us to express the bispectrum, modulo RSD and PNG terms, as a triple integral. Furthermore, we derived an identity to express as a simple sum the 6-dimensional angular integral of three spherical harmonics (or equivalently, the one-dimensional integral of a product of three spherical Bessel functions on an infinite interval). This enabled us to rapidly compute and study the signal in the case of a homogeneous and isotropic Universe, and to accelerate the calculation of the RSD and PNG contributions to the observed bispectrum.

Even with these techniques and the various numerical optimizations we employed, computing the SFB bispectrum is clearly expensive: for each triplet of multipole indices (l_1, l_2, l_3) and of wavenumbers (k_1, k_2, k_3), we need to evaluate triple integrals with oscillatory integrands. Our method requires $\mathcal{O}(100)$ CPU hours for each l-triplet to compute the signal on a grid of 200^3 (k_1, k_2, k_3) triplets. In a realistic data analysis, one would need to calculate the signal for different cosmologies in a Monte-Carlo Markov Chain (MCMC) on the order of seconds. We note however that we have chosen a very large redshift extent $z \lesssim 4$, corresponding to $r_{\max} = 5000\,\mathrm{Mpc}h^{-1}$, for which the integration is the most challenging. Surveys with smaller redshift extent would require less time for computation.

There are several possibilities to accelerate and improve the accuracy of the computation that we leave for future work. For example, as the local frequency of the oscillations in the signal can be estimated as a function of (k_i, l_i) from the isotropic and homogeneous bispectrum as in Section 5.3, the signal can instead be sampled on a suitable non-uniform grid of (k_1, k_2, k_3). To improve upon the Gauss-Legendre quadrature method for integrating the spherical Bessel product Eq. 5.70, the 3-dimensional generalization of the FFTLog method of [180] could prove superior. Leveraging cache-friendly memory layouts may also help to speed up some of the linear algebra operations involved in computing these Bessel integrals on a grid in k-space.

For the purpose of calculations in a MCMC analysis, one could also explore decomposing the bispectrum dependence on cosmological parameters into precomputed templates, and varying the coefficients of the template corresponding to the varying cosmology. If it becomes impossible to directly compute the signal for each point in the cosmology parameter space sampled during the MCMC, the use of emulators could also aid in minimizing the evaluation time.

Another natural extension to this chapter is to incorporate more physical and observational effects in the computation. The most important physical effects on large-scales that we have not included here are general-relativistic (GR) effects. The authors of Ref. [166] detailed how to incorporate them in the SFB bispectrum; in principle they may be evaluated numerically within the same framework described here, i.e. through (many) additional terms in the first order kernels $\mathcal{W}_l(k, q)$ and in the second-order kernels $\mathcal{V}^{l_1 l_2 l_3}$, after a template decomposition into Legendre polynomials as in Section 5.4. On smaller scales, more detailed modeling of RSD (e.g. Fingers-of-God and Alcock-Paczynski effects) and of the nonlinear regime would be needed. In addition, we have used a spherically symmetric window function to demonstrate the calculation, while realistic window convolution is still to be explored.

To feasibly use the SFB bispectrum to analyze survey data, a number of missing pieces would still need to be filled in. In particular, it would be necessary to develop an efficient SFB bispectrum estimator, e.g., by building off of techniques developed by [154, 157] for an SFB power spectrum estimator. As allowing for a survey window of arbitrary geometry in the modeling of the signal would greatly increase the computational cost, one may explore accounting for it in the estimator, e.g., by using a windowless estimator which directly returns the window-deconvolved bispectrum as pioneered in Ref. [181] for the bispectrum multipoles.

Moreover, a realistic covariance matrix for the SFB bispectrum beyond the Gaussian approximation also needs to be developed, including complexities due to window function convolution as well as non-Gaussian covariance. If the window effects can be reliably removed at the estimator level, then the covariance would be significantly simplified. For the non-Gaussian covariance, an approximation similar in form to that proposed in Ref. [182] may be applicable for the SFB bispectrum, where the non-Gaussian part of the covariance is dominated by the product of two bispectra sharing the same large scale — a good approximation for squeezed configurations and also tested to be good enough for other configurations in Ref. [182] in the context of Fourier-space bispectrum. Alternatively, to incorporate all complexities at once, one may also develop mocks to compute the mock-based covariance by averaging over many realizations, once a fast SFB bispectrum estimator exists. This method would include wide-angle effects directly for mocks with large enough angular area, while it could be challenging to incorporate all GR effects into the mocks.

Since an advantage of the SFB formalism is that it avoids the loss of information due to assuming inexact lines-of-sights for individual galaxy triplets, it would also be interesting to evaluate more quantitatively now this information gain, for example by comparing to the standard bispectrum multipole formalism in the local plane-parallel approximation and to perturbative corrections thereof as in [146]. Our work to enable the computation of the signal will allow for such a study to be conducted. With a suitable scheme to interpolate the signal in the space of multipoles l_i, it could be feasible to conduct a Fisher forecast for various cosmological parameters of interest, such as $f_{\rm NL}$ or RSD parameters.

Note that this loss of information may be small for surveys with small angular extent, but more important for full-sky surveys like SPHEREx. Currently, with the exception of the TSH formalism, only perturbative approaches to modeling wide-angle effects in the bispectrum have been proposed [146, 183], expanding from the global plane-parallel approximation. Thus, the SFB bispectrum remains the only method to fully account for all large scale effects non-perturbatively on the largest angular scales while preserving the potential of retaining all information contained in the radial modes.

Another advantage of the SFB formalism is that some of the GR terms, which are mostly radial effects along the line-of-sight, become easily disentangled from other effects. In particular, the monopole and the dipole terms in the SFB formalism contain all the observer terms in GR arising from the potential and velocity at the observer position. Some of these terms may be quantified via other means before being subtracted (e.g. the velocity term in the dipole), while others are intrinsically undetectable (e.g. observer potential) and may need to be modeled through constrained realization if they affect observables of interest.

Modeling these terms in a Cartesian framework amounts to propagating these effects to every mode (and every order if a perturbative expansion from the plane-parallel approximation is used), which would propagate potential systematics into every measured mode. In contrast, in a spherical framework such as SFB, there is a clear radial and angular separation that allows for the isolation of such terms into just the monopole and dipole, which may then be discarded or tested separately for systematics.

While the TSH formalism provides a similar advantage, it requires many radial bins required to resolve the large scale radial modes (which is important to do for measuring $f_{\rm NL}$), which introduces highly correlated neighboring radial bins, and leads to numerically instabilities during covariance inversion. The SFB method is therefore a trade-off between extracting the maximal amount of information and the cost of computing the signal. In this regard, we have made a step forward by rendering the SFB signal computable and studying its various features.

This is merely the beginning of more efforts to follow to make the calculation of the SFB bispectrum feasible for next-generation surveys. With increasing computational power in the future, along with more sophisticated numerical and mathematical techniques, the SFB bispectrum may become a key formalism that will allow us to extract all of the possible information from a full-sky galaxy survey.

5.A Useful formulae

Dirac delta distribution

For a continuously differentiable function g with simple roots $\{x_i\}$ we have

$$\delta_D(g(x)) = \sum_i \frac{\delta_D(x - x_i)}{|g'(x_i)|}\,. \tag{A.1}$$

For any function $f(\boldsymbol{k})$,

$$\int k^2 \mathrm{d}k\, \mathrm{d}^2\hat{\boldsymbol{k}}\, \delta^D(\boldsymbol{k} - \boldsymbol{k}')\, f(\boldsymbol{k}) = \int \mathrm{d}k\, \delta^D(k - k') \int \mathrm{d}^2\hat{\boldsymbol{k}}\, \delta^D(\hat{\boldsymbol{k}} - \hat{\boldsymbol{k}}')\, f(\boldsymbol{k})\,. \tag{A.2}$$

Therefore,

$$\delta^D(\boldsymbol{k} - \boldsymbol{k}') = k^{-2}\, \delta^D(k - k')\, \delta^D(\hat{\boldsymbol{k}} - \hat{\boldsymbol{k}}')\,. \tag{A.3}$$

Spherical Bessel functions

To first order the Bessel function $J_\nu(x)$ may be approximated by a Dirac delta as [179]

$$J_\nu(kr) \simeq \delta^D(kr-\nu) \ . \tag{A.4}$$

Therefore, for a spherical Bessel function $j_\ell(x) = \sqrt{\pi/2x}\, J_{\ell+\frac{1}{2}}(x)$ we have

$$j_\ell(kr) \simeq \sqrt{\frac{\pi}{2rk}}\, \delta^D\left(r - \frac{\ell+\frac{1}{2}}{k}\right) , \tag{A.5}$$

to first order. In the cosmology literature, a version of this is often called *Limber's approximation* [177]. Spherical Bessel functions satisfy the orthogonality relation

$$\delta^D(k-k') = \frac{2kk'}{\pi} \int_0^\infty \mathrm{d}r\, r^2\, j_\ell(kr)\, j_\ell(k'r) \, . \tag{A.6}$$

Spherical harmonics

Spherical harmonics can be expressed in terms of a complex exponential and real associated Legendre functions $\mathrm{P}_\ell^m(x)$ as

$$Y_{\ell m}(\hat{\boldsymbol{r}}) = e^{im\phi} \left(\frac{(\ell-m)!(2\ell+1)}{4\pi\,(\ell+m)!}\right)^{\frac{1}{2}} \mathrm{P}_\ell^m(\cos\theta) \, . \tag{A.7}$$

The associated Legendre functions are even or odd according to the index,

$$P_\ell^m(-x) = (-1)^{\ell+m} P_\ell^m(x) \, . \tag{A.8}$$

The completeness relation is

$$\sum_{\ell m} Y_{\ell m}(\hat{\boldsymbol{r}})\, Y^*_{\ell m}(\hat{\boldsymbol{r}}') = \delta^D(\hat{\boldsymbol{r}} - \hat{\boldsymbol{r}}') \, . \tag{A.9}$$

The spherical harmonics satisfy the orthogonality relation

$$\int \mathrm{d}\Omega_{\hat{\boldsymbol{r}}}\, Y_{\ell m}(\hat{\boldsymbol{r}})\, Y^*_{\ell' m'}(\hat{\boldsymbol{r}}) = \delta^K_{\ell\ell'} \delta^K_{mm'} \, . \tag{A.10}$$

For a rotation $\mathcal{R}$ about the origin that sends the unit vector $\mathbf{r}$ to $\mathbf{r}'$, we have

$$Y_{\ell,m}(\mathbf{r}') = \sum_{m'=-\ell}^{\ell} [D^{(\ell)}_{mm'}(\mathcal{R})]^* Y_{\ell,m'}(\mathbf{r}), \tag{A.11}$$

where $[D^{(\ell)}_{mm'}(\mathcal{R})]^*$ is the complex conjugate of an entry of the Wigner D-matrix. The Wigner D-matrix is a unitary square matrix of dimension $2j+1$. If $\mathcal{R}$ is defined by proper Euler angles α, β, γ in the z-y-z convention, we have the property

$$D^{\ell}_{m0}(\mathcal{R}) = \sqrt{\frac{4\pi}{2\ell+1}} Y^*_{\ell,m}(\beta, \alpha)\,, \tag{A.12}$$

and also the relation

$$D^{j}_{mk}(\mathcal{R}) D^{j'}_{m'k'}(\mathcal{R}) = \sum_{J=|j-j'|}^{j+j'} \langle j m j' m' | J\,(m+m')\rangle \langle j k j' k' | J\,(k+k')\rangle D^{J}_{(m+m')(k+k')}(\mathcal{R})\,, \tag{A.13}$$

where $\langle j_1 m_1 j_2 m_2 | j_3 m_3\rangle$ is a Clebsch-Gordan coefficient. The latter is related to the Wigner $3j$ symbols by

$$\langle j_1\, m_1\, j_2\, m_2 | J\, M\rangle = (-1)^{-j_1+j_2-M} \sqrt{2J+1} \begin{pmatrix} j_1 & j_2 & J \\ m_1 & m_2 & -M \end{pmatrix}. \tag{A.14}$$

We may also expand plane waves in terms of spherical Bessels and spherical harmonics,

$$e^{i\boldsymbol{q}\cdot\boldsymbol{r}} = 4\pi \sum_{\ell',m'} i^{\ell'} j_{\ell'}(qr)\, Y^*_{\ell'm'}(\hat{\boldsymbol{q}})\, Y_{\ell'm'}(\hat{\boldsymbol{r}})\,, \tag{A.15}$$

from which it follows, using Eq. A.10, that

$$\int \mathrm{d}^2\hat{\boldsymbol{r}} Y^*_{l,m}(\hat{\boldsymbol{r}}) e^{i\boldsymbol{q}\cdot\boldsymbol{r}} (\hat{\boldsymbol{q}}\cdot\hat{\boldsymbol{r}})^{\alpha} = 4\pi i^l Y^*_{l,m}(\hat{\boldsymbol{q}}) (-i\partial_{qr})^{\alpha} j_l(qr)\,. \tag{A.16}$$

The Legendre polynomials can be expressed as a sum over spherical harmonics as

$$\mathcal{L}_{\ell}(\hat{\boldsymbol{k}}\cdot\hat{\boldsymbol{r}}) = \frac{4\pi}{2\ell+1} \sum_m Y_{\ell m}(\hat{\boldsymbol{k}})\, Y^*_{\ell m}(\hat{\boldsymbol{r}})\,. \tag{A.17}$$

We also have the identities

$$Y^*_{\ell m}(\hat{\boldsymbol{r}}) = (-1)^m Y_{\ell,-m}(\hat{\boldsymbol{r}})\,, \tag{A.18}$$

$$Y_{\ell m}(-\hat{\boldsymbol{r}}) = (-1)^{\ell} Y_{\ell,m}(\hat{\boldsymbol{r}})\,. \tag{A.19}$$

Gaunt factor

The Gaunt factor is

$$\mathcal{G}^{\ell L L_1}_{m M M_1} \equiv \int \mathrm{d}^2\hat{\boldsymbol{r}}\, Y_{\ell m}(\hat{\boldsymbol{r}})\, Y_{LM}(\hat{\boldsymbol{r}})\, Y_{L_1 M_1}(\hat{\boldsymbol{r}})\,, \tag{A.20}$$

and it can be expressed in terms of Wigner-3j symbols,

$$\mathcal{G}^{\ell L L_1}_{mMM_1} = \left(\frac{(2\ell+1)(2L+1)(2L_1+1)}{4\pi}\right)^{\frac{1}{2}} \begin{pmatrix} \ell & L & L_1 \\ 0 & 0 & 0 \end{pmatrix} \begin{pmatrix} \ell & L & L_1 \\ m & M & M_1 \end{pmatrix} . \tag{A.21}$$

Hence, a product of two spherical harmonics can be reduced to a linear combination of spherical harmonics by

$$Y_{l_1 m_1}(\hat{\boldsymbol{r}}) Y_{l_2 m_2}(\hat{\boldsymbol{r}}) = \sum_L (-1)^M \mathcal{G}^{l_1 l_2 L}_{m_1 m_2 -M} Y_{LM}(\hat{\boldsymbol{r}}) , \tag{A.22}$$

where $M = m_1 + m_2$. Using this identity, one can derive by recursion the analogous integral to Eq. A.20 for any number of spherical harmonics. For four spherical harmonics we have (as in Appendix A of Ref. [184]):

$$\int \mathrm{d}^2\hat{\boldsymbol{r}}\, Y_{l_1 m_1}(\hat{\boldsymbol{r}}) Y_{l_2 m_2}(\hat{\boldsymbol{r}}) Y_{l_3 m_3}(\hat{\boldsymbol{r}}) Y_{l_4 m_4}(\hat{\boldsymbol{r}}) = \sum_L (-1)^M \mathcal{G}^{l_1 l_2 L}_{m_1 m_2 -M} \mathcal{G}^{L l_3 l_4}_{M m_3 m_4} . \tag{A.23}$$

Wigner symbols

The Wigner 3j symbols obey an orthogonality relation

$$\sum_{mM} \begin{pmatrix} \ell & L & L_1 \\ m & M & M_1 \end{pmatrix} \begin{pmatrix} \ell & L & L_2 \\ m & M & M_2 \end{pmatrix} = \frac{\delta^K_{L_1 L_2} \delta^K_{M_1 M_2} \delta^T(\ell, L, L_1)}{2L_1 + 1} , \tag{A.24}$$

where $\delta^T(\ell, L, L_1)$ enforces the triangle relation that is obeyed by the Wigner 3j-symbols, i.e. they vanish unless $|\ell - L| \le L_1 \le \ell + L$ and $m + M + M_1 = 0$.

The Wigner 3j's acquire a phase for $m_i \to -m_i$:

$$\begin{pmatrix} j_1 & j_2 & j_3 \\ -m_1 & -m_2 & -m_3 \end{pmatrix} = (-1)^{j_1+j_2+j_3} \begin{pmatrix} j_1 & j_2 & j_3 \\ m_1 & m_2 & m_3 \end{pmatrix} . \tag{A.25}$$

We also have the identity

$$\begin{pmatrix} j_1 & j_2 & j_3 \\ m_1 & m_2 & m_3 \end{pmatrix} \begin{Bmatrix} j_1 & j_2 & j_3 \\ l_1 & l_2 & l_3 \end{Bmatrix} = \sum_{m_1' m_2' m_3'} (-1)^{l_1+l_2+l_3+m_1'+m_2'+m_3'} \times \begin{pmatrix} j_1 & l_2 & l_3 \\ m_1 & m_2' & -m_3' \end{pmatrix} \begin{pmatrix} l_1 & j_2 & l_3 \\ -m_1' & m_2 & m_3' \end{pmatrix} \begin{pmatrix} l_1 & l_2 & j_3 \\ m_1' & -m_2' & m_3 \end{pmatrix} , \tag{A.26}$$

where a Wigner $6j$-symbol appears on the LHS. Lastly, we also have

$$\begin{pmatrix} j_{13} & j_{23} & j_{33} \\ m_{13} & m_{23} & m_{33} \end{pmatrix} \begin{Bmatrix} j_{11} & j_{12} & j_{13} \\ j_{21} & j_{22} & j_{23} \\ j_{31} & j_{32} & j_{33} \end{Bmatrix} = \sum_{m_{r1}, m_{r2}, r=1,2,3} \begin{pmatrix} j_{11} & j_{12} & j_{13} \\ m_{11} & m_{12} & m_{13} \end{pmatrix} \begin{pmatrix} j_{21} & j_{22} & j_{23} \\ m_{21} & m_{22} & m_{23} \end{pmatrix}$$
$$\times \begin{pmatrix} j_{31} & j_{32} & j_{33} \\ m_{31} & m_{32} & m_{33} \end{pmatrix} \begin{pmatrix} j_{11} & j_{21} & j_{31} \\ m_{11} & m_{21} & m_{31} \end{pmatrix} \begin{pmatrix} j_{12} & j_{22} & j_{32} \\ m_{12} & m_{22} & m_{32} \end{pmatrix}, \tag{A.27}$$

where a Wigner $9j$-symbol appears on the LHS.

5.B Encoding of observational isotropy by the Gaunt factor

Here we show that the 3-point function of the SFB modes of an observationally-isotropic real-valued field $\delta(\mathbf{r})$ is real and proportional to the Gaunt factor. To see this, note that in real space, the 3-point function of δ can only depend on the distances to each point and the angles on the sky. Therefore, we may expand it in Legendre polynomials as

$$\langle \delta(\boldsymbol{r}_1)\delta(\boldsymbol{r}_2)\delta(\boldsymbol{r}_3)\rangle = \sum_{L_1 L_2 L_3} f_{L_1 L_2 L_3}(r_1, r_2, r_3)\, \mathcal{L}_{L_1}(\hat{\boldsymbol{r}}_1 \cdot \hat{\boldsymbol{r}}_2)\, \mathcal{L}_{L_2}(\hat{\boldsymbol{r}}_2 \cdot \hat{\boldsymbol{r}}_3)\, \mathcal{L}_{L_3}(\hat{\boldsymbol{r}}_3 \cdot \hat{\boldsymbol{r}}_1)\,. \tag{B.1}$$

The Legendre polynomials may be further decomposed into sums over spherical harmonics via Eq. A.17. We may then transform Eq. B.1 to spherical harmonic space to obtain

$$\begin{aligned}
&\langle \delta_{\ell_1 m_1}(r_1)\delta_{\ell_2 m_2}(r_2)\delta_{\ell_3 m_3}(r_3)\rangle \\
&= \int d^2\hat{r}_1\, d^2\hat{r}_2\, d^2\hat{r}_3\, Y^*_{\ell_1 m_1}(\hat{\boldsymbol{r}}_1)\, Y^*_{\ell_2 m_2}(\hat{\boldsymbol{r}}_2)\, Y^*_{\ell_3 m_3}(\hat{\boldsymbol{r}}_3) \\
&\quad \times \sum_{L_1 L_2 L_3} A_{L_1 L_2 L_3}\, f_{L_1 L_2 L_3}(r_1, r_2, r_3) \sum_{M_1 M_2 M_3} (-1)^{M_1+M_2+M_3}\, Y^*_{L_1 -M_1}(\hat{\boldsymbol{r}}_1) Y^*_{L_1 M_1}(\hat{\boldsymbol{r}}_2) \\
&\quad \times Y^*_{L_2 -M_2}(\hat{\boldsymbol{r}}_2) Y^*_{L_2 M_2}(\hat{\boldsymbol{r}}_3)\, Y^*_{L_3 -M_3}(\hat{\boldsymbol{r}}_3) Y^*_{L_3 M_3}(\hat{\boldsymbol{r}}_1) \\
&= \sum_{L_1 L_2 L_3} A_{L_1 L_2 L_3}\, f_{L_1 L_2 L_3}(r_1, r_2, r_3) \sum_{M_1 M_2 M_3} (-1)^{M_1+M_2+M_3}\, \mathcal{G}^{\ell_1 L_1 L_3}_{m_1 -M_1 M_3}\, \mathcal{G}^{\ell_2 L_2 L_1}_{m_2 -M_2 M_1}\, \mathcal{G}^{\ell_3 L_3 L_2}_{m_3 -M_3 M_2}\,,
\end{aligned} \tag{B.2}$$

where we define $A_{L_1L_2L_3} \equiv \prod_i 4\pi/(2L_i+1)$. Using the identity Eq. A.26 to evaluate the sum of Gaunt factors, we may write

$$\langle\delta_{\ell_1 m_1}(r_1)\delta_{\ell_2 m_2}(r_2)\delta_{\ell_3 m_3}(r_3)\rangle = \sqrt{(4\pi)^3(2l_1+1)(2l_2+1)(2l_3+1)}\begin{pmatrix} l_1 & l_2 & l_3 \\ m_1 & m_2 & m_3 \end{pmatrix}$$
$$\times \sum_{L_1L_2L_3} f_{L_1L_2L_3}(r_1,r_2,r_3)(-1)^{L_1+L_2+L_3}\begin{Bmatrix} l_1 & l_2 & l_3 \\ L_1 & L_2 & L_3 \end{Bmatrix}\begin{pmatrix} l_1 & L_1 & L_3 \\ 0 & 0 & 0 \end{pmatrix}\begin{pmatrix} l_2 & L_2 & L_1 \\ 0 & 0 & 0 \end{pmatrix}\begin{pmatrix} l_3 & L_3 & L_2 \\ 0 & 0 & 0 \end{pmatrix}. \tag{B.3}$$

The Wigner $3j$ symbols inside the sum over the L_i impose that $l_1+l_2+l_3$ be even, hence the sum is proportional to the symbol $\begin{pmatrix} l_1 & l_2 & l_3 \\ 0 & 0 & 0 \end{pmatrix}$, and $\langle\delta_{\ell_1 m_1}(r_1)\delta_{\ell_2 m_2}(r_2)\delta_{\ell_3 m_3}(r_3)\rangle$, to the Gaunt factor $\mathcal{G}^{l_1l_2l_3}_{m_1m_2m_3}$, which encodes the isotropy. The 3-point function of the SFB modes is then obtained by applying the basis transformation Eq. 5.1, hence it is real.

5.C An identity for integrating a product of three spherical harmonics

Here we derive the identity

$$I^{l_1l_2l_3}_{m_1m_2m_3}(k_1,k_2,k_3) \equiv \int d^2\hat{\boldsymbol{k}}_1 d^2\hat{\boldsymbol{k}}_2 d^2\hat{\boldsymbol{k}}_3 Y^*_{l_1,m_1}(\hat{\boldsymbol{k}}_1)Y^*_{l_2,m_2}(\hat{\boldsymbol{k}}_2)Y^*_{l_3,m_3}(\hat{\boldsymbol{k}}_3)\delta_D(\boldsymbol{k}_1+\boldsymbol{k}_2+\boldsymbol{k}_3)$$
$$= \frac{4\pi^{\frac{3}{2}}}{k_1k_2k_3}\sqrt{(2l_1+1)}\begin{pmatrix} l_1 & l_2 & l_3 \\ m_1 & m_2 & m_3 \end{pmatrix}\sum_{|m|\le\min(l_2,l_3)} Y_{l_2,m}(\theta_{12},0)Y_{l_3,-m}(\theta_{13},0)(-1)^m\begin{pmatrix} l_1 & l_2 & l_3 \\ 0 & m & -m \end{pmatrix}, \tag{C.1}$$

which we use to calculate the SFB bispectrum in the homogeneous and isotropic Universe, as well as to accelerate part of the calculation of the observed bispectrum.

We need only to show this for k_1, k_2, k_3 which satisfy the triangle inequality, as otherwise the integral clearly vanishes. Above, we define θ_{ij} as the angle between $\boldsymbol{k}_i$ and $\boldsymbol{k}_j$, such that $\cos(\theta_{12}) = \vartheta(k_1,k_2,k_3) \equiv \frac{k_3^2-k_1^2-k_2^2}{2k_1k_2}$ and $\cos(\theta_{13}) = \vartheta(k_1,k_3,k_2)$, and we denote for the unit vector $\hat{\boldsymbol{r}}$ of spherical angles (θ,ϕ), $Y_{\ell,m}(\theta,\phi) \equiv Y_{\ell,m}(\hat{\boldsymbol{r}})$. The angle-averaged form of Eq. C.1 is denoted $I_{l_1l_2l_3}(k_1,k_2,k_3)$ such that

$$I^{l_1l_2l_3}_{m_1m_2m_3}(k_1,k_2,k_3) = \begin{pmatrix} l_1 & l_2 & l_3 \\ m_1 & m_2 & m_3 \end{pmatrix} I_{l_1l_2l_3}(k_1,k_2,k_3)\,. \tag{C.2}$$

We begin by using Eq. A.1 and Eq. A.3 to write

$$\delta_D(\boldsymbol{k}_1+\boldsymbol{k}_2+\boldsymbol{k}_3) = k_3^{-2}\delta_D(|\boldsymbol{k}_1+\boldsymbol{k}_2|-k_3)\delta_D(\widehat{\boldsymbol{k}_1+\boldsymbol{k}_2}+\hat{\boldsymbol{k}}_3)$$
$$= (k_1k_2k_3)^{-1}\delta_D(\hat{\boldsymbol{k}}_1\cdot\hat{\boldsymbol{k}}_2-\vartheta(k_1,k_2,k_3))\delta_D(\widehat{\boldsymbol{k}_1+\boldsymbol{k}_2}+\hat{\boldsymbol{k}}_3)\,, \tag{C.3}$$

such that, after integration over $d^2\hat{\boldsymbol{k}}_3$, Eq. C.1 becomes

$$I^{l_1l_2l_3}_{m_1m_2m_3}(k_1,k_2,k_3) = (k_1k_2k_3)^{-1}(-1)^{l_3}\int d^2\hat{\boldsymbol{k}}_1\, d^2\hat{\boldsymbol{k}}_2\, Y^*_{l_1,m_1}(\hat{\boldsymbol{k}}_1)\, Y^*_{l_2,m_2}(\hat{\boldsymbol{k}}_2)\, Y^*_{l_3,m_3}\big((\widehat{\boldsymbol{k}_1+\boldsymbol{k}_2})\big)$$
$$\times\,\delta_D\big(\hat{\boldsymbol{k}}_1\cdot\hat{\boldsymbol{k}}_2 - \vartheta(k_1,k_2,k_3)\big)\,, \tag{C.4}$$

where we used the parity property Eq. A.19. We then integrate over $\hat{\boldsymbol{k}}_2$ by rotating it through an angle φ_2 around $\hat{\boldsymbol{k}}_1$, as the Dirac delta fixes $\cos(\theta_{12}) = \vartheta(k_1,k_2,k_3)$. Then $\cos(\pi-\theta_{13})$ also remains fixed and $\widehat{\boldsymbol{k}_1+\boldsymbol{k}_2}$ rotates about $\hat{\boldsymbol{k}}_1$ by the same angle φ_2.

We denote by $\mathcal{R}(\hat{\boldsymbol{k}}_1)$ the rotation sending the axis $\hat{\boldsymbol{z}}$ to $\hat{\boldsymbol{k}}_1$. Using the rotation formula for spherical harmonics Eq. A.11 and integrating over $\hat{\boldsymbol{k}}_1\cdot\hat{\boldsymbol{k}}_2$, Eq. C.4 becomes

$$I^{l_1l_2l_3}_{m_1m_2m_3}(k_1,k_2,k_3) = (k_1k_2k_3)^{-1}(-1)^{l_3}\int d^2\hat{\boldsymbol{k}}_1\, d\varphi_2\, Y^*_{l_1,m_1}(\hat{\boldsymbol{k}}_1)$$
$$\times\left[\sum_{m_2'=-l_2}^{l_2} D^{(l_2)}_{m_2,m_2'}(\mathcal{R}(\hat{\boldsymbol{k}}_1))\, Y^*_{l_2,m_2'}(\theta_{12},\varphi_2)\right]\left[\sum_{m_3'=-l_3}^{l_3} D^{(l_3)}_{m_3,m_3'}(\mathcal{R}(\hat{\boldsymbol{k}}_1))\, Y^*_{l_3,m_3'}(\pi-\theta_{13},\varphi_2)\right]. \tag{C.5}$$

where $D^{(\ell)}_{m,m'}(\mathcal{R}(\hat{\boldsymbol{k}}_1))$ are Wigner D-matrix elements. As $Y^*_{\ell,m}(\theta,\phi)$ is proportional to $e^{-im\phi}$, integrating the pairwise products of spherical harmonics over $d\varphi_2$ gives factors $2\pi\delta^K_{m_2',-m_3'}$. Hence

$$I^{l_1l_2l_3}_{m_1m_2m_3}(k_1,k_2,k_3) = 2\pi(k_1k_2k_3)^{-1}(-1)^{l_3}\sum_{m_2'=-\min(l_2,l_3)}^{\min(l_2,l_3)} Y^*_{l_2,m_2'}(\theta_{12},0)\, Y^*_{l_3,-m_2'}(\pi-\theta_{13},0)$$
$$\times\int d^2\hat{\boldsymbol{k}}_1\, Y^*_{l_1,m_1}(\hat{\boldsymbol{k}}_1) D^{(l_2)}_{m_2,m_2'}(\mathcal{R}(\hat{\boldsymbol{k}}_1)) D^{(l_3)}_{m_3,-m_2'}(\mathcal{R}(\hat{\boldsymbol{k}}_1))\,, \tag{C.6}$$

where $D^{(\ell)}_{mm'}(\mathcal{R})$ is the Wigner D-matrix. Using Eq. A.13, the integral in Eq. C.6 becomes

$$\int d^2\hat{\boldsymbol{k}}_1\, Y^*_{l_1,m_1}(\hat{\boldsymbol{k}}_1)\, D^{(l_2)}_{m_2,m_2'}(\mathcal{R}(\hat{\boldsymbol{k}}_1))\, D^{(l_3)}_{m_3,-m_2'}(\mathcal{R}(\hat{\boldsymbol{k}}_1))$$
$$= \sum_{J=|l_2-l_3|}^{l_2+l_3} \langle l_2m_2\, l_3m_3|J(m_2+m_3)\rangle\langle l_2m_2' l_3(-m_2')|J0\rangle\int d^2\hat{\boldsymbol{k}}_1\, Y^*_{l_1,m_1}(\hat{\boldsymbol{k}}_1) D^{J}_{m_2+m_3,0}(\mathcal{R}(\hat{\boldsymbol{k}}_1))$$
$$= (-1)^{m_1}\sqrt{\frac{4\pi}{2l_1+1}}\,\langle l_2m_2\, l_3m_3|l_1(-m_1)\rangle\langle l_2m_2' l_3(-m_2')|l_10\rangle\,, \tag{C.7}$$

where the second equation above follows from the first by applying the identity Eq. A.12 to write

$$D^{J}_{m_2+m_3,0}(\mathcal{R}(\hat{\boldsymbol{k}}_1)) = \sqrt{\frac{4\pi}{2J+1}} Y^{*}_{J,m_2+m_3}(\hat{\boldsymbol{k}}_1)\,, \tag{C.8}$$

and then using the orthogonality of spherical harmonics Eq. A.10. We obtain the final expression Eq. C.1 by expressing the Clebsch-Gordan coefficients in terms of Wigner $3j$'s via Eq. A.14 and inserting Eq. C.7 into Eq. C.6. In writing Eq. C.1 we have also removed the complex conjugations from the spherical harmonics as they are real, and used the parity of associated Legendre polynomials Eq. A.8.

It is also instructive to rewrite the integral Eq. C.1 to make explicit the consequence of isotropy. Using that

$$\delta_D(\boldsymbol{k}_1 + \boldsymbol{k}_2 + \boldsymbol{k}_3) = \frac{1}{(2\pi)^3} \int \mathrm{d}^3\boldsymbol{r}\, e^{i(\boldsymbol{k}_1+\boldsymbol{k}_2+\boldsymbol{k}_3)\cdot\boldsymbol{r}}\,, \tag{C.9}$$

and Eq. A.16 (for $\alpha = 0$), Eq. C.1 becomes

$$I^{l_1 l_2 l_3}_{m_1 m_2 m_3}(k_1, k_2, k_3) = 8 i^{l_1+l_2+l_3} \int r^2 \mathrm{d}r\, j_{l_1}(k_1 r) j_{l_2}(k_2 r) j_{l_3}(k_3 r) \int d^2\hat{\boldsymbol{r}}\, Y^{*}_{l_1,m_1}(\hat{\boldsymbol{r}}) Y^{*}_{l_2,m_2}(\hat{\boldsymbol{r}}) Y^{*}_{l_3,m_3}(\hat{\boldsymbol{r}})\,, \tag{C.10}$$

where the angular integral is the Gaunt factor $\mathcal{G}^{l_1 l_2 l_3}_{m_1 m_2 m_3}$ encoding the isotropy. The above radial integral of the product of three spherical Bessel functions has been evaluated analytically and by recursion in [185–188], though typically with methods requiring more computation than Eq. C.1. During the preparation of the paper on which this chapter is based, the authors became aware of Ref.[189], which also evaluated the radial integral, leading to a result equivalent to Eq. C.1 via an alternate derivation.

5.D Details of the bispectrum computation

Legendre expansion coefficients $Z_{l_1 l_2 l_3}(r, k_1, k_2)$

In this subsection we derive the coefficients $Z_{l_1 l_2 l_3}(r, k_1, k_2)$ introduced in Eq. 5.66, which we reproduce here:

$$\begin{aligned}\tilde{Z}_2(\boldsymbol{k}_1, \boldsymbol{k}_2, \boldsymbol{r}) &= \sum_{l_1 l_2 l_3} Z_{l_1 l_2 l_3}(k_1, k_2, r)\, \mathcal{L}_{l_1}(\hat{\boldsymbol{k}}_1 \cdot \hat{\boldsymbol{k}}_2)\, \mathcal{L}_{l_2}(\hat{\boldsymbol{k}}_1 \cdot \hat{\boldsymbol{r}})\, \mathcal{L}_{l_3}(\hat{\boldsymbol{k}}_2 \cdot \hat{\boldsymbol{r}}) \\ &= \sum_{\{l_i m_i\}} \frac{(4\pi)^3 Z_{l_1 l_2 l_3}(k_1, k_2, r)}{(2l_1+1)(2l_2+1)(2l_3+1)} Y_{l_1 m_1}(\hat{\boldsymbol{k}}_1) Y^{*}_{l_1 m_1}(\hat{\boldsymbol{k}}_2) Y_{l_2 m_2}(\hat{\boldsymbol{k}}_1) Y^{*}_{l_2 m_2}(\hat{\boldsymbol{r}}) Y_{l_3 m_3}(\hat{\boldsymbol{k}}_2) Y^{*}_{l_3 m_3}(\hat{\boldsymbol{r}})\,.\end{aligned} \tag{D.1}$$

We first note that the form of $Z_2(\boldsymbol{k}_1, \boldsymbol{k}_2, \boldsymbol{r})$ (see Eq. 5.28) implies that it can be written as a polynomial in μ_1, μ_2, $\hat{\boldsymbol{k}}_1 \cdot \hat{\boldsymbol{k}}_2$, and $\mu = (k_1\mu_1 + k_2\mu_2)/k$, except for the terms proportional to $f_{\rm NL}$:

$$f_{\rm NL}\frac{\alpha(k)}{\alpha(k_1)\,\alpha(k_2)}\left(b_{10}^{\rm E} + f(r)\mu^2\right) . \tag{D.2}$$

Furthermore, except for the term

$$f(r)\mu^2 G_2(\boldsymbol{k}_1, \boldsymbol{k}_2) , \tag{D.3}$$

$Z_2(\boldsymbol{k}_1, \boldsymbol{k}_2, \boldsymbol{r})$ is a polynomial of in μ_1, μ_2 and $\hat{\boldsymbol{k}}_1 \cdot \hat{\boldsymbol{k}}_2$ alone, which allows us to write the decomposition Eq. 5.66. In fact, Eq. D.3 could also be included in this decomposition, by writing

$$\mu^2 = \frac{(\mu k)^2}{k_1^2 + k_2^2 + 2k_1k_2\hat{\boldsymbol{k}}_1 \cdot \hat{\boldsymbol{k}}_2} = \frac{(k_1\mu_1 + k_2\mu_2)^2}{k_1^2 + k_2^2}\sum_{n\geq 0}\left(-\frac{2k_1k_2}{k_1^2 + k_2^2}\hat{\boldsymbol{k}}_1 \cdot \hat{\boldsymbol{k}}_2\right)^n . \tag{D.4}$$

However, then the sum over l_1, l_2, l_3 in Eq. 5.66 becomes infinite, and truncating this slowly-converging series after even a small number of terms greatly increases the number of non-vanishing coefficients $Z_{l_1l_2l_3}$. Hence, we opt to treat Eq. D.3 along with Eq. D.2 separately (and exactly) as described in Appendix 5.D.

Leaving out these terms, we have only 9 coefficients $Z_{l_1l_2l_3}(r, k_1, k_2)$, which are listed below by triplet (l_1, l_2, l_3). We have dropped the implicit r-dependence for brevity.

$$(0,0,0): \quad \frac{1}{3}b^{\mathrm{E}}_{10}f + \frac{17}{21}b^{\mathrm{E}}_{10} + \frac{1}{2}b^{\mathrm{E}}_{20} + \frac{1}{9}f^2 + \frac{b^{\mathrm{E}}_{01}f}{6\alpha(k_1)} + \frac{b^{\mathrm{E}}_{01}f}{6\alpha(k_2)} + \frac{b^{\mathrm{E}}_{11}}{2\alpha(k_1)} + \frac{b^{\mathrm{E}}_{11}}{2\alpha(k_2)} + \frac{b^{\mathrm{E}}_{02}}{\alpha(k_1)\alpha(k_2)} \tag{D.5}$$

$$(0,0,2): \quad \frac{1}{9}f(3b^{\mathrm{E}}_{10} + 2f) + f\frac{b^{\mathrm{E}}_{01}}{3\alpha(k_1)} \tag{D.6}$$

$$(0,1,1): \quad \left(\frac{k_1}{2k_2} + \frac{k_2}{2k_1}\right)f(b^{\mathrm{E}}_{10} + \frac{3}{5}f) + b^{\mathrm{E}}_{01}f\left(\frac{k_2}{2k_1\alpha(k_2)} + \frac{k_1}{2k_2\alpha(k_1)}\right) \tag{D.7}$$

$$(0,1,3): \quad f^2\frac{k_2}{5k_1} \tag{D.8}$$

$$(0,2,0): \quad \frac{1}{9}f(3b^{\mathrm{E}}_{10} + 2f) + f\frac{b^{\mathrm{E}}_{01}}{3\alpha(k_2)} \tag{D.9}$$

$$(0,2,2): \quad \frac{4}{9}f^2 \tag{D.10}$$

$$(0,3,1): \quad f^2\frac{k_1}{5k_2} \tag{D.11}$$

$$(1,0,0): \quad b^{\mathrm{E}}_{10}\left(\frac{k_1}{2k_2} + \frac{k_2}{2k_1}\right) + b^{\mathrm{E}}_{01}\left(\frac{k_2}{2k_1\alpha(k_2)} + \frac{k_1}{2k_2\alpha(k_1)}\right) \tag{D.12}$$

$$(2,0,0): \quad \frac{4}{21} \tag{D.13}$$

Derivation of the observed SFB bispectrum Eq. 5.67

Here we detail the remainder of the derivation of the observed bispectrum Eq. 5.67 after the Legendre expansion of the second-order redshift-space kernel has been performed as in Section 5.D.

We first insert the decomposition of $\tilde{Z}_2(\boldsymbol{k}_1, \boldsymbol{k}_2, \boldsymbol{r})$ (Eq. D.1) into $\delta^{g,(2)}_{lm}$ (Eq. 5.64), and use the identity in Eq. A.15 to simplify the complex exponentials. We rid of the angular integrals over $\hat{\boldsymbol{q}}$ with the orthogonality relation for spherical harmonics Eq. A.10. After rearranging for the angular and radial integrals and assuming a separable window $W(\boldsymbol{r}) = W(r)W(\hat{\boldsymbol{r}})$, we obtain

$$\delta^{g,(2)}_{\ell m}(k) = \sqrt{\frac{2}{\pi}}\, k \int \mathrm{d}r\, r^2\, j_\ell(kr)\, W(r)\, D^2(r)\, 4\pi \int \frac{\mathrm{d}k_1\, k_1}{(2\pi)^3} \int \frac{\mathrm{d}k_2\, k_2}{(2\pi)^3} \sum_{\{l_i m_i\}} \frac{(4\pi)^3 Z_{l_1 l_2 l_3}(k_1, k_2, r)}{(2l_1{+}1)(2l_2{+}1)(2l_3{+}1)}$$
$$\times\, r^2 (4\pi)^3 \sum_{\{L_i M_i\}} \sum_{LM} i^{-L_1-L_2+L_3+L_4} j_{L_3}(k_1 r)\, j_{L_4}(k_2 r)\, \delta^{(1)}_{L_1 M_1}(k_1)\, \delta^{(1)}_{L_2 M_2}(k_2)$$
$$\times\, \frac{\pi}{2r^2}\, \mathcal{G}^{L_3\, L_4\, L}_{M_3 M_4 M} \int \mathrm{d}^2\hat{\boldsymbol{r}}\, W(\hat{\boldsymbol{r}})\, Y_{LM}(\hat{\boldsymbol{r}})\, Y^*_{\ell m}(\hat{\boldsymbol{r}})\, Y^*_{l_2 m_2}(\hat{\boldsymbol{r}})\, Y^*_{l_3 m_3}(\hat{\boldsymbol{r}})$$
$$\times \int \mathrm{d}^2\hat{\boldsymbol{k}}_1\, Y_{l_1 m_1}(\hat{\boldsymbol{k}}_1)\, Y_{l_2 m_2}(\hat{\boldsymbol{k}}_1)\, Y_{L_3 M_3}(\hat{\boldsymbol{k}}_1)\, Y_{L_1 M_1}(\hat{\boldsymbol{k}}_1) \int \mathrm{d}^2\hat{\boldsymbol{k}}_2\, Y^*_{l_1 m_1}(\hat{\boldsymbol{k}}_2)\, Y_{l_3 m_3}(\hat{\boldsymbol{k}}_2)\, Y_{L_4 M_4}(\hat{\boldsymbol{k}}_2)\, Y_{L_2 M_2}(\hat{\boldsymbol{k}}_2)\,. \tag{D.14}$$

We may rewrite this more compactly as

$$\delta^{g,(2)}_{\ell m}(k) = \int \mathrm{d}k_1 \int \mathrm{d}k_2 \sum_{L_1 M_1} \sum_{L_2 M_2} \mathcal{V}^{\ell L_1 L_2}_{m M_1 M_2}(k, k_1, k_2)\, \delta^{(1)}_{L_1 M_1}(k_1)\, \delta^{(1)}_{L_2 M_2}(k_2)\,, \tag{D.15}$$

where we use $\mathcal{V}$ to denote the second-order coupling kernel in the SFB bispectrum

$$\mathcal{V}^{\ell L_1 L_2}_{m M_1 M_2}(k, k_1, k_2) \equiv \sqrt{\frac{\pi}{2}}\, 2^8 \pi\, k k_1 k_2 \int \mathrm{d}r\, r^2\, j_\ell(kr)\, W(r)\, D^2(r) \sum_{l_1 l_2 l_3} \frac{Z_{l_1 l_2 l_3}(k_1, k_2, r)}{(2l_1+1)\,(2l_2+1)\,(2l_3+1)}$$
$$\times \sum_{L_3 L_4} j_{L_3}(k_1 r)\, j_{L_4}(k_2 r)\, \mathcal{C}^{L_1\, L_2\, \ell\, , L_3 L_4}_{M_1 M_2 m, l_1 l_2 l_3}\,. \tag{D.16}$$

Here $C^{L_1\, L_2\, \ell\, , L_3 L_4}_{M_1 M_2 m, l_1 l_2 l_3}$ is a mode coupling coefficient

$$\mathcal{C}^{L_1\, L_2\, \ell\, , L_3 L_4}_{M_1 M_2 m, l_1 l_2 l_3} = i^{-L_1-L_2+L_3+L_4} \sum_{m_1 m_2 m_3} \sum_{M_3 M_4} \sum_{LM} (-1)^{M+m_1} \mathcal{G}^{L_3 L_4 L}_{M_3 M_4 M} \mathcal{H}^{L \ell l_2 l_3}_{-M m m_2 m_3} \mathcal{H}^{l_1 l_2 L_3 L_1}_{m_1 m_2 M_3 M_1} \mathcal{H}^{l_1 l_3 L_4 L_2}_{-m_1 m_3 M_4 M_2}\,. \tag{D.17}$$

and

$$\mathcal{H}^{l_1 l_2 l_3 l_4}_{m_1 m_2 m_3 m_4} \equiv \int \mathrm{d}^2\hat{\boldsymbol{r}}\; W(\hat{\boldsymbol{r}}) Y_{l_1 m_1}(\hat{\boldsymbol{r}}) Y_{l_2 m_2}(\hat{\boldsymbol{r}}) Y_{l_3 m_3}(\hat{\boldsymbol{r}}) Y_{l_4 m_4}(\hat{\boldsymbol{r}}) \tag{D.18}$$

is the integral over four spherical harmonics and the angular part of the window function.

Using the form of $\delta^{g,(1)}_{\ell m}(k)$ in Eq. 5.10, the terms contributing to the tree-level 3-point correlation function of the SFB modes are

$$\left\langle \delta^{g,(2)}_{\ell m}(k)\, \delta^{g,(1)}_{\ell' m'}(k')\, \delta^{g,(1)}_{\ell'' m''}(k'') \right\rangle$$
$$= \int \mathrm{d}k_1 \int \mathrm{d}k_2 \sum_{L_1 M_1} \sum_{L_2 M_2} \mathcal{V}^{\ell L_1 L_2}_{m M_1 M_2}(k, k_1, k_2) \int \mathrm{d}q' \sum_{L' M'} \mathcal{W}^{L' M'}_{\ell' m'}(k', q') \int \mathrm{d}q'' \sum_{L'' M''} \mathcal{W}^{L'' M''}_{\ell'' m''}(k'', q'')$$
$$\times \left\langle \delta^{(1)}_{L_1 M_1}(k_1)\, \delta^{(1)}_{L_2 M_2}(k_2)\, \delta^{(1)}_{L' M'}(q')\, \delta^{(1)}_{L'' M''}(q'') \right\rangle\,, \tag{D.19}$$

along with the two other terms with cyclically permuted superscript indices. Noting that the SFB power spectrum for the constant-time slice matter density contrast is homogeneous and isotropic, i.e.

$$\left\langle \delta^{(1)}_{L_1 M_1}(k_1)\, \delta^{(1)}_{L_2 M_2}(k_2) \right\rangle = \delta^K_{L_1 L_2} \delta^K_{M_1 - M_2} (-1)^{M_2} \delta^D(k_1 - k_2)\, P(k_1)\,, \tag{D.20}$$

we may apply Wick's theorem,

$$\begin{aligned}
&\left\langle \delta^{g,(2)}_{\ell m}(k)\, \delta^{g,(1)}_{\ell' m'}(k')\, \delta^{g,(1)}_{\ell'' m''}(k'') \right\rangle \\
&= \int \mathrm{d}k_1 \sum_{L_1 M_1} (-1)^{M_1} \mathcal{V}^{\ell L_1 L_1}_{m M_1 - M_1}(k, k_1, k_1)\, P(k_1) \int \mathrm{d}q' \sum_{L' M'} (-1)^{M'} \mathcal{W}^{L' M'}_{\ell' m'}(k', q')\, \mathcal{W}^{L' - M'}_{\ell'' m''}(k'', q')\, P(q') \\
&+ \int \mathrm{d}q' \int \mathrm{d}q'' \sum_{L' M'} \sum_{L'' M''} (-1)^{M' + M''} \mathcal{V}^{\ell L' L''}_{m - M' - M''}(k, q', q'')\, \mathcal{W}^{L' M'}_{\ell' m'}(k', q')\, \mathcal{W}^{L'' M''}_{\ell'' m''}(k'', q'')\, P(q')\, P(q'') \\
&+ \int \mathrm{d}q' \int \mathrm{d}q'' \sum_{L'' M''} \sum_{L' M'} (-1)^{M' + M''} \mathcal{V}^{\ell L'' L'}_{m - M'' - M'}(k, q'', q')\, \mathcal{W}^{L' M'}_{\ell' m'}(k', q')\, \mathcal{W}^{L'' M''}_{\ell'' m''}(k'', q'')\, P(q')\, P(q'')\,.
\end{aligned} \tag{D.21}$$

From here on we assume a spherically symmetric window $W(\boldsymbol{r}) = W(r)$. Then we have $\mathcal{W}^{LM}_{\ell m}(k, q) = \delta^K_{\ell L} \delta^K_{m M}\, \mathcal{W}_\ell(k, q)$. Hence,

$$\begin{aligned}
&\left\langle \delta^{g,(2)}_{\ell m}(k)\, \delta^{g,(1)}_{\ell' m'}(k')\, \delta^{g,(1)}_{\ell'' m''}(k'') \right\rangle \\
&= \delta^K_{\ell' \ell''} \delta^K_{m' - m''} (-1)^{m'} C_{\ell'}(k', k'') \int \mathrm{d}k_1 \sum_{L_1 M_1} (-1)^{M_1} \mathcal{V}^{\ell L_1 L_1}_{m M_1 - M_1}(k, k_1, k_1)\, P(k_1) \\
&+ \int \mathrm{d}q'\, \mathcal{W}_{\ell'}(k', q')\, P(q') \int \mathrm{d}q''\, \mathcal{W}_{\ell''}(k'', q'')\, P(q'') (-1)^{m' + m''} \left[\mathcal{V}^{\ell \ell' \ell''}_{m - m' - m''}(k, q', q'') + \mathcal{V}^{\ell \ell'' \ell'}_{m - m'' - m'}(k, q'', q') \right].
\end{aligned} \tag{D.22}$$

In Eq. D.15 swapping $L_1 \leftrightarrow L_2, k_1 \leftrightarrow k_2, M_1 \leftrightarrow M_2$ gives $\mathcal{V}^{\ell L_1 L_2}_{m M_1 M_2}(k, k_1, k_2) = \mathcal{V}^{\ell L_2 L_1}_{m M_2 M_1}(k, k_2, k_1)$, thus the two terms in brackets in Eq. D.22 are equal. In Appendix 5.D we simplify $\mathcal{V}^{\ell \ell' \ell''}_{m - m' - m''}$ and show that it is proportional to the Gaunt factor $\mathcal{G}^{\ell \ell' \ell''}_{m m' m''}$. Hence we define the angle-averaged quantity

$$\mathcal{V}^{\ell \ell' \ell''}(k, k', k'') \equiv \sum_{m m' m''} \begin{pmatrix} \ell & \ell' & \ell'' \\ m & m' & m'' \end{pmatrix} (-1)^{m' + m''} \mathcal{V}^{\ell \ell' \ell''}_{m - m' - m''}(k, k', k'')\,, \tag{D.23}$$

whose simplified expression is given by Eq. D.33.

In fact, the first line of Eq. D.22 always vanishes when $\ell > 0$, which we may see by the following quick argument. By the remarks at the beginning of Section 5.2 on observational isotropy, Eq. D.22 must be proportional to the Gaunt factor $\mathcal{G}^{\ell\ell'\ell''}_{mm'm''}$, such that Eq. D.22 is nonzero only if ℓ, ℓ', ℓ'' form a triangle. This condition is already imposed by the second line of Eq. D.22. Let $\ell > 0$ and set $\ell' = \ell'' = 0$ such that the triangle condition is violated. As $C_0(k', k'') \neq 0$, the integral in the first line of Eq. D.22 must vanish, and consequently the first line must vanish for any (ℓ, ℓ', ℓ'') with $\ell > 0$. The authors of Ref. [166] demonstrate this directly with a lengthy derivation.

Finally, after angle-averaging with Eq. 5.45 and re-indexing for clarity, the SFB bispectrum, ignoring contributions from the $f_{\rm NL}$ and G_2 terms, is given by

$$B^{\mathrm{SFB},\tilde{Z}_2}_{l_1 l_2 l_3}(k_1, k_2, k_3) = 2\int \mathrm{d}q_2\, \mathcal{W}_{l_2}(k_2, q_2) P(q_2) \int \mathrm{d}q_3\, \mathcal{W}_{l_3}(k_3, q_3) P(q_3)\, \mathcal{V}^{l_1 l_2 l_3}(k_1, q_2, q_3) \\ + 2 \text{ cyc. perm.} \tag{D.24}$$

The contribution from the $f_{\rm NL}$ and G_2 terms is given in Appendix 5.D (Eq. D.46). It is of a similar form to the contribution from the terms in $\tilde{Z}_2$.

In principle, it is possible to repeat the above derivation while relaxing the assumption that $W(\boldsymbol{r})$ is spherically symmetric (but keeping the assumption that the radial and angular dependencies are separable) by decomposing $W(\hat{\boldsymbol{r}})$ into spherical harmonics. However, as in this case we can no longer leverage observational isotropy of the signal, the calculation is significantly more complicated (and expensive), so we leave the details to a future work.

Lastly, it is useful to verify that we retrieve Eq. 5.55 in the limit of an isotropic and homogeneous Universe, i.e. by setting $D = b_1 = W = 1$ and $f = 0$. In this case, the second term in Eq. 5.67 vanishes, and we may take $W_\ell(k, q) = \delta_D(k - q)$, such that

$$B^{\mathrm{SFB}}_{l_1 l_2 l_3}(k_1, k_2, k_3) = 2P(k_2)P(k_3)\, \mathcal{V}^{l_1 l_2 l_3}(k_1, k_2, k_3) + 2 \text{ cyc. perm.}. \tag{D.25}$$

As it is somewhat tedious to demonstrate equivalence with Eq. 5.55 analytically, we omit the details here[6]; as a test of our code, we verify numerically that Eq. D.25 and Eq. 5.55 are identical in the considered limit.

Simplification of the kernel $\mathcal{V}^{L_1 L_2 \ell}_{M_1 M_2 m}(k, k_1, k_2)$

We now show that, under the assumption of a spherically symmetric window $W(\boldsymbol{r}) = W(r)$, the kernel $\mathcal{V}^{\ell L_1 L_2}_{m M_1 M_2}$ is proportional to the Gaunt factor $\mathcal{G}^{L_1 L_2 \ell}_{M_1 M_2 -m}$, and compute

[6] For a lengthy proof along these lines see Ref. [166].

its angle-averaged expression, defined by Eq. D.23. For compactness, we will denote the Wigner coefficient $\begin{pmatrix} \ell_1 & \ell_2 & \ell_3 \\ m_1 & m_2 & m_3 \end{pmatrix}$ by $K^{\ell_1\ell_2\ell_3}_{m_1m_2m_3}$ and the coefficient of proportionality between Gaunt factors and Wigner coefficients by

$$f_{\ell_1\ell_2\ell_3} \equiv \left(\frac{(2\ell_1+1)(2\ell_2+1)(2\ell_3+1)}{4\pi}\right)^{\frac{1}{2}} \begin{pmatrix} \ell_1 & \ell_2 & \ell_3 \\ 0 & 0 & 0 \end{pmatrix}, \tag{D.26}$$

such that $\mathcal{G}^{\ell_1\ell_2\ell_3}_{m_1m_2m_3} = f_{\ell_1\ell_2\ell_3} K^{\ell_1\ell_2\ell_3}_{m_1m_2m_3}$.

First, we use the identity Eq. A.23 to evaluate the integral over four spherical harmonics Eq. D.18, such that we may express Eq. D.17 in terms of Gaunt factors[7]. We also use that the sum of the lower indices of the Gaunt factor must vanish, to write

$$\begin{aligned} \mathcal{C}^{L_1\,L_2\,\ell\,,L_3L_4}_{M_1\,M_2 m,l_1l_2l_3} = i^{-L_1-L_2+L_3+L_4} \sum_{L,H_1,H_2,H_3} \sum_{m_1,m_2,m_3,M_3,M_4,M} (-1)^{m+m_1+m_2+m_3} \\ \times \mathcal{G}^{L_3L_4L}_{M_3M_4M} \mathcal{G}^{L\ell H_1}_{-Mm-N_1} \mathcal{G}^{H_1l_2l_3}_{N_1m_2m_3} \mathcal{G}^{l_1l_2H_2}_{m_1m_2-N_2} \mathcal{G}^{H_2L_3L_1}_{N_2M_3M_1} \mathcal{G}^{l_1l_3H_3}_{-m_1m_3-N_3} \mathcal{G}^{H_3L_4L_2}_{N_3M_4M_2}, \end{aligned} \tag{D.27}$$

where the sums over N_1, N_2, and N_3 have only one term each, and are thus not explicitly written. With Eq. A.25, and changing signs on the summation variables, we can use Eq. A.26 to simplify the inner sum

$$\begin{aligned} &\sum_{m_1m_2m_3} (-1)^{m_1+m_2+m_3} \mathcal{G}^{H_1l_2l_3}_{N_1m_2m_3} \mathcal{G}^{l_1l_2H_2}_{m_1m_2-N_2} \mathcal{G}^{l_1l_3H_3}_{-m_1m_3-N_3} \\ &= f_{H_1l_2l_3} f_{H_2l_1l_2} f_{H_3l_1l_3} (-1)^{H_1+l_2+l_3+H_3+l_1+l_3} \sum_{m_1m_2m_3} (-1)^{m_1+m_2+m_3} K^{H_1l_2l_3}_{-N_1m_2-m_3} K^{l_1H_3l_3}_{-m_1-N_3m_3} K^{l_1l_2H_2}_{m_1-m_2-N_2} \\ &= f_{H_1l_2l_3} f_{H_2l_1l_2} f_{H_3l_1l_3} (-1)^{l_1+l_2+l_3} K^{H_1H_2H_3}_{-N_1-N_2-N_3} \begin{Bmatrix} H_1 & H_2 & H_3 \\ l_1 & l_3 & l_2 \end{Bmatrix}, \end{aligned} \tag{D.28}$$

where we also used that $l_1 + l_2 + H_2$ must be even. Then, after expressing all Gaunt

[7]Note that if we allow for a generic angular dependence of the window $W(\hat{\boldsymbol{r}})$, it is still possible to evaluate the integral Eq. A.23 by decomposing $W(\hat{\boldsymbol{r}})$ into spherical harmonics and using the generalization of the integral Eq. D.17 to a product of five spherical harmonics. However this leads to an explosion in the number of terms needed to compute the kernel $\mathcal{V}^{\ell L_1 L_2}_{mM_1M_2}$, so in practice only spherically symmetric windows are currently computationally feasible.

factors in terms of Wigner coefficients, Eq. D.27 becomes

$$
\begin{aligned}
\mathcal{C}^{L_1\ L_2\ \ell\ ,L_3L_4}_{M_1M_2m,l_1l_2l_3} &= i^{-L_1-L_2+L_3+L_4} \sum_{L,H_1,H_2,H_3} f_{H_1l_2l_3} f_{H_2l_1l_2} f_{H_3l_1l_3} (-1)^{l_1+l_2+l_3} \begin{Bmatrix} H_1 & H_2 & H_3 \\ l_1 & l_3 & l_2 \end{Bmatrix} (-1)^m \\
&\times f_{L_3L_4L} f_{L\ell H_1} f_{H_2L_3L_1} f_{H_3L_4L_2} \sum_{M_3,M_4,M} K^{L_3L_4L}_{M_3M_4M} K^{L\ell H_1}_{-Mm-N_1} K^{H_2L_3L_1}_{N_2M_3M_1} K^{H_3L_4L_2}_{N_3M_4M_2} K^{H_1H_2H_3}_{-N_1-N_2-N_3} \\
&= i^{-L_1-L_2+L_3+L_4} K^{L_1L_2\ell}_{M_1M_2-m} (-1)^m (-1)^{l_1+l_2+l_3} \\
&\times \sum_{L,H_1,H_2,H_3} f_{H_1l_2l_3} f_{H_2l_1l_2} f_{H_3l_1l_3} f_{L_3L_4L} f_{L\ell H_1} f_{H_2L_3L_1} f_{H_3L_4L_2} (-1)^{H_1+H_2+H_3} \\
&\times \begin{Bmatrix} H_1 & H_2 & H_3 \\ l_1 & l_3 & l_2 \end{Bmatrix} \begin{Bmatrix} H_2 & L_3 & L_1 \\ H_3 & L_4 & L_2 \\ H_1 & L & \ell \end{Bmatrix}, \qquad \text{(D.29)}
\end{aligned}
$$

where we used Eq. A.27 to obtain the last line.

Finally, substituting Eq. D.29 in Eq. D.16 and collecting constant factors, we obtain

$$
\mathcal{V}^{\ell L_1L_2}_{mM_1M_2}(k,k_1,k_2) \equiv (32\pi)^{\frac{3}{2}} k k_1 k_2 \begin{pmatrix} L_1 & L_2 & \ell \\ M_1 & M_2 & -m \end{pmatrix} (-1)^m \sum_{l_1l_2l_3L_3L_4} g^{L_1L_2\ell}_{l_1l_2l_3L_3L_4} J^{\ell L_3L_4}_{l_1l_2l_3}(k,k_1,k_2)\,, \qquad \text{(D.30)}
$$

where we have defined

$$
J^{\ell L_3L_4}_{l_1l_2l_3}(k,k_1,k_2) \equiv \int \mathrm{d}r\, r^2\, j_\ell(kr)\, j_{L_3}(k_1r)\, j_{L_4}(k_2r)\, W(r)\, D^2(r)\, Z_{l_1l_2l_3}(k_1,k_2,r)\,, \qquad \text{(D.31)}
$$

and

$$
\begin{aligned}
g^{L_1L_2\ell}_{l_1l_2l_3L_3L_4} &\equiv \frac{(-1)^{l_1+l_2+l_3}}{(2l_1+1)(2l_2+1)(2l_3+1)} i^{-L_1-L_2+L_3+L_4} \\
&\times \sum_{L,H_1,H_2,H_3} f_{H_1l_2l_3} f_{H_2l_1l_2} f_{H_3l_1l_3} f_{L_3L_4L} f_{L\ell H_1} f_{H_2L_3L_1} f_{H_3L_4L_2} \begin{Bmatrix} H_1 & H_2 & H_3 \\ l_1 & l_3 & l_2 \end{Bmatrix} \begin{Bmatrix} H_2 & L_3 & L_1 \\ H_3 & L_4 & L_2 \\ H_1 & L & \ell \end{Bmatrix}, \qquad \text{(D.32)}
\end{aligned}
$$

which is real. There are 9 triplets (l_1, l_2, l_3) in the Legendre decomposition of the kernel Z_2, excluding contributions from the kernel G_2 and from terms proportional to $f_{\rm NL}$. As a result, for fixed L_1, L_2, ℓ there are at most 49 terms in the sum of Eq. D.30. Finally, angle-averaging with Eq. D.23, we obtain

$$
\mathcal{V}^{\ell L_1L_2}(k,k_1,k_2) \equiv (32\pi)^{\frac{3}{2}} k k_1 k_2 \sum_{l_1l_2l_3L_3L_4} g^{L_1L_2\ell}_{l_1l_2l_3L_3L_4} J^{\ell L_3L_4}_{l_1l_2l_3}(k,k_1,k_2)\,. \qquad \text{(D.33)}
$$

Contribution from the $f_{\rm NL}$ and G_2 terms

Here we address the terms in the kernel Z_2 (Eq. 5.28) that were left out when decomposing Z_2 as polynomial in $\hat{\boldsymbol{k}}_1 \cdot \hat{\boldsymbol{k}}_2$, $\hat{\boldsymbol{k}}_1 \cdot \hat{\boldsymbol{r}}$, and $\hat{\boldsymbol{k}}_2 \cdot \hat{\boldsymbol{r}}$ (Eq. 5.66). These terms are

$$
f_{\rm NL} \frac{\alpha(k,r)}{\alpha\left(k_1,r\right)\alpha\left(k_2,r\right)}\left(b_{10}^{\rm E} + f(r)\mu^2\right) , \tag{D.34}
$$

and

$$
f(r)\mu^2 G_2\left(\boldsymbol{k}_1, \boldsymbol{k}_2\right) . \tag{D.35}
$$

To account for them, it will be advantageous to first write the SFB bispectrum in an alternate form (Eq. D.37), which makes clear the relation of the observed bispectrum to the bispectrum of an isotropic and homogeneous Universe.

Relation between position-dependent bispectrum and SFB bispectrum

The SFB bispectrum is obtained from the position-dependent Fourier-space bispectrum by first transforming Eq. 5.31 to configuration space using Eq. 5.61, and then transforming into SFB space using Eq. 5.1. We get

$$
\begin{aligned}
&\left\langle \delta^{\rm obs}_{g,l_1m_1}(k_1)\delta^{\rm obs}_{g,l_2m_2}(k_2)\delta^{\rm obs}_{g,l_3m_3}(k_3)\right\rangle \\
&= \left(\frac{2}{\pi}\right)^{\frac{3}{2}} k_1k_2k_3 \int \left(\prod_i \frac{1}{(2\pi)^3} r_i^2 \mathrm{d}r_i q_i^2 \mathrm{d}q_i \mathrm{d}^2\hat{\boldsymbol{r}}_i \mathrm{d}^2\hat{\boldsymbol{q}}_i W(\boldsymbol{r}_i) e^{i\boldsymbol{q}_i\cdot\boldsymbol{r}_i} j_{l_i}(k_ir_i) Y^*_{l_i,m_i}(\hat{\boldsymbol{r}}_i)\right) \\
&\times B_s(\boldsymbol{q}_1,\boldsymbol{q}_2,\boldsymbol{q}_3,\boldsymbol{r}_1,\boldsymbol{r}_2,\boldsymbol{r}_3)(2\pi)^3\delta_D(\boldsymbol{q}_1+\boldsymbol{q}_2+\boldsymbol{q}_3) .
\end{aligned} \tag{D.36}
$$

In the absence of RSD, linear growth, galaxy bias, and window, the observed SFB bispectrum (Eq. D.36) reduces to the SFB bispectrum in an isotropic and homogeneous Universe (Eq. 5.50), using Eq. A.6. Unlike in the isotropic and homogeneous case, however, fixing the lengths q_i and imposing $\boldsymbol{q}_1 + \boldsymbol{q}_2 + \boldsymbol{q}_3 = 0$ fixes the angles $\hat{\boldsymbol{q}}_i \cdot \hat{\boldsymbol{q}}_j$ but does not determine $B_s(\boldsymbol{q}_1,\boldsymbol{q}_2,\boldsymbol{q}_3,\boldsymbol{r}_1,\boldsymbol{r}_2,\boldsymbol{r}_3)$, which depends on the nine angles $\mu_{ij} \equiv \hat{\boldsymbol{q}}_i \cdot \hat{\boldsymbol{r}}_j$ to the three lines of sight $\hat{\boldsymbol{r}}_j$.

Assuming a radial window $W(\boldsymbol{r}) = W(r)$, the angle-averaged bispectrum is given by

$$
\begin{aligned}
&B^{\rm SFB,\,obs}_{l_1l_2l_3}(k_1,k_2,k_3) = \frac{1}{(2\pi)^6}\left(\frac{2}{\pi}\right)^{\frac{3}{2}} k_1k_2k_3 \\
&\times \int \left(\prod_i r_i^2 \mathrm{d}r_i q_i^2 \mathrm{d}q_i W(r_i) j_{l_i}(k_ir_i)\right) \mathcal{I}^{\rm ang.}_{l_1l_2l_3}(q_1,q_2,q_3,r_1,r_2,r_3) ,
\end{aligned} \tag{D.37}
$$

where we have defined the angle-averaged angular integral

$$\mathcal{I}^{\text{ang.}}_{l_1 l_2 l_3}(q_1, q_2, q_3, r_1, r_2, r_3) \equiv \sum_{m_1 m_2 m_3} \begin{pmatrix} l_1 & l_2 & l_3 \\ m_1 & m_2 & m_3 \end{pmatrix} \int \left(\prod_i \mathrm{d}^2 \hat{\boldsymbol{r}}_i \mathrm{d}^2 \hat{\boldsymbol{q}}_i e^{i\boldsymbol{q}_i \cdot \boldsymbol{r}_i} Y^*_{l_i, m_i}(\hat{\boldsymbol{r}}_i) \right)$$
$$\times B_s(\boldsymbol{q}_1, \boldsymbol{q}_2, \boldsymbol{q}_3, \boldsymbol{r}_1, \boldsymbol{r}_2, \boldsymbol{r}_3) \delta_D(\boldsymbol{q}_1 + \boldsymbol{q}_2 + \boldsymbol{q}_3)\,. \quad \text{(D.38)}$$

The integral $\mathcal{I}^{\text{ang.}}_{l_1 l_2 l_3}$ is closely related to the TSH bispectrum, and would be the same if we were to integrate over the q_i. However, we use the above definition for clarity later in this Appendix.

G_2 contribution

The contribution from the velocity kernel G_2 in the bispectrum B_s (Eq. 5.32) is given by

$$B_s \supset D_1 D_2 D_3^2 \left(2P(q_1)P(q_2)\right) \left[b_1 + f_1 \mu_{11}^2\right] \left[b_2 + f_2 \mu_{22}^2\right] \left[f_3 G_2(\boldsymbol{q}_1, \boldsymbol{q}_2) \mu_{33}^2\right]$$
$$+2 \text{ cyc. perm.}\,, \quad \text{(D.39)}$$

where we write for brevity in this section $b_i = b^{\mathrm{E}}_{10}(r_i) + b^{\mathrm{E}}_{01}(r_i)/\alpha(k_i, r_i)$, $f_i = f(r_i)$, $D_i = D(r_i)$.

We perform the integrals over $\hat{\boldsymbol{r}}_i$ in Eq. D.38 using the identity Eq. A.16. As $G_2(\boldsymbol{q}_1, \boldsymbol{q}_2)$ is rotationally invariant, when $\boldsymbol{q}_1 + \boldsymbol{q}_2 + \boldsymbol{q}_3 = 0$ we may write it as $G_2(\boldsymbol{q}_1, \boldsymbol{q}_2) = G_2(q_1, q_2, q_3)$, evaluated with $\hat{\boldsymbol{q}}_j \cdot \hat{\boldsymbol{q}}_k = \vartheta(q_j, q_k, q_l)$. The G_2 contribution to Eq. D.38 is thus

$$\mathcal{I}^{\text{ang.}}_{l_1 l_2 l_3} \supset \sum_{m_1 m_2 m_3} \begin{pmatrix} l_1 & l_2 & l_3 \\ m_1 & m_2 & m_3 \end{pmatrix} \int \left(\prod_j \mathrm{d}^2 \hat{\boldsymbol{q}}_j \right) \delta_D(\boldsymbol{q}_1 + \boldsymbol{q}_2 + \boldsymbol{q}_3) \Bigg\{$$
$$\times \left[2 \prod_{i=1,2} D_i P(q_i) 4\pi i^{l_i} Y^*_{l_i, m_i}(\hat{\boldsymbol{q}}_i) \Big(b_i j_{l_i}(q_i r_i) - f_i j''_{l_i}(q_i r_i) \Big) \right]$$
$$\times D_3^2 \Big[-4\pi i^{l_3} Y^*_{l_3, m_3}(\hat{\boldsymbol{q}}_3) f_3 G_2(\boldsymbol{q}_1, \boldsymbol{q}_2) j''_{l_3}(q_3 r_3) \Big] + 2 \text{ cyc. perm.} \Bigg\}$$
$$= (4\pi)^3 i^{l_1 + l_2 + l_3} \left[2 \prod_{i=1,2} P(q_i) D_i \Big(b_i j_{l_i}(q_i r_i) - f_i j''_{l_i}(q_i r_i) \Big) \right] D_3^2 \Big(-f_3 G_2(q_1, q_2, q_3) j''_{l_3}(q_3 r_3) \Big)$$
$$\times \sum_{m_1 m_2 m_3} \begin{pmatrix} l_1 & l_2 & l_3 \\ m_1 & m_2 & m_3 \end{pmatrix} \int d^2 \hat{\boldsymbol{q}}_1 d^2 \hat{\boldsymbol{q}}_2 d^2 \hat{\boldsymbol{q}}_3 Y^*_{l_1, m_1}(\hat{\boldsymbol{q}}_1) Y^*_{l_2, m_2}(\hat{\boldsymbol{q}}_2) Y^*_{l_3, m_3}(\hat{\boldsymbol{q}}_3) \delta_D(\boldsymbol{q}_1 + \boldsymbol{q}_2 + \boldsymbol{q}_3) + 2 \text{ cyc. perm.}\,.$$
$$\text{(D.40)}$$

We recognize the integral in the last line of Eq. D.40 as the integral defined in Eq. C.1, which is proportional to a Wigner-3j symbol. Thus, the sum simplifies with the identity Eq. A.24, and we can express the last line as the integral $I_{l_1 l_2 l_3}(q_1, q_2, q_3)$ of Eq. C.2. We obtain the G_2 contribution to the SFB bispectrum by inserting Eq. D.40 into Eq. D.37. The integrals over r_1 and r_2 can be written compactly in terms of the kernels $\mathcal{W}_l(k, q)$ (Eq. 5.17) as

$$
\begin{aligned}
B^{\mathrm{SFB},G_2}_{l_1 l_2 l_3}(k_1, k_2, k_3) &= \frac{1}{(2\pi)^6}\left(\frac{2}{\pi}\right)^{\frac{3}{2}} k_1 k_2 k_3 (4\pi)^3 i^{l_1+l_2+l_3} \\
&\times \int \left(\prod_i dq_i q_i^2\right) 2P(q_1)P(q_2)\left(\frac{\pi}{2k_1 q_1}\mathcal{W}_{l_1}(k_1, q_1)\right)\left(\frac{\pi}{2k_2 q_2}\mathcal{W}_{l_2}(k_2, q_2)\right) G_2(q_1, q_2, q_3) \\
&\times \left(\int dr_3 r_3^2 W(r_3) j_{l_3}(k_3 r_3) D^2(r_3)(-f(r_3) j''_{l_3}(q_3 r_3))\right) I_{l_1 l_2 l_3}(q_1, q_2, q_3) + 2 \text{ cyc. perm.}\,.
\end{aligned}
\tag{D.41}
$$

Total contribution from f_{NL} and G_2 terms

The contribution from the f_{NL} term Eq. D.34 is analogous to Eq. (D.41). Noting that we may factorize $\alpha(k, r) = \gamma(k) D(r)$ with

$$
\gamma(k) \equiv \frac{2k^2 c^2 T(k)}{3\Omega_m H_0^2}\,, \tag{D.42}
$$

we may define, in analogy to the derivation in 5.4, the kernels [8]

$$
\mathcal{W}^{G_2}_{\ell}(k, q) \equiv \frac{2kq}{\pi}\int dr\, r^2 W(r) j_\ell(kr) D^2(r)\Big(-f(r) j''_\ell(qr)\Big) \tag{D.43}
$$

$$
\mathcal{W}^{f_{\mathrm{NL}}}_{\ell}(k, q) \equiv \frac{2kq}{\pi}\int dr\, r^2 W(r) j_\ell(kr) D(r)\Big(b^{\mathrm{E}}_{10}(r) j_\ell(qr) - f(r) j''_\ell(qr)\Big) \tag{D.44}
$$

$$
\begin{aligned}
\mathcal{V}^{l_3 l_1 l_2}_{f_{\mathrm{NL}},G_2}(k_3, q_1, q_2) &\equiv \frac{1}{(2\pi)^{\frac{3}{2}}} i^{l_1+l_2+l_3}\int dq_3 (q_1 q_2 q_3) I_{l_1 l_2 l_3}(q_1, q_2, q_3) \\
&\times \left[G_2(q_1, q_2, q_3)\mathcal{W}^{G_2}_{l_3}(k_3, q_3) + \left(f_{\mathrm{NL}}\frac{\gamma(q_3)}{\gamma(q_1)\gamma(q_2)}\right)\mathcal{W}^{f_{\mathrm{NL}}}_{l_3}(k_3, q_3)\right].
\end{aligned}
\tag{D.45}
$$

Finally, after reordering the cyclic permutations to match the ordering in the main text, the combined contribution to the bispectrum signal from the f_{NL} and G_2 terms

[8] Note that $\mathcal{W}_l(k, q)$ (Eq. 5.17) differs from Eq. D.44 in that the scale-dependent bias $b(r, q)$ is replaced by $b^{\mathrm{E}}_{10}(r)$.

is

$$B^{\mathrm{SFB},\, f_{\mathrm{NL}}, G_2}_{l_1 l_2 l_3}(k_1, k_2, k_3) = 2 \int \mathrm{d}q_2 \mathcal{W}_{l_2}(k_2, q_2)\, P(q_2) \int \mathrm{d}q_3\, \mathcal{W}_{l_3}(k_3, q_3)\, P(q_3)\, \mathcal{V}^{l_1 l_2 l_3}_{f_{\mathrm{NL}}, G_2}(k_1, q_2, q_3) + 2 \text{ cyc. perm.} \quad \text{(D.46)}$$

The advantage of expressing Eq. D.45 in the above form is that the integral $I_{l_1 l_2 l_3}$ can be rapidly (pre)computed without numerical integration via the identity Eq. C.2.

Bibliography

[1] Spinning echo template notebook.

[2] A. Testa and P. Pani. Analytical template for gravitational-wave echoes: signal characterization and prospects of detection with current and future interferometers. *Phys. Rev. D*, 98(4):044018, 2018. doi:10.1103/PhysRevD.98.044018.

[3] E. Maggio, P. Pani, and V. Ferrari. Exotic compact objects and how to quench their ergoregion instability. *Phys. Rev. D*, 96(10):104047, 2017. doi:10.1103/PhysRevD.96.104047.

[4] E. Maggio, V. Cardoso, S. R. Dolan, and P. Pani. Ergoregion instability of exotic compact objects: electromagnetic and gravitational perturbations and the role of absorption. *Phys. Rev. D*, 99(6):064007, 2019. doi:10.1103/PhysRevD.99.064007.

[5] N. Aghanim et al. Planck 2018 results. vi. cosmological parameters. *Astron. Astrophys.*, 641:A6, 2020. doi:10.1051/0004-6361/201833910.

[6] V. Cardoso, E. Franzin, and P. Pani. Is the gravitational-wave ringdown a probe of the event horizon? *Phys. Rev. Lett.*, 116(17):171101, 2016. doi:10.1103/PhysRevLett.116.171101.

[7] V. Cardoso, S. Hopper, C. F. B. Macedo, C. Palenzuela, and P. Pani. Gravitational-wave signatures of exotic compact objects and of quantum corrections at the horizon scale. *Phys. Rev. D*, 94(8):084031, 2016. doi:10.1103/PhysRevD.94.084031.

[8] N. Oshita and N. Afshordi. Probing microstructure of black hole spacetimes with gravitational wave echoes. *Phys. Rev. D*, 99(4):044002, 2019. doi:10.1103/PhysRevD.99.044002.

[9] Q. Wang, N. Oshita, and N. Afshordi. Echoes from quantum black holes, 2019.

[10] V. Ferrari and K. D. Kokkotas. Scattering of particles by neutron stars: Time evolutions for axial perturbations. *Phys. Rev. D*, 62:107504, 2000. doi:10.1103/PhysRevD.62.107504.

[11] P. Pani and V. Ferrari. On gravitational-wave echoes from neutron-star binary coalescences. *Class. Quant. Grav.*, 35(15):15LT01, 2018. doi:10.1088/1361-6382/aacb8f.

[12] L. Buoninfante and A. Mazumdar. Nonlocal star as a blackhole mimicker, 2019.

[13] L. Buoninfante, A. Mazumdar, and J. Peng. Nonlocality amplifies echoes, 2019.

[14] A. Delhom, C. F. B. Macedo, G. J. Olmo, and L. C. B. Crispino. Absorption by black hole remnants in metric-affine gravity, 2019.

[15] V. Cardoso and P. Pani. Tests for the existence of black holes through gravitational wave echoes. *Nat. Astron.*, 1(9):586–591, 2017. doi:10.1038/s41550-017-0225-y.

[16] V. Cardoso and P. Pani. The observational evidence for horizons: from echoes to precision gravitational-wave physics, 2017.

[17] V. Cardoso and P. Pani. Testing the nature of dark compact objects: a status report, 2019.

[18] J. Abedi, H. Dykaar, and N. Afshordi. Echoes from the abyss: Tentative evidence for planck-scale structure at black hole horizons. *Phys. Rev. D*, 96 (8):082004, 2017. doi:10.1103/PhysRevD.96.082004.

[19] R. S. Conklin, B. Holdom, and J. Ren. Gravitational wave echoes through new windows. *Phys. Rev. D*, 98(4):044021, 2018. doi:10.1103/PhysRevD.98.044021.

[20] J. Abedi and N. Afshordi. Echoes from the abyss: A highly spinning black hole remnant for the binary neutron star merger gw170817, 2018.

[21] G. Ashton, O. Birnholtz, M. Cabero, C. Capano, T. Dent, B. Krishnan, G. D. Meadors, A. B. Nielsen, A. Nitz, and J. Westerweck. Comments on: "echoes from the abyss: Evidence for planck-scale structure at black hole horizons", 2016.

[22] J. Abedi, H. Dykaar, and N. Afshordi. Echoes from the abyss: The holiday edition!, 2017.

[23] J. Westerweck, A. Nielsen, O. Fischer-Birnholtz, M. Cabero, C. Capano, T. Dent, B. Krishnan, G. Meadors, and A. H. Nitz. Low significance of evidence for black hole echoes in gravitational wave data. *Phys. Rev. D*, 97 (12):124037, 2018. doi:10.1103/PhysRevD.97.124037.

[24] J. Abedi, H. Dykaar, and N. Afshordi. Comment on: "low significance of evidence for black hole echoes in gravitational wave data", 2018.

[25] N. Uchikata, H. Nakano, T. Narikawa, N. Sago, H. Tagoshi, and T. Tanaka. Searching for black hole echoes from the ligo-virgo catalog gwtc-1, 2019.

[26] K. W. Tsang, A. Ghosh, A. Samajdar, K. Chatziioannou, S. Mastrogiovanni, M. Agathos, and C. V. D. Broeck. A morphology-independent search for gravitational wave echoes in data from the first and second observing runs of advanced ligo and advanced virgo, 2019.

[27] R. S. Conklin and B. Holdom. Gravitational wave "echo" spectra, 2019.

[28] K. W. Tsang, M. Rollier, A. Ghosh, A. Samajdar, M. Agathos, K. Chatziioannou, V. Cardoso, G. Khanna, and C. Van Den Broeck. A morphology-independent data analysis method for detecting and characterizing gravitational wave echoes. *Phys. Rev. D*, 98(2):024023, 2018. doi:10.1103/PhysRevD.98.024023.

[29] K. Lin, W.-L. Qian, X. Fan, and H. Zhang. Tail wavelets in the merger of binary compact objects, 2019.

[30] H. Nakano, N. Sago, H. Tagoshi, and T. Tanaka. Black hole ringdown echoes and howls. *PTEP*, 2017(7):071E01, 2017. doi:10.1093/ptep/ptx093.

[31] Z. Mark, A. Zimmerman, S. M. Du, and Y. Chen. A recipe for echoes from exotic compact objects, 2017.

[32] A. Maselli, S. H. Volkel, and K. D. Kokkotas. Parameter estimation of gravitational wave echoes from exotic compact objects. *Phys. Rev. D*, 96(6): 064045, 2017. doi:10.1103/PhysRevD.96.064045.

[33] P. Bueno, P. A. Cano, F. Goelen, T. Hertog, and B. Vercnocke. Echoes of kerr-like wormholes. *Phys. Rev. D*, 97(2):024040, 2018. doi:10.1103/PhysRevD.97.024040.

[34] Y.-T. Wang, Z.-P. Li, J. Zhang, S.-Y. Zhou, and Y.-S. Piao. Are gravitational wave ringdown echoes always equal-interval? *Eur. Phys. J. C*, 78(6):482, 2018. doi:10.1140/epjc/s10052-018-5974-y.

[35] M. R. Correia and V. Cardoso. Characterization of echoes: A dyson-series representation of individual pulses. *Phys. Rev. D*, 97(8):084030, 2018. doi:10.1103/PhysRevD.97.084030.

[36] Q. Wang and N. Afshordi. Black hole echology: The observer's manual. *Phys. Rev. D*, 97(12):124044, 2018. doi:10.1103/PhysRevD.97.124044.

[37] J. L. Friedman. Ergosphere instability. *Communications in Mathematical Physics*, 63:243–255, 1978. doi:10.1007/BF01196933.

[38] G. Moschidis. A proof of friedman's ergosphere instability for scalar waves. *Commun. Math. Phys.*, 358(2):437–520, 2018. doi:10.1007/s00220-017-3010-y.

[39] R. Brito, V. Cardoso, and P. Pani. *Superradiance*, volume 906 of *Lecture Notes in Physics*. Springer, 2015. doi:10.1007/978-3-319-19000-6.

[40] V. Cardoso, P. Pani, M. Cadoni, and M. Cavaglia. Ergoregion instability of ultracompact astrophysical objects. *Phys. Rev. D*, 77:124044, 2008. doi:10.1103/PhysRevD.77.124044.

[41] V. Cardoso, P. Pani, M. Cadoni, and M. Cavaglia. Instability of hyper-compact kerr-like objects. *Class. Quant. Grav.*, 25(19):195010, 2008. doi:10.1088/0264-9381/25/19/195010.

[42] C. B. M. H. Chirenti and L. Rezzolla. On the ergoregion instability in rotating gravastars. *Phys. Rev. D*, 78:084011, 2008. doi:10.1103/PhysRevD.78.084011.

[43] V. Cardoso, L. C. B. Crispino, C. F. B. Macedo, H. Okawa, and P. Pani. Light rings as observational evidence for event horizons: long-lived modes, ergoregions and nonlinear instabilities of ultracompact objects. *Phys. Rev. D*, 90(4):044069, 2014. doi:10.1103/PhysRevD.90.044069.

[44] R. Vicente, V. Cardoso, and J. C. Lopes. Penrose process, superradiance, and ergoregion instabilities. *Phys. Rev. D*, 97(8):084032, 2018. doi:10.1103/PhysRevD.97.084032.

[45] E. Barausse, R. Brito, V. Cardoso, I. Dvorkin, and P. Pani. The stochastic gravitational-wave background in the absence of horizons. *Class. Quant. Grav.*, 35(20):20LT01, 2018. doi:10.1088/1361-6382/aae1de.

[46] G. Poschl and E. Teller. Bemerkungen zur quantenmechanik des anharmonischen oszillators. *Z. Phys.*, 83:143–151, 1933. doi:10.1007/BF01331132.

[47] V. Ferrari and B. Mashhoon. New approach to the quasinormal modes of a black hole. *Phys. Rev. D*, 30:295–304, 1984. doi:10.1103/PhysRevD.30.295.

[48] G. Raposo, P. Pani, and R. Emparan. Exotic compact objects with soft hair, 2018.

[49] C. Barcelo, R. Carballo-Rubio, and S. Liberati. Generalized no-hair theorems without horizons, 2019.

[50] P. Pani. I-love-q relations for gravastars and the approach to the black-hole limit. *Phys. Rev. D*, 92(12):124030, 2015. doi:10.1103/PhysRevD.92.124030.

[51] N. Uchikata and S. Yoshida. Slowly rotating thin shell gravastars. *Class. Quant. Grav.*, 33(2):025005, 2016. doi:10.1088/0264-9381/33/2/025005.

[52] N. Uchikata, S. Yoshida, and P. Pani. Tidal deformability and i-love-q relations for gravastars with polytropic thin shells. *Phys. Rev. D*, 94(6):064015, 2016. doi:10.1103/PhysRevD.94.064015.

[53] K. Yagi and N. Yunes. I-love-q anisotropically: Universal relations for compact stars with scalar pressure anisotropy. *Phys. Rev. D*, 91(12):123008, 2015. doi:10.1103/PhysRevD.91.123008.

[54] K. Yagi and N. Yunes. Relating follicly-challenged compact stars to bald black holes: A link between two no-hair properties. *Phys. Rev. D*, 91(10): 103003, 2015. doi:10.1103/PhysRevD.91.103003.

[55] C. Posada. Slowly rotating supercompact schwarzschild stars. *Mon. Not. Roy. Astron. Soc.*, 468(2):2128–2139, 2017. doi:10.1093/mnras/stx523.

[56] S. A. Teukolsky. Rotating black holes - separable wave equations for gravitational and electromagnetic perturbations. *Phys. Rev. Lett.*, 29:1114–1118, 1972. doi:10.1103/PhysRevLett.29.1114.

[57] S. A. Teukolsky. Perturbations of a rotating black hole. 1. fundamental equations for gravitational electromagnetic and neutrino field perturbations. *Astrophys. J.*, 185:635–647, 1973. doi:10.1086/152444.

[58] S. A. Teukolsky and W. H. Press. Perturbations of a rotating black hole. iii - interaction of the hole with gravitational and electromagnetic radiation. *Astrophys. J.*, 193:443–461, 1974. doi:10.1086/153180.

[59] S. Detweiler. On resonant oscillations of a rapidly rotating black hole. *Proceedings of the Royal Society of London Series A*, 352:381–395, 1977. doi:10.1098/rspa.1977.0005.

[60] S. Chandrasekhar. *The Mathematical Theory of Black Holes*. Oxford University Press, New York, 1983.

[61] A. Vilenkin. Exponential amplification of waves in the gravitational field of ultrarelativistic rotating body. *Phys. Lett. B*, 78:301–303, 1978. doi:10.1016/0370-2693(78)90027-8.

[62] I. Novikov and V. Frolov. *Black Hole Physics*. Springer, 1989.

[63] M. Casals and A. C. Ottewill. Canonical quantization of the electromagnetic field on the kerr background. *Phys. Rev. D*, 71:124016, 2005. doi:10.1103/PhysRevD.71.124016. URL `https://link.aps.org/doi/10.1103/PhysRevD.71.124016`.

[64] A. A. Starobinskij and S. M. Churilov. Amplification of electromagnetic and gravitational waves scattered by a rotating black hole. *Zhurnal Eksperimentalnoi i Teoreticheskoi Fiziki*, 65:3–11, 1973.

[65] A. Neitzke. Greybody factors at large imaginary frequencies, 2003.

[66] T. Harmark, J. Natario, and R. Schiappa. Greybody factors for d-dimensional black holes. *Adv. Theor. Math. Phys.*, 14(3):727–794, 2010. doi:10.4310/ATMP.2010.v14.n3.a1.

[67] E. Berti, V. Cardoso, and C. M. Will. On gravitational-wave spectroscopy of massive black holes with the space interferometer lisa. *Phys. Rev. D*, 73: 064030, 2006. doi:10.1103/PhysRevD.73.064030.

[68] A. Buonanno, G. B. Cook, and F. Pretorius. Inspiral, merger and ring-down of equal-mass black-hole binaries. *Phys. Rev. D*, 75:124018, 2007. doi:10.1103/PhysRevD.75.124018.

[69] N. Oshita, Q. Wang, and N. Afshordi. On reflectivity of quantum black hole horizons, 2019.

[70] LIGO Collaboration and D. Shoemaker. Advanced ligo anticipated sensitivity curves. Technical Report T0900288-v3, 2010. Available at `https://dcc.ligo.org/LIGO-T0900288/public`.

[71] Y. B. Zel'dovich. Pis'ma zh. eksp. teor. fiz. 14 (1971) 270 [jetp lett. 14, 180 (1971)]. *Pis'ma Zh. Eksp. Teor. Fiz.*, 14:270, 1971. [JETP Lett. 14, 180 (1971)].

[72] J. L. Friedman. Generic instability of rotating relativistic stars. *Commun. Math. Phys.*, 62(3):247–278, 1978. doi:10.1007/BF01202527.

[73] E. E. Flanagan and S. A. Hughes. Measuring gravitational waves from binary black hole coalescences: 1. signal-to-noise for inspiral, merger, and ringdown. *Phys. Rev. D*, 57:4535–4565, 1998. doi:10.1103/PhysRevD.57.4535.

[74] E. W. Leaver. Spectral decomposition of the perturbation response of the schwarzschild geometry. *Phys. Rev. D*, 34:384–408, 1986. doi:10.1103/PhysRevD.34.384.

[75] E. Berti, V. Cardoso, and A. O. Starinets. Quasinormal modes of black holes and black branes. *Class. Quantum Grav.*, 26(16):163001, 2009. doi:10.1088/0264-9381/26/16/163001.

[76] M. Vallisneri. Use and abuse of the fisher information matrix in the assessment of gravitational-wave parameter-estimation prospects. *Phys. Rev. D*, 77: 042001, 2008. doi:10.1103/PhysRevD.77.042001.

[77] LIGO Scientific Collaboration, B. P. Abbott, et al. Exploring the sensitivity of next generation gravitational wave detectors. *Class. Quant. Grav.*, 34(4): 044001, 2017. doi:10.1088/1361-6382/aa51f4.

[78] R. Essick, S. Vitale, and M. Evans. Frequency-dependent responses in third generation gravitational-wave detectors. *Phys. Rev. D*, 96(8):084004, 2017. doi:10.1103/PhysRevD.96.084004.

[79] S. Hild et al. Sensitivity studies for third-generation gravitational wave observatories. *Class. Quant. Grav.*, 28:094013, 2011. doi:10.1088/0264-9381/28/9/094013.

[80] H. Audley, S. Babak, J. Baker, E. Barausse, P. Bender, E. Berti, P. Binetruy, M. Born, D. Bortoluzzi, J. Camp, C. Caprini, V. Cardoso, M. Colpi, J. Conklin, N. Cornish, C. Cutler, et al. Laser interferometer space antenna, 2017. ArXiv e-prints, arXiv:1702.00786.

[81] C. P. Burgess, R. Plestid, and M. Rummel. Effective field theory of black hole echoes. *JHEP*, 09:113, 2018. doi:10.1007/JHEP09(2018)113.

[82] A. A. Starobinskiĭ. Spectrum of relict gravitational radiation and the early state of the universe. *Soviet Journal of Experimental and Theoretical Physics Letters*, 30:682, December 1979. ISSN 0021-3640. URL http://adsabs.harvard.edu/abs/1979JETPL..30..682S.

[83] Alan H. Guth. Inflationary universe: A possible solution to the horizon and flatness problems. *Physical Review D*, 23(2):347–356, January 1981. doi:10.1103/PhysRevD.23.347. URL https://link.aps.org/doi/10.1103/PhysRevD.23.347. Publisher: American Physical Society.

[84] A. D. Linde. A new inflationary universe scenario: A possible solution of the horizon, flatness, homogeneity, isotropy and primordial monopole problems. *Physics Letters B*, 108(6):389–393, February 1982. ISSN 0370-2693. doi:10.1016/0370-2693(82)91219-9. URL http://www.sciencedirect.com/science/article/pii/0370269382912199.

[85] A. D. Linde. Coleman-Weinberg theory and the new inflationary universe scenario. *Physics Letters B*, 114(6):431–435, August 1982. ISSN 0370-2693. doi:10.1016/0370-2693(82)90086-7. URL http://www.sciencedirect.com/science/article/pii/0370269382900867.

[86] Andreas Albrecht and Paul J. Steinhardt. Cosmology for Grand Unified Theories with Radiatively Induced Symmetry Breaking. *Physical Review Letters*, 48(17):1220–1223, April 1982. doi:10.1103/PhysRevLett.48.1220. URL https://link.aps.org/doi/10.1103/PhysRevLett.48.1220. Publisher: American Physical Society.

[87] Juan Maldacena. Non-gaussian features of primordial fluctuations in single field inflationary models. *Journal of High Energy Physics*, 2003(05):013–013, May 2003. ISSN 1029-8479. doi:10.1088/1126-6708/2003/05/013. URL http://stacks.iop.org/1126-6708/2003/i=05/a=013?key=crossref.b9cd189c7a03380cbcfbc82162f2f8f2.

[88] Neal Dalal, Olivier Doré, Dragan Huterer, and Alexander Shirokov. Imprints of primordial non-Gaussianities on large-scale structure: Scale-dependent bias and abundance of virialized objects. *Physical Review D*, 77(12):123514, June 2008. ISSN 1550-7998, 1550-2368. doi:10.1103/PhysRevD.77.123514. URL https://link.aps.org/doi/10.1103/PhysRevD.77.123514.

[89] Takahiro Tanaka and Yuko Urakawa. Dominance of gauge artifact in the consistency relation for the primordial bispectrum. *Journal of Cosmology and Astroparticle Physics*, 2011(05):014–014, May 2011. ISSN 1475-7516. doi:10.1088/1475-7516/2011/05/014. URL https://doi.org/10.1088%2F1475-7516%2F2011%2F05%2F014. Publisher: IOP Publishing.

[90] Enrico Pajer, Fabian Schmidt, and Matias Zaldarriaga. The Observed squeezed limit of cosmological three-point functions. *Physical Review D*, 88(8):083502, October 2013. ISSN 1550-7998, 1550-2368. doi:10.1103/PhysRevD.88.083502. URL https://link.aps.org/doi/10.1103/PhysRevD.88.083502.

[91] Giovanni Cabass, Enrico Pajer, and Fabian Schmidt. How Gaussian can our Universe be? *Journal of Cosmology and Astroparticle Physics*, 2017(01):003–003, January 2017. ISSN 1475-7516. doi:10.1088/1475-7516/2017/01/003. URL http://arxiv.org/abs/1612.00033. arXiv: 1612.00033.

[92] Rafael Bravo, Sander Mooij, Gonzalo A. Palma, and Bastián Pradenas. Vanishing of local non-Gaussianity in canonical single field inflation. *Journal of Cosmology and Astroparticle Physics*, 2018(05):025–025, May 2018. ISSN 1475-7516. doi:10.1088/1475-7516/2018/05/025. URL http://stacks.iop.org/1475-7516/2018/i=05/a=025?key=crossref.68ebe96893df575b23183271f7f89094.

[93] Liang Dai, Enrico Pajer, and Fabian Schmidt. Conformal Fermi Coordinates. *Journal of Cosmology and Astroparticle Physics*, 2015(11):043–043, November 2015. ISSN 1475-7516. doi:10.1088/1475-7516/2015/11/043. URL https://doi.org/10.1088%2F1475-7516%2F2015%2F11%2F043. Publisher: IOP Publishing.

[94] T. J. Allen, B. Grinstein, and Mark B. Wise. Non-gaussian density perturbations in inflationary cosmologies. *Physics Letters B*, 197(1):66–70, October 1987. ISSN 0370-2693. doi:10.1016/0370-2693(87)90343-1. URL http://www.sciencedirect.com/science/article/pii/0370269387903431.

[95] N. Bartolo, S. Matarrese, and A. Riotto. Non-Gaussianity from inflation. *Physical Review D*, 65(10):103505, April 2002. ISSN 0556-2821, 1089-4918. doi:10.1103/PhysRevD.65.103505. URL https://link.aps.org/doi/10.1103/PhysRevD.65.103505.

[96] Mohsen Alishahiha, Eva Silverstein, and David Tong. DBI in the sky: Non-Gaussianity from inflation with a speed limit. *Physical Review D*, 70(12):123505, December 2004. doi:10.1103/PhysRevD.70.123505. URL https://link.aps.org/doi/10.1103/PhysRevD.70.123505. Publisher: American Physical Society.

[97] Xingang Chen and Yi Wang. Large non-Gaussianities with intermediate shapes from quasi-single-field inflation. *Physical Review D*, 81(6):063511, March 2010. ISSN 1550-7998, 1550-2368. doi:10.1103/PhysRevD.81.063511. URL https://link.aps.org/doi/10.1103/PhysRevD.81.063511.

[98] Xingang Chen and Yi Wang. Quasi-single field inflation and non-Gaussianities. *Journal of Cosmology and Astroparticle Physics*, 2010 (04):027–027, April 2010. ISSN 1475-7516. doi:10.1088/1475-7516/2010/04/027. URL https://doi.org/10.1088%2F1475-7516%2F2010%2F04%2F027. Publisher: IOP Publishing.

[99] Daniel Baumann and Daniel Green. Signature of supersymmetry from the early universe. *Physical Review D*, 85(10):103520, May 2012. doi:10.1103/PhysRevD.85.103520. URL https://link.aps.org/doi/10.1103/PhysRevD.85.103520. Publisher: American Physical Society.

[100] Nima Arkani-Hamed and Juan Maldacena. Cosmological Collider Physics. *arXiv:1503.08043 [astro-ph, physics:hep-ph, physics:hep-th]*, March 2015. URL http://arxiv.org/abs/1503.08043. arXiv: 1503.08043.

[101] Soubhik Kumar and Raman Sundrum. Heavy-lifting of gauge theories by cosmic inflation. *Journal of High Energy Physics*, 2018(5):11, May 2018. ISSN 1029-8479. doi:10.1007/JHEP05(2018)011. URL http://link.springer.com/10.1007/JHEP05(2018)011.

[102] Anne-Sylvie Deutsch. Influence of super-horizon modes on correlation functions during inflation. *Journal of Cosmology and Astroparticle Physics*, 2018(05):022–022, May 2018. ISSN 1475-7516. doi:10.1088/1475-7516/2018/05/022. URL https://doi.org/10.1088%2F1475-7516%2F2018%2F05%2F022. Publisher: IOP Publishing.

[103] Xingang Chen, Yi Wang, and Zhong-Zhi Xianyu. Neutrino signatures in primordial non-gaussianities. *Journal of High Energy Physics*, 2018(9):22, September 2018. ISSN 1029-8479. doi:10.1007/JHEP09(2018)022. URL http://link.springer.com/10.1007/JHEP09(2018)022.

[104] Haipeng An, Mark B. Wise, and Zipei Zhang. de Sitter quantum loops as the origin of primordial non-Gaussianities. *Physical Review D*, 99(5):056007, March 2019. ISSN 2470-0010, 2470-0029. doi:10.1103/PhysRevD.99.056007. URL https://link.aps.org/doi/10.1103/PhysRevD.99.056007.

[105] Michael McAneny and Alexander K. Ridgway. New shapes of primordial non-Gaussianity from quasi-single field inflation with multiple isocurvatons. *Physical Review D*, 100(4):043534, August 2019. ISSN 2470-0010, 2470-0029. doi:10.1103/PhysRevD.100.043534. URL https://link.aps.org/doi/10.1103/PhysRevD.100.043534.

[106] Soubhik Kumar and Raman Sundrum. Cosmological Collider Physics and the Curvaton. *arXiv:1908.11378 [astro-ph, physics:hep-ph]*, August 2019. URL http://arxiv.org/abs/1908.11378. arXiv: 1908.11378 version: 1.

[107] Shiyun Lu, Yi Wang, and Zhong-Zhi Xianyu. A cosmological Higgs collider. *Journal of High Energy Physics*, 2020(2):11, February 2020. ISSN 1029-8479. doi:10.1007/JHEP02(2020)011. URL http://link.springer.com/10.1007/JHEP02(2020)011.

[108] Anson Hook, Junwu Huang, and Davide Racco. Minimal signatures of the standard model in non-Gaussianities. *Physical Review D*, 101(2):023519, January 2020. ISSN 2470-0010, 2470-0029. doi:10.1103/PhysRevD.101.023519. URL https://link.aps.org/doi/10.1103/PhysRevD.101.023519.

[109] Valentin Assassi, Daniel Baumann, Daniel Green, and Liam McAllister. Planck-suppressed operators. *Journal of Cosmology and Astroparticle Physics*, 2014(01):033–033, January 2014. ISSN 1475-7516. doi:10.1088/1475-7516/2014/01/033. URL https://doi.org/10.1088%2F1475-7516%2F2014%2F01%2F033. Publisher: IOP Publishing.

[110] Haipeng An, Michael McAneny, Alexander K. Ridgway, and Mark B. Wise. Non-Gaussian enhancements of galactic halo correlations in quasi-single field inflation. *Physical Review D*, 97(12):123528, June 2018. ISSN 2470-0010, 2470-0029. doi:10.1103/PhysRevD.97.123528. URL https://link.aps.org/doi/10.1103/PhysRevD.97.123528.

[111] Clifford Cheung, A. Liam Fitzpatrick, Jared Kaplan, Leonardo Senatore, and Paolo Creminelli. The effective field theory of inflation. *Journal of High Energy Physics*, 2008(03):014–014, March 2008. ISSN 1126-6708. doi:10.1088/1126-6708/2008/03/014. URL https://doi.org/10.1088%2F1126-6708%2F2008%2F03%2F014. Publisher: Springer Science and Business Media LLC.

[112] Steven Weinberg. Quantum contributions to cosmological correlations. *Physical Review D*, 72(4):043514, August 2005. doi:10.1103/PhysRevD.72.043514. URL https://link.aps.org/doi/10.1103/PhysRevD.72.043514. Publisher: American Physical Society.

[113] Daniel Baumann. TASI Lectures on Inflation. *arXiv:0907.5424 [astro-ph, physics:gr-qc, physics:hep-ph, physics:hep-th]*, November 2012. URL http://arxiv.org/abs/0907.5424. arXiv: 0907.5424.

[114] V. Desjacques, D. Jeong, and F. Schmidt. Large-scale galaxy bias. *Phys. Rept.*, 733:1–193, 2018.

[115] P. McDonald. Clustering of dark matter tracers: Renormalizing the bias parameters. *Phys. Rev. D*, 74:103512, 2006.

[116] P. McDonald and A. Roy. Clustering of dark matter tracers: generalizing bias for the coming era of precision lss. *Journal of Cosmology and Astroparticle Physics*, 2009(08):020–020, 2009.

[117] V. Assassi, D. Baumann, D. Green, and M. Zaldarriaga. Renormalized halo bias. *Journal of Cosmology and Astroparticle Physics*, 2014(08):056–056, 2014.

[118] P. McDonald. Primordial non-gaussianity: Large-scale structure signature in the perturbative bias model. *Physical Review D*, 78(12), 2008.

[119] V. Assassi, D. Baumann, and F. Schmidt. Galaxy bias and primordial non-gaussianity. *Journal of Cosmology and Astroparticle Physics*, 2015(12): 043–043, 2015.

[120] N. Aghanim et al. Planck 2018 results. vi. cosmological parameters. *Astron. Astrophys.*, 641:A6, 2020. [Erratum: Astron.Astrophys. 652, C4 (2021)].

[121] P. J. E. Peebles. *The large-scale structure of the universe*. Princeton University Press, 1980.

[122] J. N. Fry. The galaxy correlation hierarchy in perturbation theory. *Astrophys. J.*, 279:499–510, 1984.

[123] M. H. Goroff, B. Grinstein, S. J. Rey, and M. B. Wise. Coupling of modes of cosmological mass density fluctuations. *Astrophys. J.*, 311:6–14, 1986.

[124] D. Jeong. *Cosmology with high* ($z > 1$) *redshift galaxy surveys*. PhD thesis, University of Texas Austin, 2010. URL https://repositories.lib.utexas.edu/handle/2152/ETD-UT-2010-08-1781.

[125] J. J. M. Carrasco, M. P. Hertzberg, and L. Senatore. The effective field theory of cosmological large scale structures. *JHEP*, 09:082, 2012.

[126] D. Baumann, A. Nicolis, L. Senatore, and M. Zaldarriaga. Cosmological non-linearities as an effective fluid. *Journal of Cosmology and Astroparticle Physics*, 2012(07):051–051, 2012.

[127] T. Baldauf, M. Mirbabayi, M. Simonović, and M. Zaldarriaga. Lss constraints with controlled theoretical uncertainties. *arXiv preprint arXiv:1602.00674*, 2016.

[128] M. Mirbabayi, F. Schmidt, and M. Zaldarriaga. Biased tracers and time evolution. *JCAP*, 07:030, 2015.

[129] A. Kehagias and A. Riotto. Conformal symmetries of frw accelerating cosmologies. *Nucl. Phys. B*, 884:547–565, 2014.

[130] A. Aghamousa et al. The desi experiment part i: Science, targeting, and survey design, 2016.

[131] L. Amendola et al. Cosmology and fundamental physics with the euclid satellite. *Living Rev. Rel.*, 21:2, 2018. doi:10.1007/s41114-017-0010-3.

[132] O. Doré, J. Bock, M. Ashby, P. Capak, A. Cooray, R. de Putter, T. Eifler, N. Flagey, Y. Gong, S. Habib, K. Heitmann, C. Hirata, W.-S. Jeong, R. Katti, P. Korngut, E. Krause, D.-H. Lee, D. Masters, P. Mauskopf, G. Melnick, B. Mennesson, H. Nguyen, K. Öberg, A. Pullen, A. Raccanelli, R. Smith, Y.-S. Song, V. Tolls, S. Unwin, T. Venumadhav, M. Viero, M. Werner, and M. Zemcov. Cosmology with the spherex all-sky spectral survey, 2015.

[133] T. Eifler et al. Survey optimization for cosmology with the rubin observatory legacy survey of space and time. *Mon. Not. Roy. Astron. Soc.*, 507:1514, 2021. doi:10.1093/mnras/stab533.

[134] N. Dalal, O. Doré, D. Huterer, and A. Shirokov. Imprints of primordial non-gaussianities on large-scale structure: Scale-dependent bias and abundance of virialized objects. *Phys. Rev. D*, 77:123514, 2008. doi:10.1103/PhysRevD.77.123514.

[135] P. McDonald. Primordial non-gaussianity: Large-scale structure signature in the perturbative bias model. *JCAP*, 2009:026–026, 2009. doi:10.1088/1475-7516/2009/11/026.

[136] J. Yoo, N. Hamaus, U. Seljak, and M. Zaldarriaga. Testing general relativity on horizon scales and the geometry of the universe using the galaxy bispectrum. *Phys. Rev. D*, 86, 2012. doi:10.1103/physrevd.86.063514.

[137] J. Yoo. General relativistic description of the observed galaxy power spectrum: Do we understand what we measure? *Phys. Rev. D*, 82, 2010. doi:10.1103/physrevd.82.083508.

[138] C. Bonvin and R. Durrer. What galaxy surveys really measure. *Phys. Rev. D*, 84, 2011. doi:10.1103/physrevd.84.063505.

[139] A. Challinor and A. Lewis. The linear power spectrum of observed source number counts. *Phys. Rev. D*, 84, 2011. doi:10.1103/physrevd.84.043516.

[140] K. Yamamoto, M. Nakamichi, A. Kamino, B. A. Bassett, and H. Nishioka. A measurement of the galaxy bispectrum in the two-degree field galaxy redshift survey. *Publ. Astron. Soc. Japan*, 58:93–102, 2006. doi:10.1093/pasj/58.1.93.

[141] D. Bianchi, H. Gil-Marín, R. Ruggeri, and W. J. Percival. Measuring redshift-space distortions with the bispectrum. *Mon. Not. R. Astron. Soc. Lett.*, 453: L11–L15, 2015. doi:10.1093/mnrasl/slv090.

[142] R. Scoccimarro. Redshift-space distortions, pairwise velocities, and nonlinearities. *Phys. Rev. D*, 92, 2015. doi:10.1103/physrevd.92.083532.

[143] P. Reimberg, F. Bernardeau, and C. Pitrou. General relativistic corrections to the observed bispectrum. *JCAP*, 2016:048–048, 2016. doi:10.1088/1475-7516/2016/01/048.

[144] F. Beutler, E. Castorina, and P. Zhang. The bispectrum monopole in redshift space: theory and application to mock galaxies. *JCAP*, 2019:040, 2019. doi:10.1088/1475-7516/2019/03/040.

[145] J. N. Benabou, I. Sands, C. Heinrich, H. S. Grasshorn Gebhardt, and O. Doré. Galaxy bispectrum in the spherical fourier-bessel basis, in prep.

[146] K. Pardede, E. D. Dio, and E. Castorina. Wide-angle effects in the galaxy bispectrum, 2023.

[147] E. Di Dio, R. Durrer, G. Marozzi, and F. Montanari. The bispectrum of relativistic galaxy number counts. *JCAP*, 2016:016–016, 2016. doi:10.1088/1475-7516/2016/01/016.

[148] O. Lahav. Spherical harmonic reconstruction of cosmic density and velocity fields, 1993.

[149] J. Binney and T. Quinn. Gaussian random fields on a sphere: Applications to cosmology. *Mon. Not. R. Astron. Soc.*, 249:678, 1991.

[150] A. F. Heavens and A. N. Taylor. A spherical harmonic analysis of redshift surveys. *Mon. Not. R. Astron. Soc.*, 275:483–497, 1995. doi:10.1093/mnras/275.2.483.

[151] H. Tadros, W. E. Ballinger, A. N. Taylor, A. F. Heavens, G. Efstathiou, W. Saunders, C. S. Frenk, O. Keeble, R. McMahon, S. J. Maddox, S. Oliver, M. Rowan-Robinson, W. J. Sutherland, and S. D. M. White. Redshift-space distortions in the iras pscz galaxy survey. *Mon. Not. R. Astron. Soc.*, 305: 527–546, 1999. doi:10.1046/j.1365-8711.1999.02409.x.

[152] W. J. Percival, D. Burkey, A. Heavens, A. Taylor, S. Cole, J. A. Peacock, C. M. Baugh, J. Bland-Hawthorn, T. Bridges, R. Cannon, M. Colless, C. Collins, W. Couch, G. Dalton, R. De Propris, S. P. Driver, G. Efstathiou, R. S. Ellis, C. S. Frenk, K. Glazebrook, C. Jackson, O. Lahav, I. Lewis, S. Lumsden, S. Maddox, P. Norberg, B. A. Peterson, W. Sutherland, and K. Taylor. The 2df galaxy redshift survey: Spherical harmonics analysis of fluctuations in the final catalogue. *Mon. Not. R. Astron. Soc.*, 353:1201–1218, 2004. doi:10.1111/j.1365-2966.2004.08146.x.

[153] L. Samushia. Proper fourier decomposition formalism for cosmological fields in spherical shells, 2019.

[154] H. S. G. Gebhardt and O. Doré. Superfab: a fabulous code for spherical fourier-bessel decomposition, 2021.

[155] M. Wang, S. Avila, D. Bianchi, R. Crittenden, and W. Percival. The spherical fourier-bessel bispectrum estimator: Modelling and first application to sdss-iii boss galaxies. *JCAP*, 2020:022–022, 2020. doi:10.1088/1475-7516/2020/10/022.

[156] H. S. Grasshorn Gebhardt and O. Doré. A fast algorithm for the spherical fourier-bessel decomposition of large galaxy surveys. *JCAP*, 01:038, 2022. doi:10.1088/1475-7516/2022/01/038.

[157] H. Grasshorn Gebhardt and O. Doré. A new estimator for the galaxy bispectrum in the spherical fourier-bessel basis, 2023.

[158] Y. Zhang, A. R. Pullen, and A. S. Maniyar. Spherical fourier-bessel bispectrum estimation: Modelling and application to galaxy surveys. *Phys. Rev. D*, 104, 2021. doi:10.1103/physrevd.104.103523.

[159] D. Gualdi and L. Verde. Spherical fourier-bessel decomposition in the era of large galaxy surveys: An implementation for intensity mapping. *JCAP*, 2020:041–041, 2020. doi:10.1088/1475-7516/2020/06/041.

[160] C. Heinrich, O. Doré, and E. Krause. Systematics in spherical fourier-bessel bispectrum estimators, 2023.

[161] W. R. Coulton, J. Liu, M. S. Madhavacheril, V. Böhm, and D. N. Spergel. Spherical fourier-bessel bispectrum of the cmb: Analysis with planck data. *JCAP*, 2019:043–043, 2019. doi:10.1088/1475-7516/2019/05/043.

[162] R. Ruggeri, E. Castorina, C. Carbone, and E. Sefusatti. The galaxy bispectrum in spherical fourier-bessel space: A new window into primordial non-gaussianity. *JCAP*, 2018:003–003, 2018. doi:10.1088/1475-7516/2018/03/003.

[163] R. Maartens, S. Jolicoeur, O. Umeh, E. M. D. Weerd, C. Clarkson, and S. Camera. Relativistic effects and wide-angle corrections in the galaxy bispectrum. *JCAP*, 2020:065–065, 2020. doi:10.1088/1475-7516/2020/03/065.

[164] D. Jeong and F. Schmidt. Redshift-space distortions and relativistic corrections to the galaxy bispectrum. *Phys. Rev. D*, 102:023530, 2020. doi:10.1103/PhysRevD.102.023530.

[165] C. Clarkson, E. M. de Weerd, S. Jolicoeur, R. Maartens, and O. Umeh. Wide-angle and relativistic corrections to the bispectrum of large-scale structure. *Mon. Not. Roy. Astron. Soc.*, 486:L101, 2019. doi:10.1093/mnrasl/slz066.

[166] D. Bertacca, A. Raccanelli, N. Bartolo, M. Liguori, S. Matarrese, and L. Verde. Relativistic corrections to the observed galaxy bispectrum. *Phys. Rev. D*, 97, 2018. doi:10.1103/physrevd.97.023531.

[167] A. Lewis, A. Challinor, and A. Lasenby. Efficient computation of cmb anisotropies in closed frw models. *Astrophys. J.*, 538:473, 2001. http://camb.info.

[168] J. Bezanson, A. Edelman, S. Karpinski, and V. B. Shah. Julia: A fresh approach to numerical computing. *SIAM Review*, 59:65, 2017. doi:10.1137/141000671.

[169] M. Tellarini, A. J. Ross, G. Tasinato, and D. Wands. Non-local bias in galaxy bispectrum on large scales. *JCAP*, 2016:014–014, 2016. doi:10.1088/1475-7516/2016/06/014.

[170] F. Bernardeau, S. Colombi, E. Gaztañaga, and R. Scoccimarro. Large-scale structure of the universe and cosmological perturbation theory. *Phys. Rep.*, 367:1–248, 2002. doi:10.1016/s0370-1573(02)00135-7.

[171] D. Wands and A. Slosar. Scale-dependent bias from primordial non-gaussianity in general relativity. *Phys. Rev. D*, 79:123507, 2009. doi:10.1103/PhysRevD.79.123507.

[172] J. Yoo, A. L. Fitzpatrick, and M. Zaldarriaga. A new perspective on galaxy clustering as a cosmological probe: General relativistic effects. *Phys. Rev. D*, 80:083514, 2009. doi:10.1103/PhysRevD.80.083514.

[173] J. Yoo. General relativistic description of the observed galaxy power spectrum: Do we understand what we measure? *Phys. Rev. D*, 82:083508, 2010. doi:10.1103/PhysRevD.82.083508.

[174] P. Catelan, C. Porciani, and M. Kamionkowski. Intrinsic and extrinsic galaxy alignments in weak gravitational lensing surveys. *Mon. Not. R. Astron. Soc.*, 318:39, 2000. doi:10.1046/j.1365-8711.2000.04023.x.

[175] T. Baldauf, U. Seljak, V. Desjacques, and P. McDonald. Evidence for quadratic tidal tensor bias from the halo bispectrum. *Phys. Rev. D*, 86: 083540, 2012. doi:10.1103/PhysRevD.86.083540.

[176] G. Szego. Orthogonal polynomials and legendre roots. *Trans. Am. Math. Soc.*, 39:1, 1936. URL http://www.jstor.org/stable/1989641.

[177] D. N. Limber. The analysis of counts of the extragalactic nebulae in terms of a fluctuating density field. *Astrophys. J.*, 119:655, 1954. doi:10.1086/145870.

[178] N. Kaiser. Weak lensing and cosmology. *Astrophys. J.*, 498:26, 1998. doi:10.1086/305515.

[179] M. LoVerde and N. Afshordi. Extended limber approximation. *Phys. Rev. D*, 78:123506, 2008. doi:10.1103/PhysRevD.78.123506.

[180] H. S. Grasshorn Gebhardt and D. Jeong. A new approach to the redshift-space bispectrum: application to the baryon oscillation spectroscopic survey dr12. *Phys. Rev. D*, 97, 2018. doi:10.1103/physrevd.97.023504.

[181] O. H. Philcox. The information content of the galaxy bispectrum. *Phys. Rev. D*, 104, 2021. doi:10.1103/physrevd.104.123529.

[182] M. Biagetti, L. Castiblanco, J. Noreña, and E. Sefusatti. Measuring primordial non-gaussianity with the galaxy bispectrum: Forecasts for the spherex survey. *JCAP*, 2022:009, 2022. doi:10.1088/1475-7516/2022/09/009.

[183] M. Noorikuhani and R. Scoccimarro. Covariances of higher-order statistics of galaxy clustering: the squeezed bispectrum. *Phys. Rev. D*, 107:083528, 2023. doi:10.1103/PhysRevD.107.083528.

[184] Z. Slepian. On decoupling the integrals of cosmological perturbation theory, 2018.

[185] R. Mehrem, J. T. Londergan, and M. H. Macfarlane. The calculation of gaunt coefficients and clebsch–gordan coefficients for quantum mechanical problems involving spherical harmonics. *J. Phys. A: Math. Gen.*, 24:1435, 1991. doi:10.1088/0305-4470/24/7/018.

[186] V. I. Fabrikant. A new method for calculating integrals of products of three spherical bessel functions. *Q. Appl. Math.*, 71:573, 2013. URL `http://www.jstor.org/stable/43645929`.

[187] H. Dong, J. S. Kim, and G. S. Chirikjian. Computation of clebsch-gordan coefficients and gaunt coefficients by hilbert space methods. *J. Comput. Biol.*, 22:787–805, 2015. doi:10.1089/cmb.2015.0115.

[188] J. Chellino and Z. Slepian. A recursive algorithm for the computation of spherical bessel and associated legendre functions. *Proc. R. Soc. A*, 479, 2023. doi:10.1098/rspa.2023.0138.

[189] A. Jackson and L. Maximon. On the computation of legendre polynomials and their roots. *SIAM J. Math. Anal.*, 3, 1972. doi:10.1137/0503043.